STUDY OF BACTERIAL MOTILITY USING OPTICAL TWEEZERS

by

Suddhashil Chattopadhyay

B.Sc.(HONS), Physics, Indian Institute of Technology, 2000

M.Sc., Physics, Indian Institute of Technology, 2002

M.S., Physics, University of Pittsburgh, Pittsburgh, 2004

Submitted to the Graduate Faculty of

the Department of Physics and Astronomy in partial fulfillment

of the requirements for the degree of

Doctor of Philosophy

University of Pittsburgh

2008

UNIVERSITY OF PITTSBURGH

DEPARTMENT OF PHYSICS AND ASTRONOMY

This dissertation was presented

by

Suddhashil Chattopadhyay

It was defended on

December 1st 2008

and approved by

Xiao-Lun Wu, Department of Physics and Astronomy

Daniel Boyanovsky, Department of Physics and Astronomy

Walter Goldburg, Department of Physics and Astronomy

David Jasnow, Department of Physics and Astronomy

Sanford Leuba, Department of Cell Biology and Physiology

Dissertation Director: Xiao-Lun Wu, Department of Physics and Astronomy

ABSTRACT

STUDY OF BACTERIAL MOTILITY USING OPTICAL TWEEZERS

Suddhashil Chattopadhyay, PhD

University of Pittsburgh, 2008

Bacteria are arguably the simplest of known microorganisms, forming a fundamental part of the world we live in. Many functions they perform are found in scaled-up versions in higher organisms. Among many advanced functions, bacteria possess the ability to move in search for nutrients and favorable growth conditions. Measurement of the dynamical variables associated with bacterial swimming has proven to be difficult due to the lack of an accurate and convenient tool. In the past optical traps have been used for the manipulation of microscopic objects and measurement of minute forces. Herein, I have devised techniques for use of optical traps for direct measurement of the dynamics of bacterial swimming and chemotaxis, shedding light on the propulsion apparatus and sensory systems. A detailed analysis is performed to explore the effects of non-local hydrodynamic interactions on the swimming of single cells. Due to the lack of reliable measurement techniques, experimentalists often use theoretical models to estimate bacterial dynamics, the validity of which are tested. I emphasize the shortcomings of the very popular Resistive Force Theory (RFT) and indicate how the more rigorous Slender Body Theory (SBT) is able to overcome the limitations. In addition the chemotaxis of the marine bacterial strain *Vibrio alginolyticus* is studied with the revelation of a previously unknown chemotactic mechanism. Direct observations showed that these cells are able to bend their flagella to impart direction changes, which is paramount for an effective search strategy. This interesting find opens several intriguing questions pertaining to chemotaxis.

TABLE OF CONTENTS

LIST OF TABLES

LIST OF FIGURES

This thesis is dedicated to my wife, my parents and my sister, for all their love, support and encouragement.

PREFACE

I would take this opportunity to express graditude toward my advisor, Dr. Xiao-Lun Wu, without whose dedicated guidance this work would have been impossible. I also thank the members of my thesis commitee, including ex-members, Dr. Albert Heberle and Dr. Susan Gilbert, for help and suggestion, which has improved my research greatly. I am deeply indebted to these past and present members of the Wu lab, for their help and support: Dr. Matthew Shtrahman, Dr. Jie Zhang, Dr. Yonggun Jun, Dr. Emily Chapman-McQuiston, Dr. Mahesh Bandi, Dr. Radu Moldovan, Andy McQuiston, Pedram Roushan, Ildoo Kim, Tuba Altindal and Li Xie.

1.0 INTRODUCTION

Physicists have used intuitive tools to make contributions to various subjects, occasionally changing the field completely. In this thesis I demonstrate the usage of optical tweezers as an instrument for the study of bacterial motility and chemotaxis. "Motility" refers to the process by which an organism moves by itself, and "Chemotaxis" is the process by which micro-organisms look for nutrients. This work would touch upon aspects relating to the experimental tools, methodologies and interpretation of the obtained data. In the following Sections I will briefly introduce the biological and physical aspects of the systems under study.

1.1 WHAT ARE BACTERIA?

Bacteria are unicellular micro-organisms that are ubiquitous and are known to survive in even the most harsh environments, thus forming the biggest chunk of biomass on this planet. They are the simplest and most primitive of all known organisms. They perform important functions in the world we live in, be it nitrogen fixation in soil or decomposition of biological waste. The effects of bacterial populations, although not apparent, are an integral part of all we see around us.

A small fraction of bacterial species have been identified and an even smaller fraction can be cultured in the laboratory. The study of bacteria, or bacteriology forms a fundamental part of biological science. Despite being very simple in structure bacteria are able to perform advanced functions, such as chemotaxis, which is the process by which organisms are able to use sensors on them to selectively move into regions high in nutrients or to move away from toxins. A typical bacterial cell is depicted in Fig. 1.1. They have cell bodies, often spindle shaped, containing genetic material enclosed by a cell membrane. The features of most interest to me are motility and

chemotaxis which have been studied in detail in the following chapters.

1.1.1 Bacterial Motility

Bacterial motility is paramount for performing biological functions. As seen in Fig. 1.1, most bacteria possess thin filaments called flagella, which are rigid, helical in shape and are driven by a molecular motor at its base [41]. Rotation of these filaments produces thrust which pushes cells forward. Bacterial strains may differ in flagella size, function, and number. Some typical examples are shown in Fig. 1.1. The bacterial motor can change direction of rotation to add additional features to its motility. For single polar flagellated bacteria, such as *Vibrio alginolyticus*, the reversing of the motor merely takes it backward. In the case of multiple flagellated bacteria, such as *Escherichia coli*, the helicity of the flagella makes them form a bundle when the motor rotates counter clockwise (viewed from the cell exterior). This generates thrust in a particular direction making the bacteria move forward. A change of rotational direction makes the bundle fall apart generating thrust in random directions, which in turn makes the bacteria tumble. The act of tumbling randomly chooses a new direction for the cell.

Let us now look at the dynamical variables that are required to describe bacterial motility. These are summarized in Fig. 1.2. The flagellum rotates with a rate of ω and the cell body counter rotates with Ω to conserve angular momentum. As a result of its rotation, the helix produces thrust which moves the cell with a speed V. Also shown are the cell-body dimensions, a and b being the semi -minor and -major axes of the ellipsoid respectively. In order to model the geometry of the bacterium conveniently the ellipsoidal head is often approximated to be a sphere of effective radius a_E, such that they have the same linear drag. Also shown in Fig. 1.2 are the geometrical parameters of the helix, which are the wavelength λ, the length ℓ , the radius R and the flagellar filament radius r. Other variables such as the helix angle $\phi = tan^{-1}(2\pi R/\lambda)$ and $\Lambda = \lambda/cos(\phi)$ can be defined in terms of these variables.

The cell body and the flagellum have six degrees of freedom each (three rotational and three translational). However, as the flagellum and the cell body are connected and are constrained to translate along a line, the degrees of freedom available to the bacterium gets reduced to three. These are the swimming speed (V), and the rotation rates for the cell body (Ω) and the flagellum(ω).

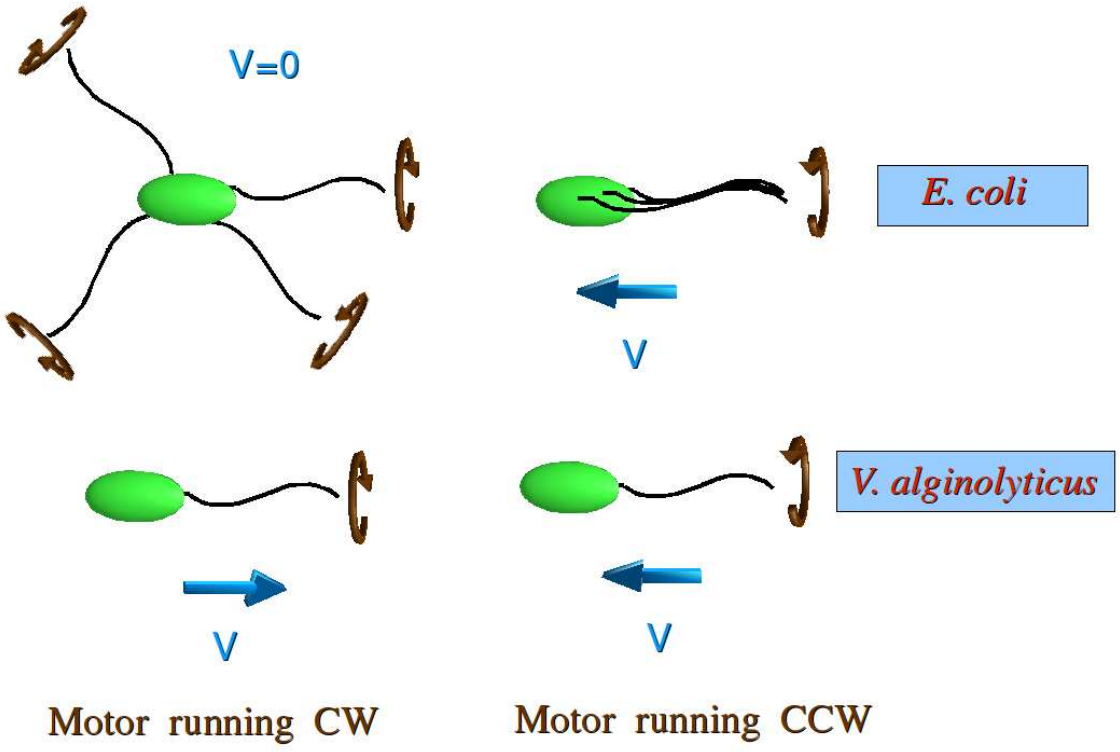

Figure 1.1: Types of bacterial flagellation.

Bacteria may possess single or multiple flagella. Cells of *E. coli* have several filaments spread over the cell body. When motors rotate counter-clockwise filaments move independently, making the cell body wobble without any net velocity. A reversal in the motor direction bundles up individual flagellum making the cell move forward. The bacterium *V. alginolyticus*, on the other hand, has a single flagellum at a cellular pole, a reversal in the rotation direction of which, makes the cell backtrack its path.

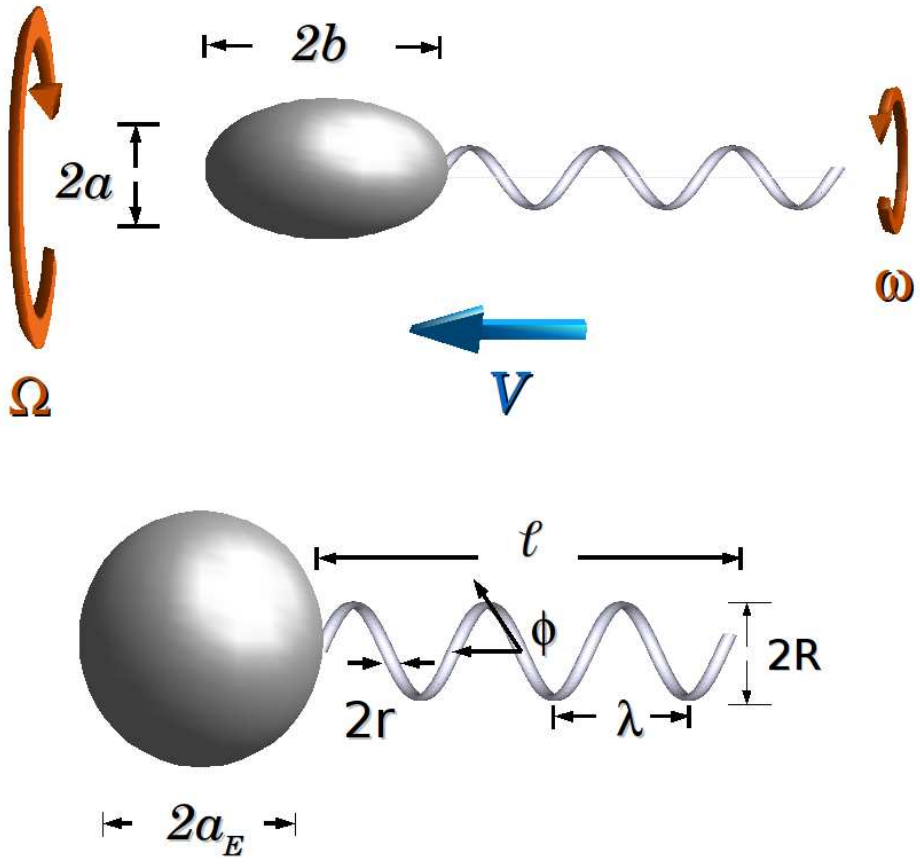

Figure 1.2: Bacterial dynamical and geometric parameters.

The bacterial flagellum rotates with a rate of ω, making the cell body counter-rotate to conserve angular momentum. The thrust produced by the flagellum pushes the cell forward with speed V. The ellipsoidal cell body has major and minor axes of $2b$ and $2a$ respectively. The geometrical parametrization of the cell is depicted, with the dimensions of the flagellum being specified by the wavelength λ, the helix radius R, the filament radius r and the helix length ℓ. The ellipsoidal head is replaced by a sphere of the same linear drag to simplify calculations. Typical values are $a_E \approx 1\,\mu m$ and $\ell \approx 6\,\mu m$.

1.1.2 Bacterial Motor

The bacterial motor is a very advanced micro machine which runs by the flow of ions. The cell maintains an electric potential across its membrane (called the membrane potential) which enables ions to move through the motor from the cell exterior, converting electrical energy to mechanical work. The motor is embedded in the cell membrane and is coupled to the flagellum via an elastic linkage, called the hook (Fig. 1.3). The hook is flexible allowing the flagellar filament to bend at its base during bundle formation. The hook also acts as a buffer between the motor and flagellum storing some of the energy being transmitted [57].

Bacteria often differ in the type of ions driving its motors, which often reflects the environment in which the particular species has evolved. *V. alginolyticus*, which is a marine bacterium, uses Na^+ ions while *E. coli*, found in soil and the animal intestine, runs its motors by H^+ ions, at rotation speeds typically around $200\,Hz$. It is further known that sodium driven motors generally run faster with frequencies reaching up to $1\,kHz$ under optimal conditions [39].

1.1.3 Flagellar Structure

The flagellum is composed of protein subunits which form an ordered repeated structure imparting helicity [40]. Being rigid these filaments do not change conformation unless a large stress is applied. On the application of a high load the flagellar segments can realign to change its wavelength [54]. Some bacterial strains such as *V. alginolyticus* possesses a sheath that covers the filament and is believed to be an extension of the cell membrane. It is not known whether this membrane rotates or is stationary with respect to the flagellum.

1.1.4 Chemotaxis

Among functions possessed by bacteria, chemotaxis is one of the most studied and well understood. Cells are able to perform a random walk in order to search for nutrients. Sensors on the cell body enable the detection of chemical gradients directing flagellar rotation accordingly. If a positive gradient is detected, cells tend to continue forward motion, on the other hand, if no gradient or a positive gradient of a toxin is detected, swimming direction is randomized. Repeated application

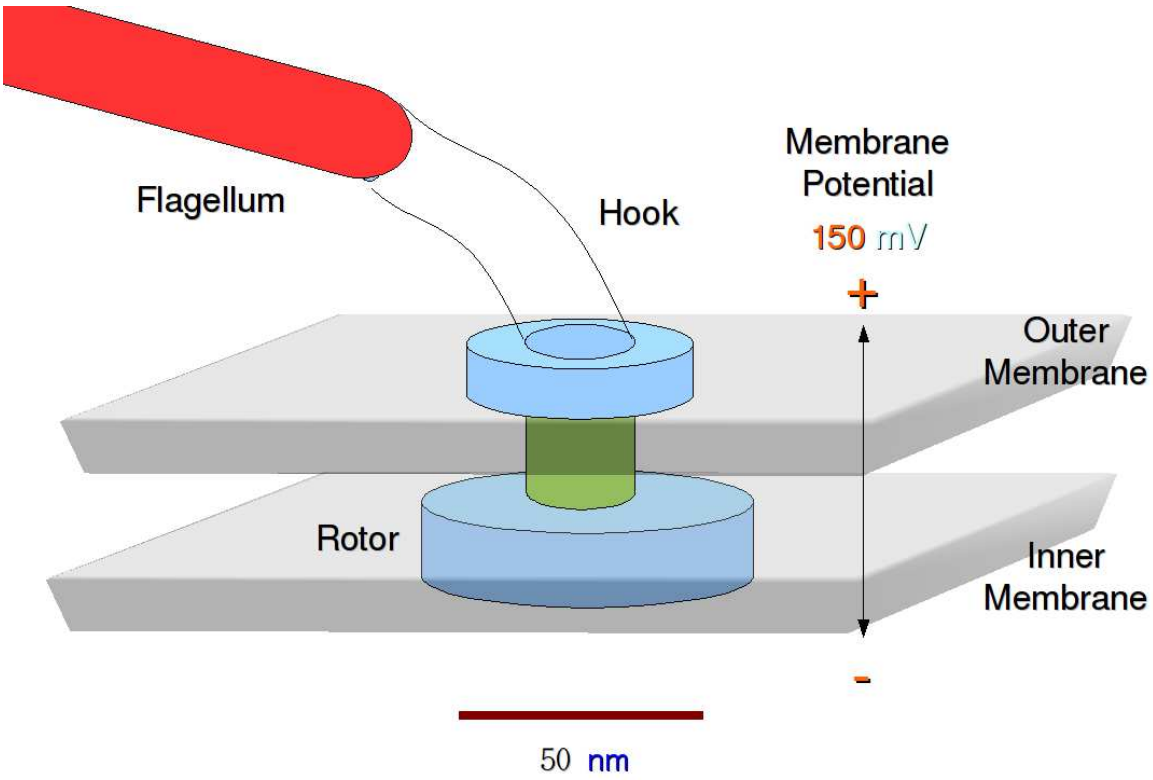

Figure 1.3: The bacterial motor.

The bacterial motor is embedded in the cellular membrane, with a potential difference ($\sim 150\,mV$ for *E. coli*) across it driving the rotor. An elastic linkage, called the hook, forms the interconnection between the motor and the flagellum. The flexibility of the hook helps flagella bundle in multi-flagellated cells.

of this sequence helps the cells to perform a three dimensional random walk to look for favorable regions.

Due to small size and a habitat strongly influenced by thermal fluctuations, bacteria have to increase signal to noise ratio by integrating chemical signals [45]. As a part of this work, I have observed a previously unknown mode of direction change, used for chemotaxis by the marine bacterium *V. alginolyticus*, in which cells are able to use their only flagellum to changes cell orientation, which is discussed in detail in Chapter 6.

2.0 SETUP

2.1 OBJECTIVE AND ISSUES

Bacteria have been studied exhaustively for the past century leading to the knowledge of a lot of intricate details [2, 11, 8, 40, 41]. A thorough discussion is beyond the scope of this thesis, and matters pertaining to swimming and chemotaxis alone will be elaborated on. The chemotactic machinery has been probed deeply with in depth knowledge being available for its genetic network and participating proteins. The bacterial motor is also well studied [10, 41] with detailed information of the components along with the torque-speed properties being known [17, 49].

The issue of the measurement of dynamical variables of bacterial swimming at the single cell level, is however challenging, primarily due to the small size of these organisms. The lack of an experimental tool that can measure and manipulate the bacterium without restricting its motion has limited the progress in understanding the propulsion mechanism. Among bacterial dynamical variables, the swimming speed (V) can be very easily measured by video microscopy, but others, such as rotation rates of the cell body (Ω) and flagella (ω) are more difficult to measure. The primary contribution of this work is to devise a new technique which measures properties of bacterial propulsion accurately and conveniently at the single cell level with the aid of optical tweezers. The basic methodology and instrumentation are discussed in the following sections with further details being furnished in Chapter 7.

2.2 OPTICAL TRAP

The principal tool used in my setup is an optical trap which is formed by focusing a single mode laser beam using a microscope objective [5, 56]. The combined effect of a tightly focused laser beam and the Gaussian profile of a single mode laser, traps an object which has a higher refractive index than the surrounding medium (Fig. 2.1). The interaction of the object with the laser beam can be examined by either ray optics (when object size is much larger than the wavelength of light) or electromagnetic wave theory (when the particle size is comparable to or smaller than the beam wavelength). For the latter case, the trapped object can be treated as an electric dipole in an inhomogeneous field [4]. The ray optics approach is simpler to visualize and is depicted in Fig. 2.1.

The setup consists of additional instrumentation which enables measurement by manipulating the cell appropriately. Figure 2.2 is the depiction of the experimental setup. The flow chamber contains bacteria in a fluid. Syringe pumps and linear actuators are used to produce flows and translate the chamber with respect to the trap. In addition, a piezo actuator is able to move the chamber to change the focal point of the objective. After passing through the sample chamber the beam is collected by an optical condenser and projected onto a position sensitive detector (PSD), which records fluctuations in the position of trapped objects. A Charged Coupled Device (CCD) camera is used to record video images via bright-field microscopy. Live video is used to monitor the sample chamber to facilitate the experiment. All devices are controlled via a computer through the use of a data acquisition card (DAQ) . The signal from the PSD is acquired by the same card.

Optical traps have been used widely for the past two decades, and as a result there have been prior attempts to trap bacteria, with the measurement of dynamics in mind [47]. However, it was observed that cells typically get trapped along the optical axis, as depicted by Configuration B in Fig. 2.3. This makes it difficult to measure the thrust force, as it now moves along the imaging direction, which has low spatial resolution. I realized that cells could instead be trapped perpendicular to the optical axis by either having it close to a surface (Configuration A in Fig. 2.3) or with the imposition of a flow in the bulk medium (Configuration C). This allows greater resolution for displacement measurements, along with convenient manipulation via the modulation of flow, in order to probe various properties. The specific procedures adopted for the measurements

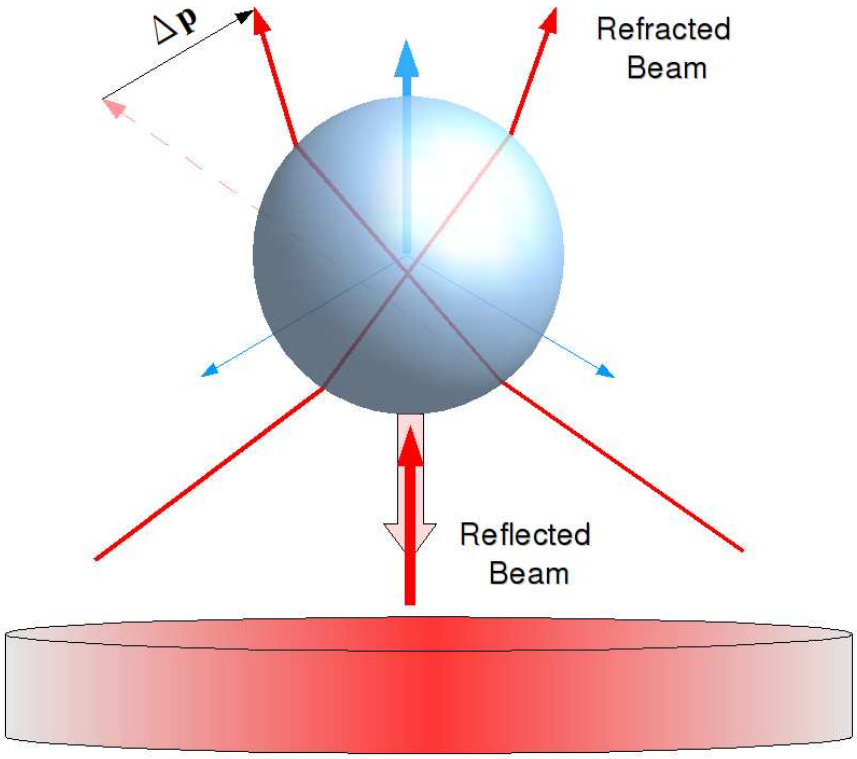

Figure 2.1: Forces in an optical trap.

The ray optics approach to understand the forces on a trapped objects, with size much larger than the wavelength of light being used. The refracted beams impart momentum onto the bead, which are depicted by the blue arrows. The central part of the beam (dark red arrow) is reflected (light red arrow), imparting a force along the optical axis. These forces balance each other, forming a stable trap. The intensity profile of the beam is depicted by the shaded slab at the bottom.

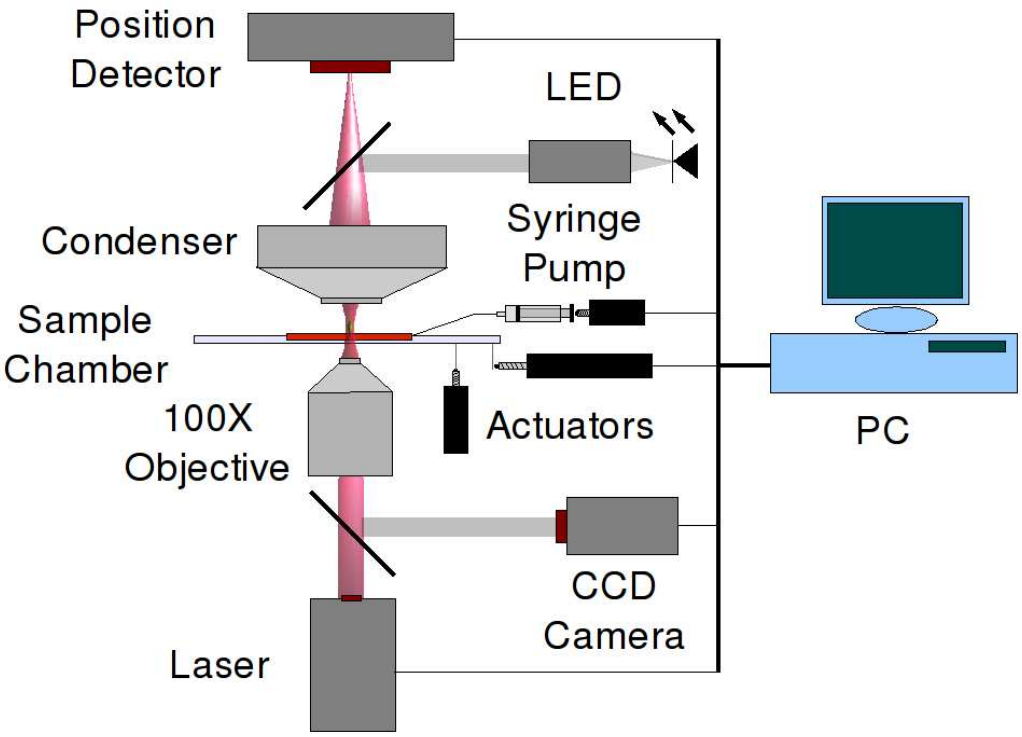

Figure 2.2: Experimental setup.

A diagrammatic depiction of the experimental setup. A laser beam is focused by a 100× objective, which traps particles in the sample chamber. The diverging beam is then collected by an optical condenser and refocused onto a position sensitive detector (PSD). Visible light illuminates the sample, which is viewed by a CCD camera. Actuators are used for translations along all axes, with a syringe pump providing flow in the chamber. Data from the PSD and camera are collected by a PC, which also controlls all instruments via analog signals output from a data acquisition card.

are described in the following chapters.

2.2.1 Detection of bacterial rotation in the optical trap

Rotation of the flagellum shows up as disturbances in the cell body. The bacterial body is further not completely symmetric with respect to the flagellar axis, allowing its rotation to be measured. Thus information on both the rotation rates can be obtained by monitoring fluctucations in the cell body.

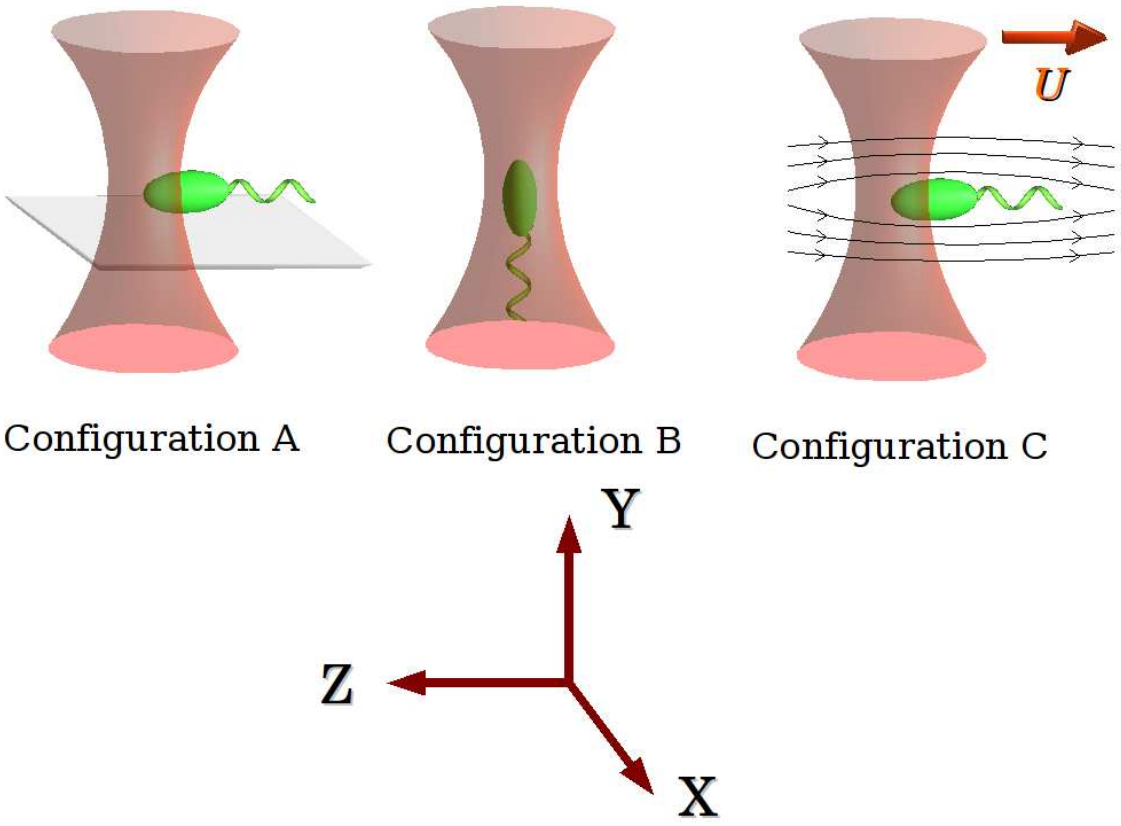

Figure 2.3: Bacterial trapping configurations.

Bacteria trapped via different configurations where the hourglass shape depicts the focussed laser beam. Configuration A occurs near a surface, when the cell remains horizontal due to steric effects. While in the fluid bulk with no applied flow, the cell aligns with the optical axis, as this is the most stable configuration. An applied flow is able to hold the cell perpendicular to the beam even when away from a surface.

3.0 SWIMMING EFFICIENCY OF BACTERIUM *ESCHERICHIA COLI*

3.1 INTRODUCTION

Bacteria swim by rotating helical propellers called flagellar filaments. For *E. coli*, these filaments are several microns in length, 20 nm in diameter and organized in a bundle of three or four [36]. Many important properties of the swimming bacteria, such as their average swimming speed, the rotation rate of the flagellar bundle, and the torque generated by the molecular motor, have been determined [48, 40, 42, 36, 17]. Other properties such as the translational and rotational drag coefficients of intact flagellar bundles, however, are difficult to measure especially for individual cells. These parameters are significant for quantitative understanding of bacterial propulsion and are the subject of extensive mathematical analysis and computer simulations [53, 35, 22, 18, 45]. In this Chapter, I investigate the fundamental swimming properties of intact *E. coli* using optical tweezers and an imposed external flow. The propulsion matrix, which relates the translational and angular velocity of the flagella to the forces and torques propelling the bacterium, can thus be determined one bacterium at a time. My experimental technique is versatile and can be used to make comparative studies of bacteria under different growth conditions, mutant strains of the same species, or different micro-organisms. Such measurements can shed new light on how this remarkable ability to swim evolves among different micro-organisms.

3.2 THE PROPULSION MATRIX

Bacterial swimming occurs at very low Reynolds numbers ($Re \simeq 10^{-5}$) such that the fluid motion is governed by Stokes flow and non-linearity in the full hydrodynamic equation is irrelevant. For

peritrichously flagellated bacteria (having multiple flagella) such as *E. coli*, the flagellar bundle may be approximated as a single effective propeller. Despite these simplifying features, the problem remains theoretically difficult due to complicated time-dependent boundary conditions. For stringent modeling of flagellar propulsion one must rely on numerical methods [46]. A second approach is not to take into account specific geometries but to consider general relations appropriate in the low Reynolds-number limit as done by Purcell, using the propulsion matrix formulation [45]. In this regime, the torque N acting on the propeller (generated by the motor) and the thrust force F_{thrust} generated by it (F_{thrust} which pushes the cell body forward) are linearly related to the propeller's angular velocity ω and the translational velocity V (relative to the background fluid):

$$-F_{thrust} = AV - B\omega \tag{3.1}$$

$$N = -BV + D\omega \tag{3.2}$$

The forces are depicted in Fig. 3.1 with the sign of ω and N obeying the right-hand rule with the flagellar filament being a left-handed helix. We deal with the magnitude of quantities with appropriate signs being accounted for. The above equations can be expressed in terms of the propulsion or resistance matrix for the flagellum $P = \begin{bmatrix} A & -B \\ -B & D \end{bmatrix}$ [24]. The coefficients A, B, and D are positive, proportional to fluid viscosity η, and depend on the shape and size of the propeller. The basic physics is, that in the absence of an externally applied torque, a translating propeller under the influence of an external force must rotate, and in the absence of an applied force, a rotating propeller under the influence of an external torque must translate [45].

The propulsion matrix description is applicable to propellers of any shape and size. However, for a rigid helical coil, the matrix elements can be derived from resistive force theory [35] which are given in Eqn. 5.6. To complete the description of the swimming bacterium, we need the propulsion matrix P_0 for the cell body. Unlike P for the flagellum, P_0 is diagonal ($B_0 = 0$) since the cell body cannot propel itself. The non-viscous force on the cell body consists of two parts, the trapping force F_{trap}, due to the optical tweezers holding the bacteria and the thrust F_{thrust} generated by the flagellum. The sum of these forces must balance the viscous force $A_o V$ acting on the cell body.

Likewise, the non-viscous torque acting on the cell body N must balance the viscous rotational drag. This gives:

$$F_{trap} + F_{thrust} = A_0 V, \tag{3.3}$$

$$D_0 \Omega = N, \tag{3.4}$$

where Ω is the angular velocity of the cell body. I treat the cell body as a prolate ellipsoid with minor semi-axis a and major semi-axis b. If the cell body is in the bulk of the fluid, the linear and rotational drag coefficients are then $A_0 = 4\pi\eta\ b/(\ln(\frac{2b}{a}) - \frac{1}{2})$ and $D_0 = 16\pi\eta a^2 b/3$ [9]. The optical trapping force is harmonic $F_{trap}(z) = -k(z - z_0)$, where k is the spring constant and $z - z_0$ is the displacement from the center of the trap [56, 44]. When the bacterium is held by the optical tweezers, its net velocity in the lab frame is zero ($V' = V + U \simeq 0$), and the relative velocity V to the fluid is opposite to the external flow U. Substituting $V = -U$ into Eqn. 3.1 and 3.4 gives,

$$k(z - z_0) = (A + A_0)U + B\omega, \tag{3.5}$$

$$D_0 \Omega = BU + D\omega. \tag{3.6}$$

This set of equations will be used below to analyze my data. These equations can also be written for the case when cells are free swimming with a speed V, giving,

$$(A + A_0)V = B\omega \tag{3.7}$$

$$D_0 \Omega = -BV + D\omega \tag{3.8}$$

Equation 3.8 inspired me to think of an equivalent electrical circuit for the bacterial flagellar apparatus, which is discussed in Appendix D.

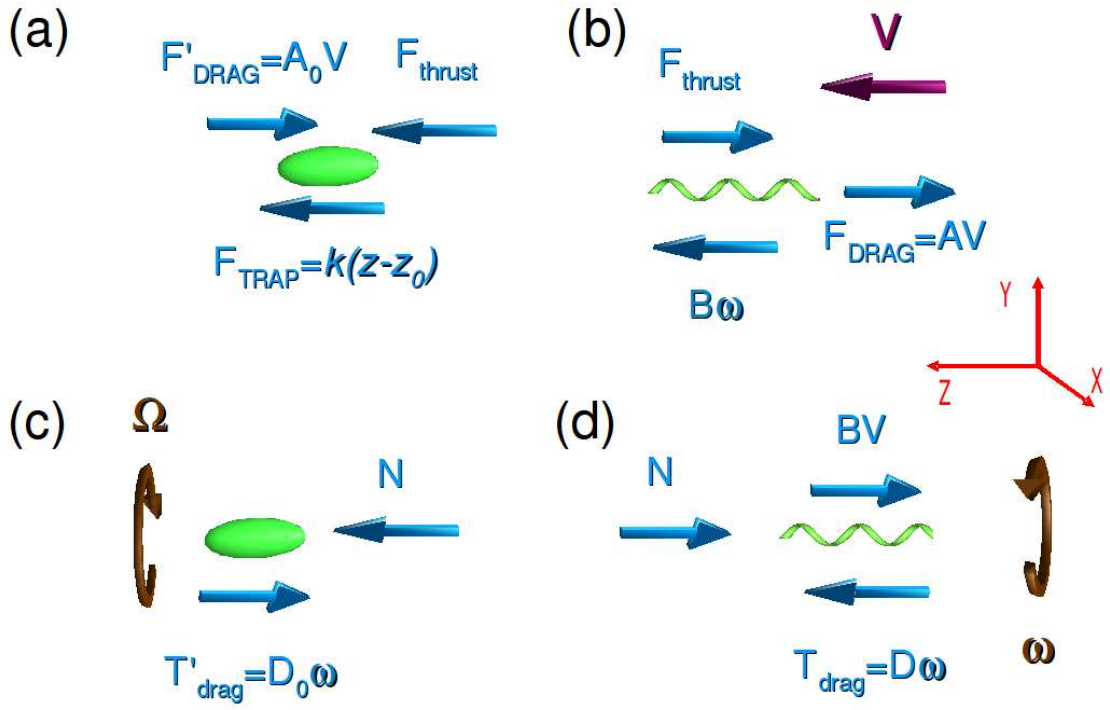

Figure 3.1: Force and Torque Balance for the bacterium. All forces are taken as magnitudes with the directions shown by arrows.

(a) The cell body is pushed with F_{thrust} by the flagellum and swims forward with V leading to a viscous drag of A_0V. The trap force is taken to be in the positive Z direction in the situation indicated. (b) The flagellum pushes on the fluid in the negative Z direction with a force $B\omega$ leading to a reaction force of same magnitude on itself while it is resisted by the reaction F_{thrust} from the cell body and a drag force (AV). (c) The torque produced by the motor N acts on the cell body and is balanced by the viscous drag. (d) The motor drives the flagellum with a torque of N in the negative Z direction which rotates the helix. The helicity of the flagellum produces a torque due to the linear motion (BV) along negative Z.

3.3 RESULTS

I used a non-tumbling strain of *E. coli,* HCB30, in our measurements (See Chapter 7 for further details). An individual bacterium is trapped near the lower glass surface via Configuration A (see Fig. 2.3). The cell is then manipulated by an imposed uniform external flow U. A non-flagellated bacterium (YK4516) was used to calibrate the spring constant k of the optical trap. A description of the calibration procedure is presented in Chapter 7.

Figure 3.3 displays an example of the time trace $z(t)$ of the longitudinal displacement of the trapped cell tip along the swimming direction of the bacterium. I observed large oscillations overlying a systematic variation of $z(t)$ as the external flow is changed. These oscillations result from wobbling of the cell body in response to the rotation of the flagellar bundle [47, 36]. The trapped bacterium was perturbed by the following sequence of events: In Regime I, U is linearly reduced from $-40\,\mu m/s$ to zero in $3\,s$. If the flow speed $|U|$ is larger than the free swimming speed V, the bacterium is trapped at the head and $z(t) < 0$ (Fig. 3.2(a)). When $|U| \leq V$, the bacterium swims forward, becomes trapped at the tail of the body (Fig.3.2(b)) and $z(t) > 0$. The zero crossing point ($z(t) = 0$) occurs precisely when $|U| = V$. In Regime II, U is maintained at zero for 4 s, and the average position of the bacterium relative to the trap is constant. Finally in regime III, the bacterium is released by temporarily blocking the laser beam. The position of the undeflected beam in Regime III is taken to be z_o, the center of the optical trap. From Regime I, the net translational drag coefficient $A + A_0 = k\Delta z/\Delta U$ is obtained, and in Regime II, I obtain F_{thrust}, since $F_{trap} = -F_{thrust}$ when $U = 0$. I checked that the measurement was reproducible by returning the flow to $U = -40\ \mu m/s$ rather than releasing the bacterium after Regime II. The bacterium returned to within a few percent of its initial average position.

I used transverse oscillations $x(t)$, which were more pronounced than $z(t)$, to obtain the angular velocity of the cell body and of the flagellar bundle. Figure 3.4(a) displays a sample power spectrum $E(f)$ of $x(t)$ for a short time interval of 4s when $U = 0$. The power spectrum has two strong peaks at $f_L \simeq 25\ Hz$ and $f_H \simeq 124\ Hz$, respectively. These two frequencies can be associated with the angular velocities of the cell body $\Omega = 2\pi f_L$ and of the flagellar bundle $\omega = -2\pi f_H$ [47]. Averaging over 200 bacteria, I found $\bar{f_L} = (19.6 \pm 0.3)\ Hz$ and $\bar{f_H} = (115 \pm 2)\ Hz$, where the standard errors of the mean are quoted. As shown in Fig.3.4(c-d), there is considerable variation

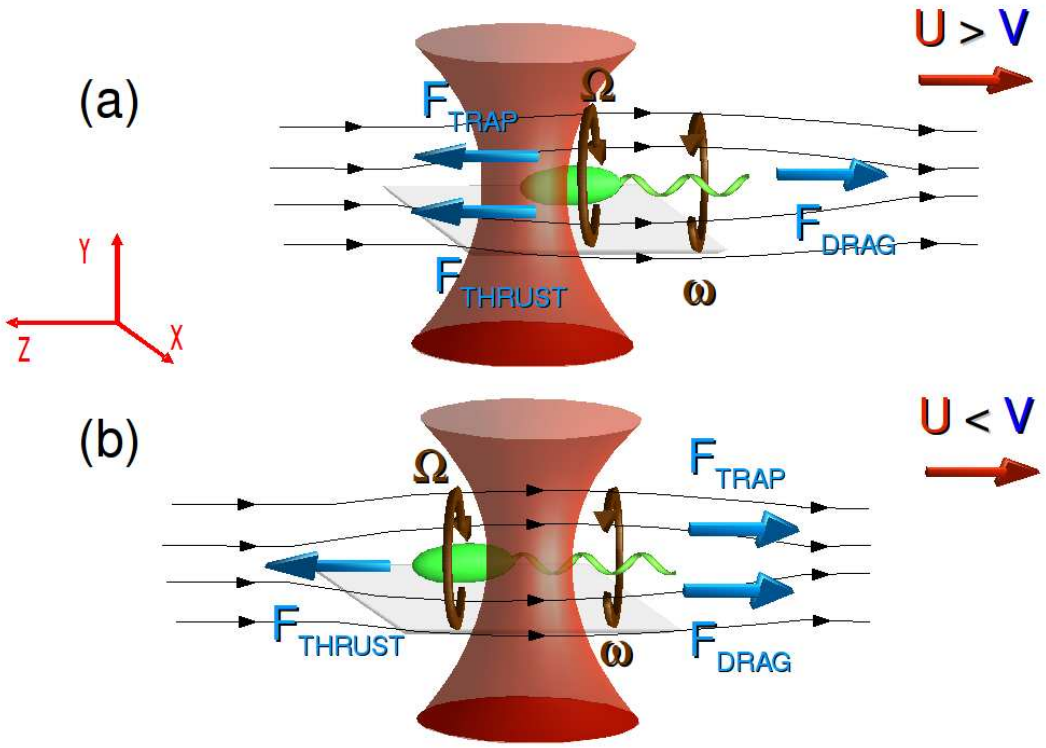

Figure 3.2: Trap configurations near a surface.

Various ways by which a bacterium can get trapped near a surface. Shown are the forces and torques on the cell body. When (a) the external flow (U) exceeds the swimming speed (V) of the bacterium the cell is trapped in the forward tip. (b) Flows lower than V, however, holds the rear tip of the bacterium.

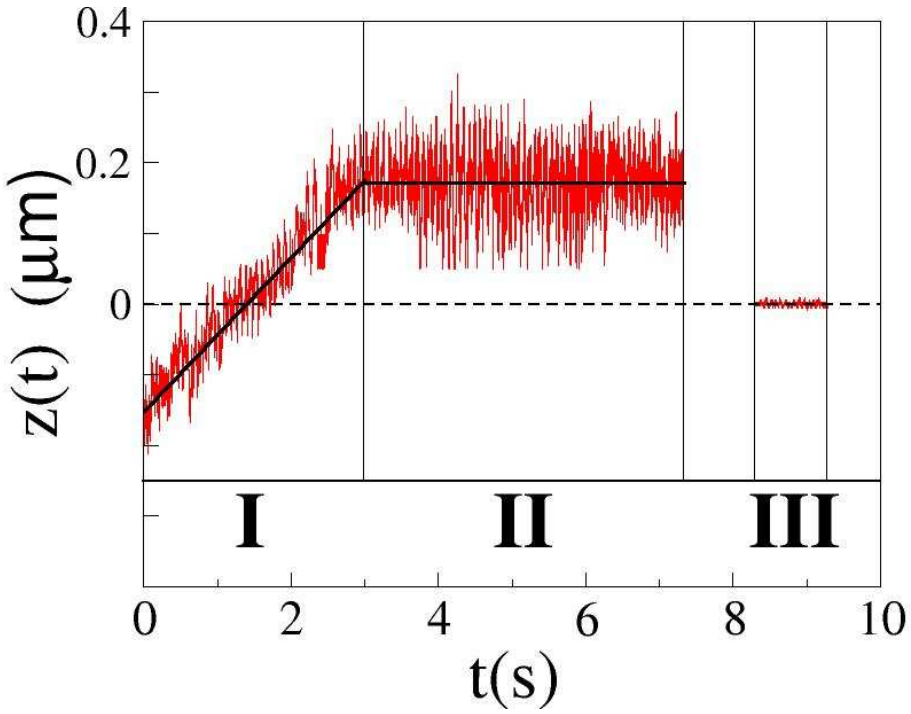

Figure 3.3: Data for an experimental run for *E. coli.*

A typical experimental run for a swimming bacterium held in the optical trap. In Regime I, an uniform flow $U = -40\ \mu m/s$ is decreased to zero linearly with time. The flow U remains zero in Regime II. The laser is blocked momentarily to let the bacterium escape and the undeflected laser beam position is recorded in Regime III. The solid lines depict linear fits to each regimes.

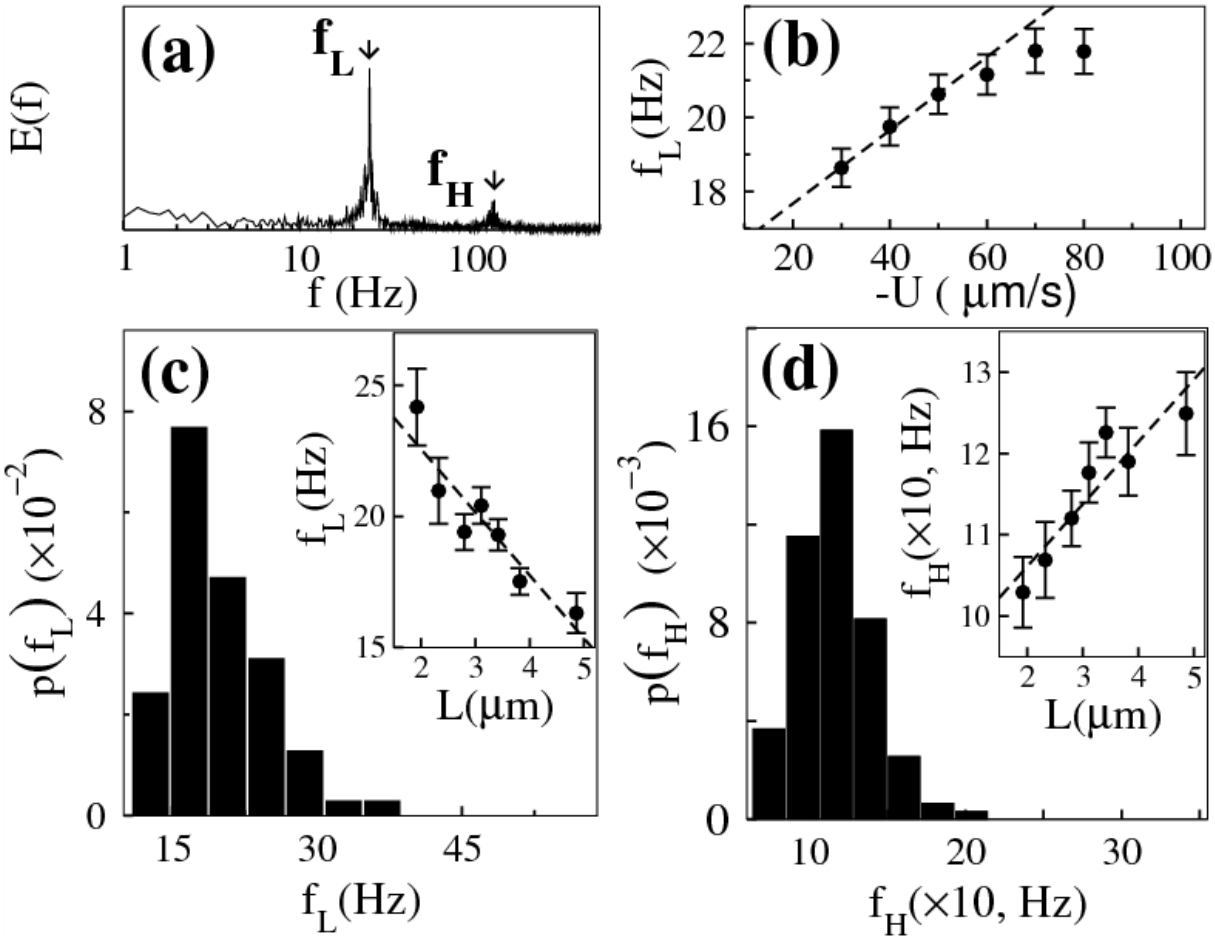

Figure 3.4: Dynamical variables of trapped cells.

(a) Power spectrum of $E(f)$ of $x(t)$ shows peaks corresponding to f_L and f_H. (b) The variation of the rotation frequency of the cell body f_L as a function of flow speed $-U$. The linear dependence is consistent with the propulsion matrix formulation. Error bars are standard errors of the mean unless otherwise noted. The PDFs of f_L and f_H are delineated in (c) and (d), respectively. The insets show the average f_L and f_H as a function of cell-body length L.

of f_L and f_H between individual bacteria; the standard deviations $\sigma_{f_L} = 5.4$ Hz and $\sigma_{f_H} = 25$ Hz are respectively 28% and 22% of the mean values. As suggested by insets of Fig. 3.4(c-d), some of the variation is due to dependence of f_L and f_H on the cell-body length $L \equiv 2b$; namely the cell-body rotation frequency f_L decreases while the flagellar rotation frequency f_H increases as L is increased. Since the motor angular velocity is defined as $\Omega_m \equiv \Omega + \omega = 2\pi(f_L + f_H)$, I found that Ω_m increases slightly with L.

To test the basic physics implied by the propulsion matrix, I measured the dependence of f_L and f_H on U for an additional 150 bacteria which were subjected to flow speeds of $-U = 30, 40, 50, 60, 70$ and 80 $\mu m/s$. Figure 3.4(b) shows that the average frequency $\bar{f_L}$ increases linearly with small $|U|$ but the rate of increase decreases considerably for $|U| > 60\,\mu m/s$. The linear dependence for small $|U|$ is in good agreement with Eqn. 3.6, which is an essential property of the propulsion-matrix formulation. The deviation for large $|U|$ represents a nonlinear response of the cell to the flow and is likely due to deformations of flagellar bundles at a high speed. Within the noise of the measurement, no systematic change in $\bar{f_H}$ was detected.

To complete my determination of the propulsion matrix, the semi-minor axis a and the length $L = 2b$ of the bacterial cell body were measured directly by video microscopy while the bacterium was held in the trap. This allows me to calculate the drag coefficients A_0 and D_0 for the cell body. However, since the bacteria were trapped approximately $d \simeq 5\,\mu m$ above a solid surface, wall effects must be taken into account. Using the analysis of Brenner [24], the wall corrections to the drag coefficients are given by an expansion in terms of the ratio of the characteristic body size L to the distance d from the wall with the result $A_0 \simeq A_0(\infty)[1 - \kappa_1 A_0(\infty)/(6\pi\eta d) + O(L/d)^3]^{-1}$ and $D_0 \simeq D_0(\infty)[1 - \kappa_2 D_0(\infty)/(8\pi\eta d^3) + O(L/d)^5]^{-1}$. Here $A_0(\infty) = 2\pi\eta L/(\ln(\frac{L}{a}) - \frac{1}{2})$ and $D_0(\infty) = 8\pi\eta a^2 L/3$ are the bulk values when $L/d \to 0$, and $\kappa_1 = 9/16$ and $\kappa_2 = 1/8$ are constants. A straightforward calculation based on our experimental geometry shows that A_0 and D_0 are increased by 13% and 4% respectively from their bulk values due to the surface. This indicates that the surface effect, though not negligible, is not significant enough to qualitatively alter the propulsion-matrix representation. In other word, we expect that the linear relation in Eqs. 3.5 and 3.6 still hold approximately and the values of A, B, and D are moderately different from their bulk values. From the time trace $z(t)$, A and B are calculated by $A = k\Delta z/\Delta U - A_0$ (Regime I) and $B = F_{thrust}/\omega$ (Regime II). Finally, the measurements of the angular velocities give $D \approx (\omega/\Omega)D_0$.

The calculations were repeated for the 200 bacteria and the average values obtained are summarized in Table 3.1. The translational drag coefficient of the flagellar bundle is approximately equal to that of the cell body ($\bar{A_0} = 1.4 \times 10^{-8} N\ s/m$). Therefore about half of the drag on the bacteria is due to the flagella. On the other hand, the rotational drag of the flagella $\bar{D}$ is much smaller than that of the cell body ($\bar{D_0} = 4.2 \times 10^{-21} N\ s\ m$).

All important dynamical quantities can be obtained from my measurements. For example, the average thrust for $U = 0$ is $\bar{F}_{thrust} = \bar{B}\ \bar{\omega} = 0.57\ pN$, while the average torque is $\bar{N} = \bar{D}\ \bar{\omega} = 5 \times 10^{-19} N\ m$, which is close to that found elsewhere [20]. The calculated mean swimming speed $\bar{V} = \bar{B}\ \bar{\omega}/(\bar{A}_0 + \bar{A}) = 20.4\ \mu m/s$ agrees well with direct measurements of the average swimming speed using video microscopy, $\bar{V} \approx 22\ \mu m/s$. Additional measurements further showed that $\bar{V}$ was the same before and after trapping, indicating minimal photo effects in this horizontal trapping configuration. The value of the trap constant used was measured to be $k = 5.7 \times 10^{-6} N/m$.

The propulsion matrix elements vary greatly among individual bacteria even though they were grown from a single colony. Figure 3.5 displays the probability distribution functions (PDF) of the scaled quantities $A/\bar{A}$, $B/\bar{B}$, and $D/\bar{D}$. The standard deviations σ are significant fractions of the means with $\sigma_A/\bar{A} \simeq 40\%$, $\sigma_B/\bar{B} \simeq 37\%$, and $\sigma_D/\bar{D} \simeq 27\%$. A conspicuous feature of the PDFs is their broad tails, particularly for A and B. This might be an indication of structural heterogeneity in the flagellar bundles of individual cells or that the conformation of the bundles changes with time. As is often the case in biological systems, the PDFs with broad tails can be roughly fitted to log-normal distributions that are plotted as solid lines in Fig. 3.5(a-c).

Part of the variations in A, B and D must arise because the bacterium are in different stages of their growth cycle during the measurements. This is especially the case for the early-log phase ($\sim 3.5 hrs$ growth time) of a growing culture, where the bacterial size is large and highly varied. In the current experiment, the bacteria were grown to the mid-log phase ($\sim$4.5 hrs growth time), where cells are smaller and their size distribution is narrower. However, even at this stage the cells are far from homogeneous. Figure 3.6(a) shows the cell-length distribution of the group of 200 randomly selected bacteria. The fitted PDF (solid line) is peaked at $\sim 3\,\mu m$ with a standard deviation of $0.8\,\mu m$. The figure also shows the smallest cell length L_0 at which a septal ring becomes discernible. I used the bacterial length L as a measure of its physiological state and determine the propulsive matrix elements as a function of L. To improve the statistics for large L, a

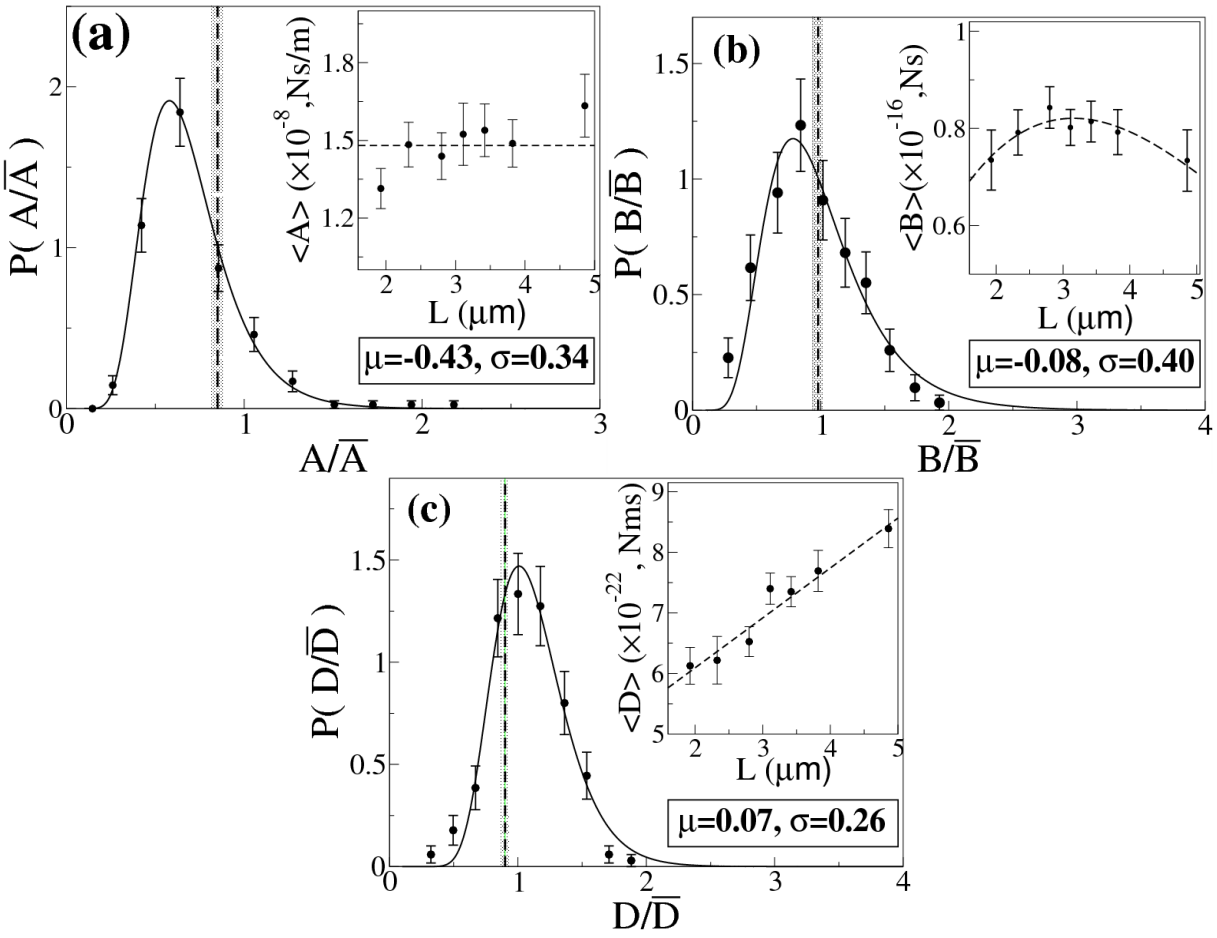

Figure 3.5: PDFs of A, B and D for *E. coli*.

The PDFs of $A/\bar{A}$, $B/\bar{B}$, and $D/\bar{D}$. The solid lines are fits to the log-normal distribution $P(x) = \exp[-(\ln x - \mu)^2/2\sigma^2]/(x\sigma\sqrt{2\pi})$. The fitting parameters μ and σ are given in the plots. The respective insets show the bacterial length L dependence of $\bar{A}$, $\bar{B}$, and $\bar{D}$. The vertical lines are calculations by Resistive Force Theory by Gray and Hancock [22]

centrifugation technique was used to select long bacteria ($4 < L < 6\,\mu m$, $n = 50$). I determine the length dependence of the coefficients A, B, and D by calculating the averaged values $\langle A \rangle$, $\langle B \rangle$ and $\langle D \rangle$ for bacteria of similar length L. The results are presented in the insets of Fig.3.5. The linear drag coefficient $\langle A \rangle$ has no clear size dependence but $\langle B \rangle$ has a small peak at $L \approx 3.3\ \mu m$, which coincides with the peak of the bacterial size L distribution. On the other hand, Fig. 3.5(c) shows that the rotational drag coefficient $\langle D \rangle$ of the propeller increases linearly with L.

These size dependencies allow us to draw certain conclusions about the structure of flagellar bundles at different stages of cell growth. Inspection of Eqs. 5.6 shows that the three matrix elements are similar in their dependence on parameters such as the pitch angle ϕ (or β) and γ_k. Such similarity precludes the possibility that β and γ_k are controlling the different L dependencies seen in the measurements. On the other hand, the matrix elements depend strongly on the pitch λ with $A \propto \lambda^0$, $B \propto \lambda^1$, and $D \propto \lambda^2$. These relationships correlate with the observation that A has the least and D the most L dependence. The observation therefore implies that the primary L dependence is via the pitch λ. One may thus conclude that both β and γ_k are approximately constant for different sized bacteria, which is physically and biologically reasonable (the wavelength and radius depend on the size of protein subunits which do not change). Since our measurements show a linear relation between D and L, one can also conclude that λ^2 grows linearly with L. A possible scenario is that as the cell body elongates, more flagella are incorporated into the bundle and consequently its stiffness and λ increase. From the shortest to the longest bacterial body length $(2-5\,\mu m)$, I found that the fractional change $\delta\lambda/\lambda$ should be about 18%, which may be discernible in carefully conducted observations using fluorescently labeled bacteria.

I next turned my attention to the power and propulsive efficiency of the swimming bacteria. The average power output of the flagellar motors is $\bar{\Sigma} = \bar{D}_0 \bar{\Omega} |\bar{\omega} - \bar{\Omega}| = 4.3 \times 10^{-16}\ W$. The power used to turn the cell body is $\bar{D}_0 \bar{\Omega}^2 \approx 6.3 \times 10^{-17}\ W$ while the actual propulsive power is another factor of ten smaller with $\bar{A}_0 \bar{V}_{swim}^2 \approx 5.8 \times 10^{-18}\ W$. Therefore $\sim 15\%$ of the rotary power is used to rotate the cell body, only $\sim 1.3\%$ is used to push the bacterium forward, and the rest is dissipated as heat. Figure 3.6(b) shows the average motor power as a function of bacterial length L. The power increases gradually with L, which is consistent with the above discussion that the number of flagella and the associated motors increase with L. The propulsion efficiency ε, defined as the ratio of the propulsive power to the rotary power, can be related to the propulsion matrix elements

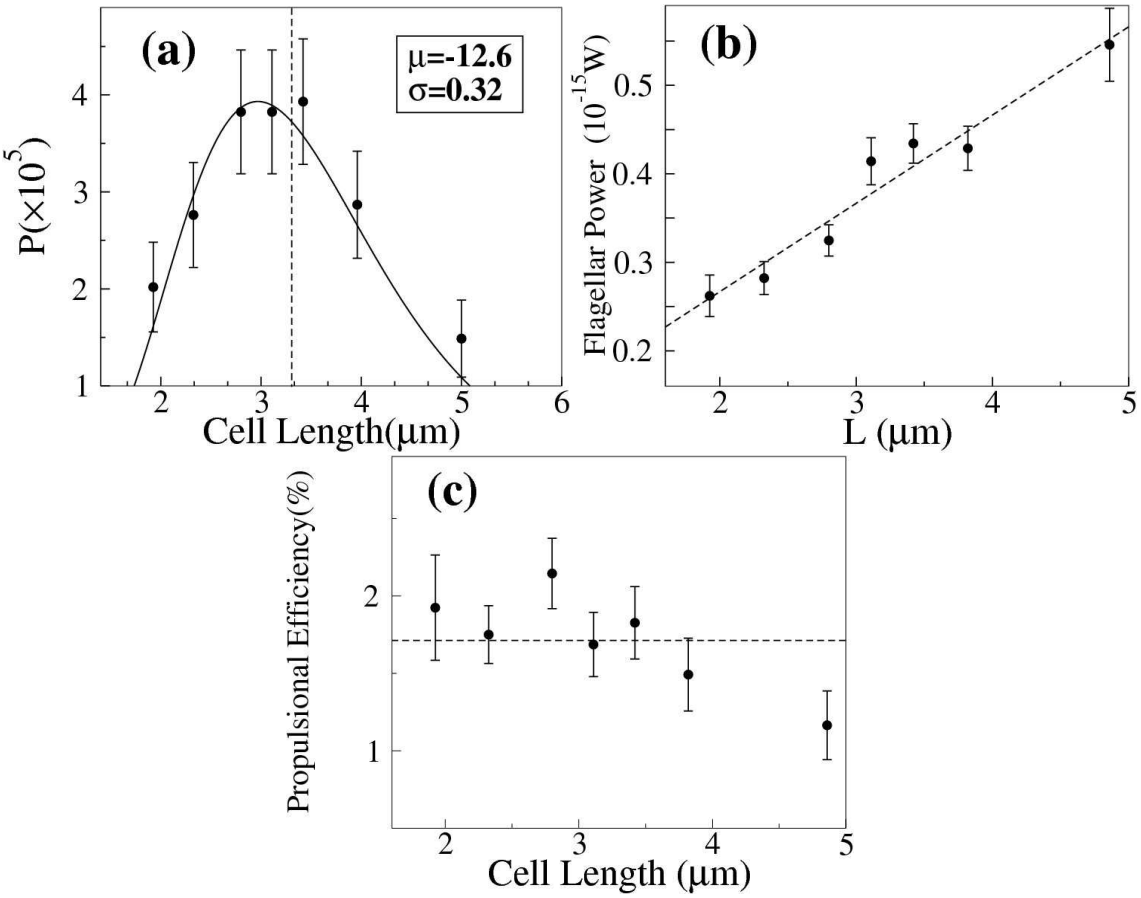

Figure 3.6: Length, power and efficiency for *E. coli*.

(a) The PDF of the bacterial cell length L. The solid line is a fit to the log-normal distribution with the parameters σ and μ defined in Fig. 3.5. The vertical line marks the smallest cell length L_0 at which I observed a septal ring. (b) The flagellar power output $\langle\Sigma\rangle$ as a function of L. The dashed line is a linear fit. (c) The propulsion efficiency $\langle\varepsilon\rangle$ as a function of L. The dotted horizontal line marks the mean efficiency 1.7% of the entire population of 250 bacteria.

[45]

$$\varepsilon \equiv \frac{A_0 V_{swim}^2}{N(\omega-\Omega)} = \frac{A_0 D_0 B^2}{[(A_0+A)D-B^2][(A_0+A)(D_0+D)-B^2]}. \tag{3.9}$$

Figure 3.6(c) shows that the efficiency as a function of bacterial size is nearly constant up to $L \simeq 4\,\mu m$. The average efficiency is $\bar{\varepsilon} \approx 1.7\%$, which is slightly larger than 1.3% estimated above. The discrepancy is due to correlations between A, B, and D of individual cells, i.e., $\varepsilon(\bar{A},\bar{B},\bar{D})$ is not the same as $\bar{\varepsilon}(A,B,D)$ when evaluated using Eqn. 3.9. Our measured efficiencies are surprisingly close to the $1-3\%$ predicted theoretically for a rigid helical propeller [35, 18]. Similar measurements were also carried out for bacteria grown to an early-log phase($\sim 3.5\,hrs$). In this case, though the average swimming speed is about a factor of three lower ($\bar{V}_{swim} \simeq 6\,\mu m/s$), the swimming efficiency reduces by almost a factor of ten with $\bar{\varepsilon} \simeq 0.2\%$. This efficiency is comparable to the $\bar{\varepsilon} \simeq 0.35\% - 0.7\%$ found by Purcell using helical coils made of metal wires [45]. The lower efficiency observed by Purcell is likely due to the sub-optimal pitch angle of the coils used.

I can also ask, for a given A_0, what is the maximum efficiency attainable by the bacterium as a function of the length of the flagellum ℓ. Assume that at some characteristic length ℓ_p, the propulsive coefficients of the flagellum are A_p, B_p and D_p. Assuming that the width of the flagellar bundle is constant, these coefficients should grow linearly with the flagellar length ℓ so that $A \approx \kappa A_p$, $B \approx \kappa B_p$, and $D \approx \kappa D_p$, where $\kappa = \ell/\ell_p$. This assumption is consistent with Eqs. 5.6**.** Substituting for A, B and D into our expression for ε (in Eqn. 3.9) and assuming $B^2 \ll (A_0+A)D$ and $D_0 \gg D$, I find that the maximum efficiency occurs when $A = A_0$ and $\varepsilon_{max} \approx B_p^2/(4A_pD_p)$, which depends only on the shape of the propeller. The same result was obtained by Purcell when he maximized ε by assuming that all propeller dimensions (not just the length) scaled with κ [45]. In my experiment, I found that $\bar{A}$ is approximately equal to $\bar{A}_0$ so that flagella are as long as required to maximize its propulsive efficiency.

3.4 MATRIX ELEMENTS FROM RESISTIVE FORCE THEORY.

Resistive Force Theory (RFT) is a theoretical model which is commonly used by experimentalists to estimate the properties of flagellar propulsion. RFT is discussed in detail in Section 5.1.3. The

theory considers local hydrodynamics only, ignoring effects of long range interactions.

The theoretical expressions for A, B, and D, given in Eqs. 5.6 can thus be used to extract physical parameters of the flagellar bundle if I treat it as a single effective flagellum. This assumption is consistent with the observation that the flow field induced by a model rotating bundle is very close to that induced by a rotating rigid helix of appropriate thickness [30]. The dimensions of the flagellum are measured using fluorescent microscopy as described in Chapter 7 with the measurements summarized in Table 3.2. For a close packing of $3-4$ flagella the filament radius is chosen to be $\approx 2r$, where r is the single filament radius[20]. The values predicted by RFT of Gray and Hancock (See Section 5.1.3) are used for the estimations with the values depicted by vertical lines in Fig. 3.5. I see that the predictions are very close to the experimental measurements.

3.5 SUMMARY

In summary, bacterial propulsion is investigated using an optical tweezers, which allows me to directly measure the thrust force F_{thrust} as a function of the imposed flow. For a free swimming bacterium, F_{thrust} precisely balances the viscous drag of the cell body A_0V and of the flagellar bundle AV. Unlike the viscous drag of the cell body, the contribution of the flagellar bundle to the total drag is difficult to determine without direct force measurements such as the one presented here. I showed that the propulsion matrix proposed by Purcell [45] gives an adequate description of bacterial swimming over a physiological range of velocities. In retrospect, this is not obvious considering that flagellar filaments are tenuous and are deformable due to hydrodynamic stress induced by swimming or by flows [37, 26]. Indeed, my measurements do show nonlinear response to changes in U when a strong flow ($|U| > 3V_{swim}$) is imposed.

Using the propulsion matrix, I have also determined dynamic quantities related to bacterial swimming and their dependence on the size of the cell body. In particular, I found that the propulsive efficiency ε, defined as the ratio of the propulsive power to the rotary power, is $\sim 1.7\%$. This efficiency depends weakly on the bacterial size but strongly on the growth condition. The measured ε is close to the maximum efficiency for the given size of the cell body and the shape of the flagellar bundle. The theoretical estimate for A, B, and D, can then be obtained using dimensions

measured by fluorescent microscopy, while assuming the bundle behaves as a single “effective” filament. I observe that these elements can be sufficiently described by the use of RFT by Gray and Hancock [22].

Table 3.1: Measured dynamical variables for *E. coli* and *V. alginolyticus.*

Bacterial Strain		**Dynamic Variables**								**Matrix Elements**				
Genus	**Name**	n_D	V $(\frac{\mu m}{s})$	$\frac{\omega}{2\pi}$ (Hz)	$\frac{\Omega}{2\pi}$ (Hz)	Torque $(pN \cdot nm)$	Force (pN)	Power (pW)	ε $(\%)$	A $(\times 10^{-8}, N \cdot s/m)$	A_0	B $(\times 10^{-16}, N \cdot s)$	D $(\times 10^{-22}, N \cdot s \cdot m)$	D_0
E. coli	HCB30	200	22(0.4)	120(2)	15(1)	400(10)	0.57(0.02)	4(0.2)	1.8(0.1)	1.5(0.05)	1.4(0.01)	7.9(0.2)	7.0(0.2)	42(0.1)
V. alginolyticus	YM42	140	34(1)	571(12)	26(1)	770(20)	-	26(1)	0.8(0.03)	0.73(0.06)	1.3(0.01)	2.3(0.2)	2.4(0.1)	47(0.1)

Measured dynamical variables for cells of *E. coli* and *V. alginolyticus*. The data for *E. coli* are the same as published in [15]. n_D denotes the number of cells used for the measurement of the dynamics. The uncertainties quoted in parenthesis are the standard errors of the mean.

Table 3.2: Geometrical parameters for *E. coli* and *V. alginolyticus.*

Bacterial Strain		**Cell No.**	**Flagellar Dimensions**				**Cell Size**	
Genus	**Name**	n_G	$\ell(\mu m)$	$\lambda(\mu m)$	$2R(nm)$	$r(nm)$	$a(\mu m)$	$b(\mu m)$
E. coli	HCB30	40	6.2(0.2)	2.3(0.02)	380(5)	12	0.44(0.01)	1.5(0.04)
V. alginolyticus	YM42	40	3.7(1)	1.2(0.02)	280(1)	16	0.35(0.01)	2.3(0.05)

Cellular dimensions as measured for cells of *E. coli* and *V. alginolyticus.* Fluorescent labelling provides dimensions for the flagellum. The cell body size is obtained from video images by bright field microscopy. n_G denoted the number of cells used included for fluorescent imaging. Numbers in parenthesis are standard errors of the mean. Values of r were obtained from Refs. [38] and [20] for *V. alginolyticus* and *E. coli* respectively.

4.0 SWIMMING OF *VIBRIO ALGINOLYTICUS*

In the previous Chapter the use of an optical trap to measure the dynamics of cells of *E. coli* was demonstrated. Certain aspects of the experimental procedure were prone to uncertainties, such as the proximity of the cells to a surface and the presence of multiple flagella. Thus, in order to perform a stringent test of theoretical models of bacterial swimming, it is desirable to avoid such a situation by using modified techniques, which are dealt with in this Chapter.

On attempting various trapping configurations, it was found that an imposed flow is capable of holding bacterial cells perpendicular to the beam, even when it is away from a surface. This is depicted as Configuration C in Fig. 2.3. The instrumentation involved in making this possible is described in Chapter 7. Experiments could now be performed in the fluid bulk eliminating any interaction with surfaces. Furthermore, ambiguities arising from the possible friction between the flagella in a bundle are avoided by switching to a strain which possesses a single polar flagellum. I choose to perform this improved study on *V. alginolyticus*, a marine bacterium that has a single flagellum located at a cellular pole.

While being trapped in Configuration C, the flow speed U can be varied and the bacterial displacement in the flow direction is given by,

$$\Delta z(t) = \frac{(A+A_0)}{k} U(t) + \frac{B\omega}{k}. \tag{4.1}$$

Hence the slope of the linear plot of $\Delta z(t)$ vs. $U(t)$ would provide the value of A and the intercept can provide B (again A_0, k and ω are assumed known). This is aided by the assumption that ω is not effected by moderate changes in the rate of flow. We have observed that an imposed flow negligibly influences the rotational load (and hence the torque) on the flagellum, which aids this assumption. Figure 4.1 depicts the sequence of events for a typical experimental run. A linear

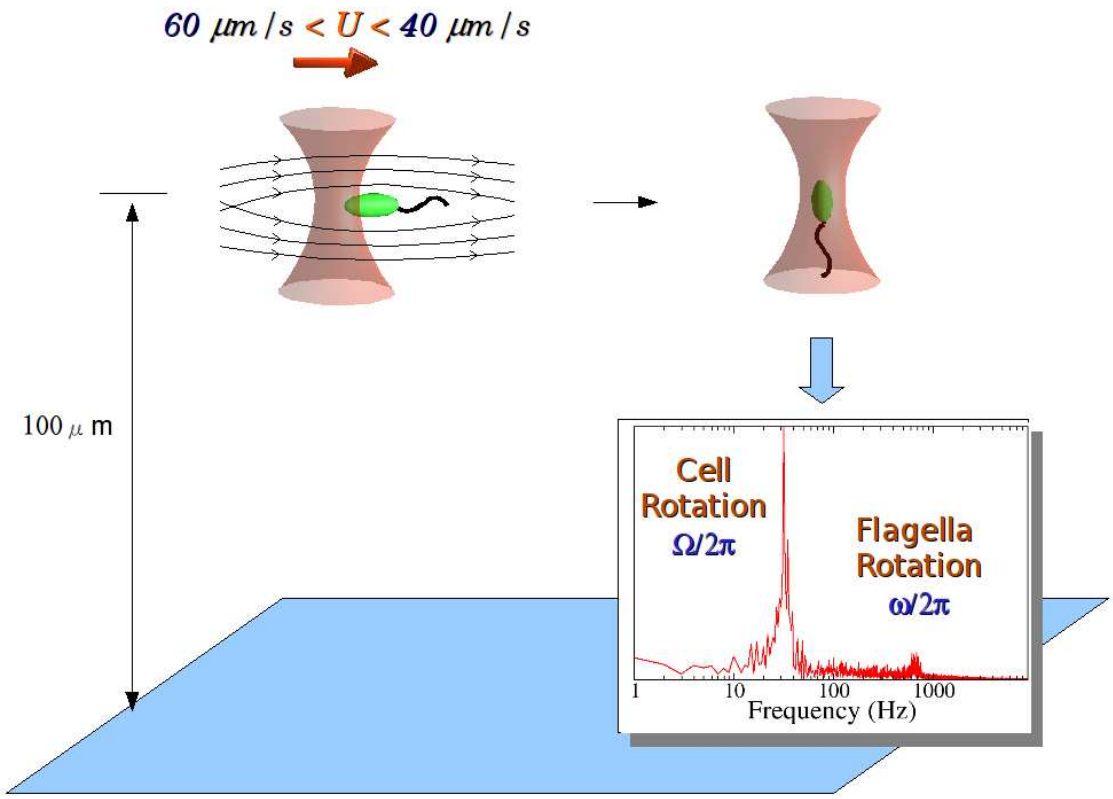

Figure 4.1: Experimental procedure for determining the propulsion matrix for *V. alginolyticus* .

The cells are trapped directly via Configuration C with the aid of an imposed flow, while being in the fluid bulk. The flow speed is then decreased linearly zero, in order to trap the cell temporarily via Configuration B. The flow ramp provides estimates of linear drag *A* and cross coefficient *B* while the stationary state gives a the rotational drag *D* for the flagellum (see main text).

change in the flow speed is performed from $U = -60\,\mu m/s$ to $-40\,\mu m/s$ in $2\,s$. Note that the flow speed has to be larger than the free swimming speed ($U > V$), otherwise the cell would flip into Configuration B (Fig. 4.1). Following the speed ramp, the cell is held with $U = 0$ in Configuration B for $1\,s$. The short trapping time ensures minimal photo damage to the cell. The flow ramp provides values for A and B (from the slope and intercept respectively), while the cell at rest measures D (Eqn. 3.6 with $U = 0$). The probability distribution functions (PDF) for the measured matrix elements are depicted in Fig. 4.2. It is seen that the PDF's can be roughly fitted by log normal distributions, which is along the lines of what has been seen in Fig. 3.5. The average values of the corresponding parameters are given in Table 3.1. The value of the trap constant used was measured to be $k = 1.22 \times 10^{-6} N/m$.

The geometry of flagellar filaments is measured by fluorescent labeling and the complete cellular geometry is summarized in Table 3.2 (See Chapter 7 for details regarding the labelling technique). Table 3.1 further provides, for comparison, corresponding values measured for cells of *E. coli*. Most notable is the the swimming efficiency ε, with *V. alginolyticus* cells having a value much lower than that of *E. coli.* It was predicted by Purcell [45], and demonstrated for cells of *E. coli* (in Chapter 3), that ε is maximized when $A_0 \approx A$. Table 3.1 clearly shows that this condition does not hold for *V. alginolyticus*, which is the possible reason for the lower efficiency. In Fig. 4.3, I plot the variation of the rotation rates of the flagellum ($\omega/2\pi$) and cell body ($\Omega/2\pi$) as a function of the cellular length ($2b$). A longer cell rotates slower in order to balance an amount of torque, while the motor as a whole ($\Omega_M = \Omega + \omega$), however, speeds up slightly, possibly because a larger cell body provides more energy for rotation. The propulsion efficiency (Fig. 4.4), on the other hand, appears to be independent of the cell length, similar to what was observed for *E. coli* in Chapter 3. The flagellar power, which is strongly dependent on the motor speed, shows an increase with cell body length, again indicating that a larger cell pumps more energy to drive the flagellar motor.

The next natural step is to estimate the values of A, B and D with the use of RFT, as was done for cells of *E. coli* in the previous chapter. That is done by substituting the geometry of the cell body and the flagellum (Table 3.1) in Eqn. 5.6. The estimates for A, B and D are depicted by the dotted lines in their corresponding PDFs. To our surprise I observed that the values predicted do not agree with experimental data. Although the values of A and D are close to the predictions by

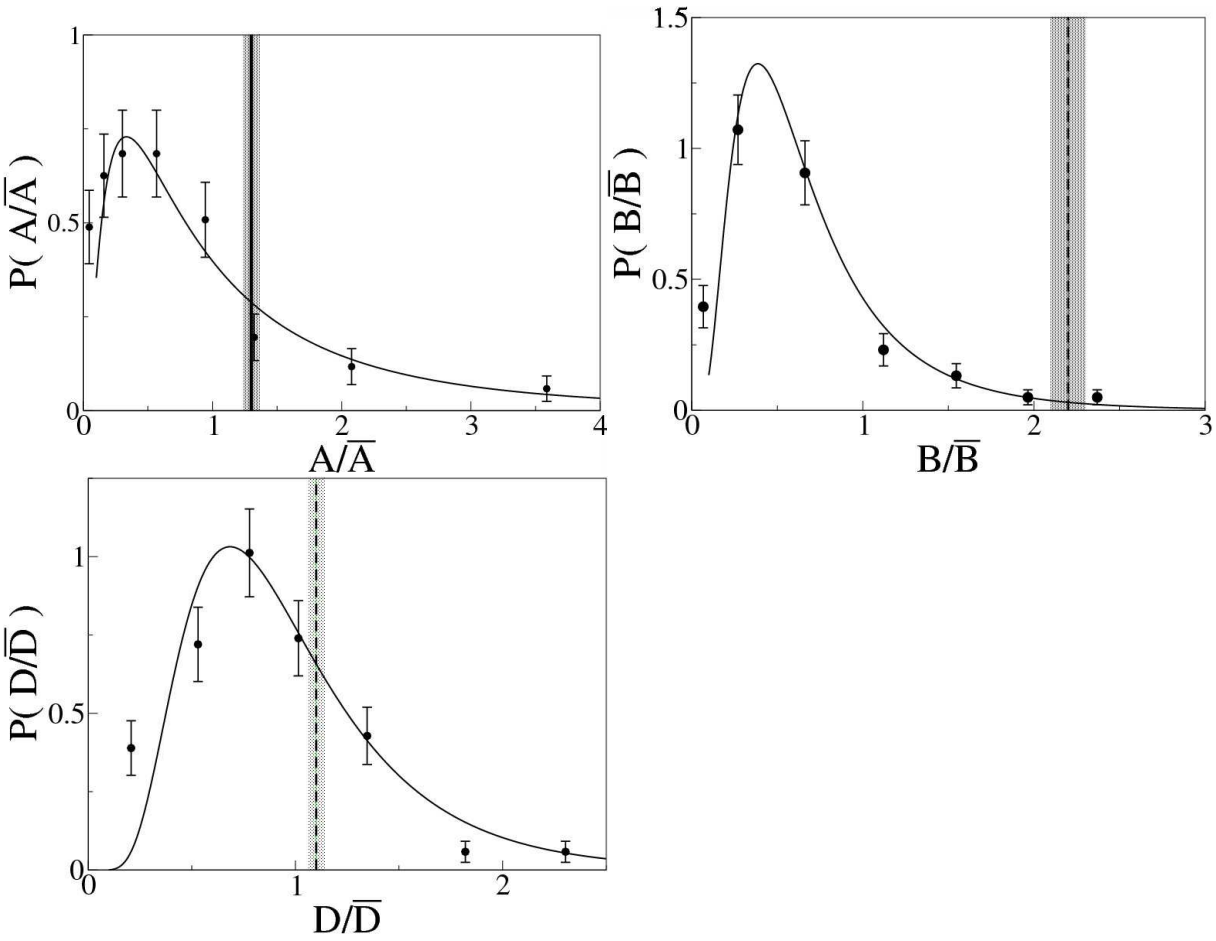

Figure 4.2: PDF for *A*, *B* and *D* for *V. alginolyticus.*

The PDFs for the elements of the propulsion matrix for cells of *V. alginolyticus.* The distributions can all be roughly fitted by log-normal distributions. The corresponding mean values are provided in Table 3.1. The dotted lines denote values of the elements as predicted by RFT, using measured bacterial geometry as given in Table 3.2.

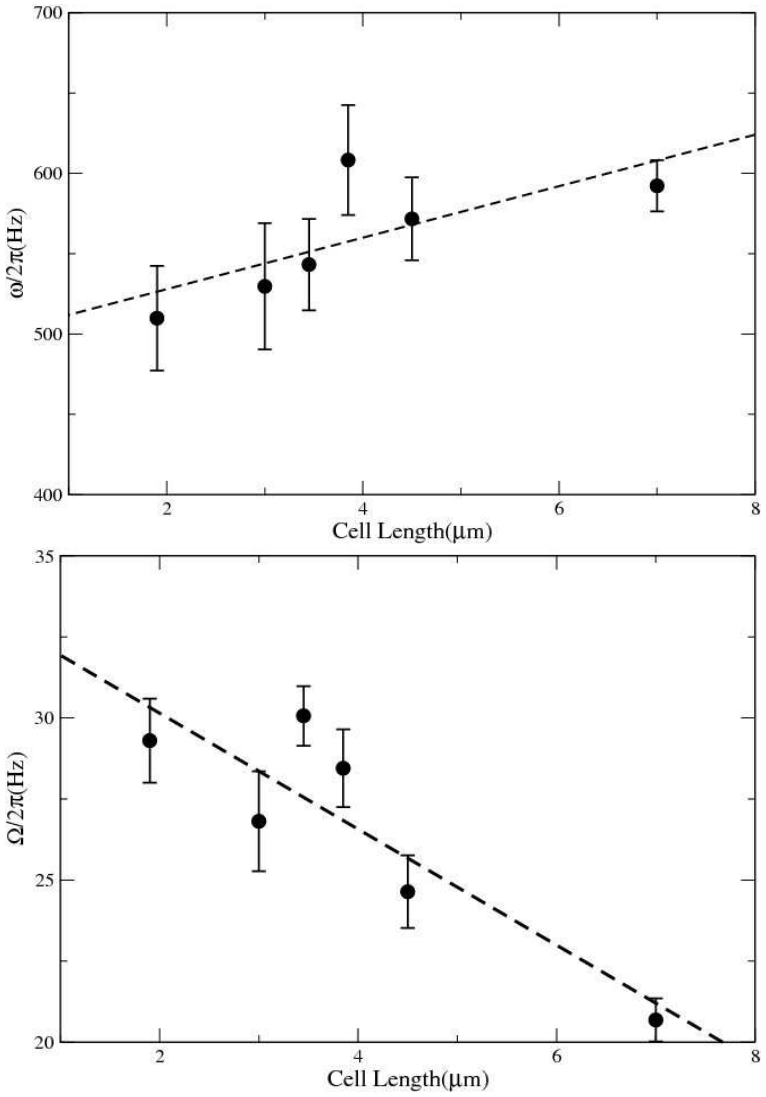

Figure 4.3: ω and Ω variation over cell length for *V. alginolyticus.*

A longer cell body can rotate slower (Ω) to balance the torque produced by the flagellar rotation (ω). A larger cell body provides more power for the motor, making ω to increase with length. The later is a more prominent effect as the increase in ω is more than the decrease in Ω.

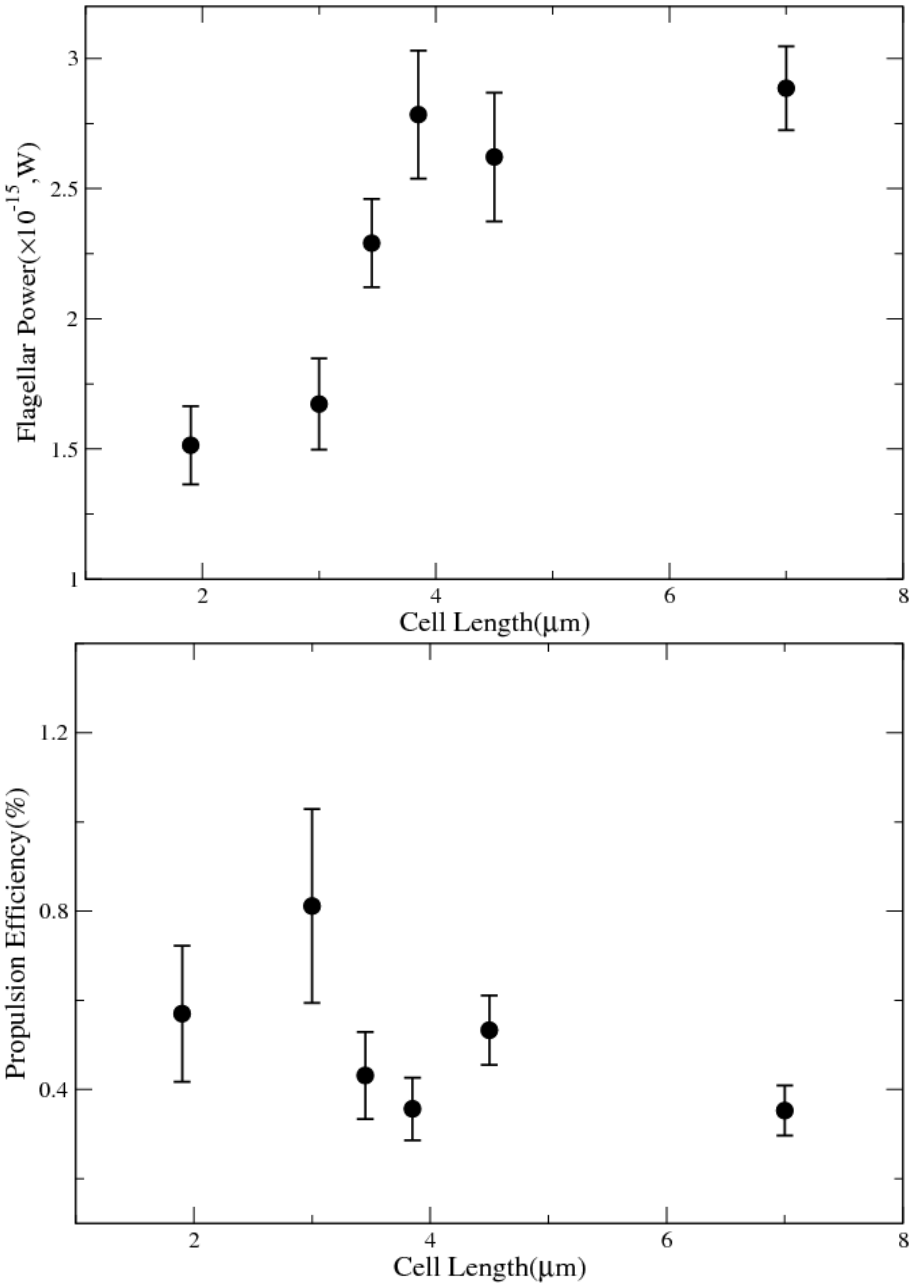

Figure 4.4: Power and efficiency over cell length for *V. alginolyticus.*

The flagellar power is strongly related to the flagellar rotation rate, and hence the output power shows an increase with length. The propulsion efficiency roughly remains constant with cell length, similar to what was observed in Chapter 3.

RFT, B is off by more than a factor of 2.This discrepancy is unexpected, particularly as similar comparisons for *E. coli* had shown reasonable agreements (Fig. 3.5). As pointed out earlier, the technique employed for *E. coli* had sources of possible uncertainties which have been eliminated in this study. Hence, the disagreement with theory for a cleaner system is even more intriguing. As RFT merely considers local hydrodynamic interaction, I was prompted to use a more rigorous theoretical approach, namely one which would include the effects of long range hydrodynamic interactions (LRHI), to explain the experimental observations. This is discussed in the next chapter.

5.0 LONG RANGE HYDRODYNAMIC INTERACTIONS IN BACTERIAL SWIMMING

5.1 INTRODUCTION

Various theories on flagellar hydrodynamics have been proposed over the last several decades. The lack of accurate experimental data has prevented rigorous analysis of these proposed models. In Chapter 3, I use multiply flagellated *E. coli* cells to measure the swimming efficiency, along with their dynamical variables. In doing so I approximated the bundle of *E. coli* as a single effective flagellum. However, for rigorous treatment one has to be able to measure and model flagellar geometry accurately. It is thus evident that *E. coli* is not suited for this purpose, as the dimensions of the flagellar bundle cannot be measured without ambiguities. These shortcomings can be overcome by the use of single flagellated strains such as *V. alginolyticus*, parameters of which can be modeled without uncertainties. Further, all measurements are done in the fluid bulk, eliminating any influence of surfaces.

A smooth swimming mutant of *Vibrio alginolyticus* (YM42), a wild type *Caulobacter crescentus* (YB4038), and minicell producing strain of *E. coli* (P678-54), all possessing single filaments, are used for this study. The data are summarized in Table 5.3 along with their flagellar geometries. Further information, including growth conditions, is detailed in Chapter 7.

5.1.1 Theory of Locomotion at Low Reynolds Number

Bacterial swimming is dictated by the Stokes equation, which along with the boundary conditions of the object under study, specifies the problem [35]. In its most general form one can write the Stoke's equation for a unit volume of the fluid as,

$$\rho\left(\frac{\partial\vec{V}}{\partial t}+\vec{V}\cdot\nabla\vec{V}\right)=-\nabla p+\nabla\cdot\mathbb{T}+\vec{F},$$

where ρ is the fluid density, $\vec{V}$ is the fluid velocity, p is the pressure, $\mathbb{T}$ is the stress tensor, and $\vec{F}$ is any external applied force per volume. The left hand side stands for the forces due to unsteady and convective accelerations respectively. Convective acceleration measures the change of velocity as a function of position (say a fluid forced through a nozzle), while the first term stands for time dependent acceleration. Stoke's equation is usually used along with the continuity equation

$$\frac{\partial\rho}{\partial t}+\nabla\cdot(\rho\vec{\mathbf{V}})=0, \tag{5.1}$$

which is a statement of the conservation of mass. For the special case of an incompressible Newtonian fluid these two equations take the form

$$\rho\left(\frac{\partial\vec{V}}{\partial t}+\vec{V}\cdot\nabla\vec{V}\right)=-\nabla p+\eta\nabla^2\vec{V}+\vec{F}, \tag{5.2}$$

and

$$\nabla\cdot\vec{V}=0,$$

where η stands for the viscosity of the fluid (the contribution of shear viscosity is zero for non compressible Newtonian fluids).

5.1.2 Reynolds Number

The Reynolds number (*Re*) is the ratio of the inertial and viscous forces. It is defined as

$$Re=\frac{VL\rho}{\eta} \tag{5.3}$$

where V, L are typical speed and length scales associated with the motion under consideration. Putting in typical values for bacterial swimming, $V=10\,\mu m/s$, $L=10\,\mu m$, $\rho=10^3\,Kg/m^3$ and $\eta=10^{-3}\,N\cdot s/m^2$, one obtains, $Re=10^{-4}$. Thus, viscosity is overwhelmingly larger than inertial forces allowing us to ignore inertial terms in Stoke's equation (Left hand side of Eqn. 5.2) giving,

$$-\nabla p + \eta \nabla^2 \vec{V} + \vec{F} = 0. \tag{5.4}$$

This used along with the continuity equation (Eqn. 5.1) gives rise to a Laplace equation for the pressure, $\nabla^2 p = -\nabla \cdot \vec{F}$. For a point force along the X axis, placed at the origin ($\vec{F}(\vec{r}) = \vec{F}\delta(\vec{r})$) one gets

$$\nabla^2 p = \nabla \cdot [\vec{F}\delta(\vec{r})]$$

giving,

$$p = -\nabla \cdot \frac{\vec{F}}{4\pi r}$$

as $\nabla^2(\frac{1}{4\pi\vec{r}}) = -\delta(\vec{r})$. For a force along the X axis ($\vec{F} = (F,0,0)$), one obtains [35]

$$p = \frac{Fx}{4\pi r^3}$$

and

$$\vec{u}(\vec{r}) = \frac{F}{8\pi\eta}(\frac{x^2+r^2}{r^3}, \frac{xy}{r^3}, \frac{xz}{r^3}). \tag{5.5}$$

The linear relationship between the applied force and the velocity is a natural consequence of low Reynolds number motion. A well known result of that is the Stokes drag for a sphere translating uniformly at low *Re*,

$$F_{DRAG} = 6\pi\eta R_s U,$$

where R_s is the radius of the sphere.

Table 5.1: Resistance coefficients for RFT.

Model	K_t	K_n
Lighthill [34]	$2\pi\eta/\ln(0.18\lambda/\alpha r)$	$4\pi\eta/(\ln(0.18\lambda/\alpha r)+1/2)$
Gray & Hancock [22]	$2\pi\eta/(\ln(2\lambda/r)-1/2)$	$4\pi\eta/(\ln(2\lambda/r)-1/2)$

The transverse K_t and the longitudinal K_n drag coefficient for a cylindrical element of radius r. λ is the wavelength of the flagellum. These two parametrization schemes are representative of RFT commonly used.

5.1.3 Resistive Force Theory

The linearity of Stoke's equation provides a simplified approach to model bacterial swimming, which was previously termed the "propulsion matrix" formulation (Chapter 3). Along the same lines, an approach to determining propulsion matrix elements (A, B and D for the flagellum) in terms of the geometry, is to assume local resistance coefficients for a small flagellar segment, and integrate over the whole flagellum. This segment has to be smaller in length than the wavelength but should be larger than the radius (r) of the filament. Drag coefficients per unit length K_t and K_n for motions along the tangential and normal directions (See Fig. 5.1) to the axis of the segment can be derived directly from Stoke's equation [35]. Integrating over the length of the flagellum one obtains,

$$\begin{aligned} A &\equiv K_n L(1-\alpha^2)(1+\gamma_k \tfrac{\alpha^2}{1-\alpha^2}), \\ B &\equiv K_n L(\tfrac{\lambda}{2\pi})(1-\alpha^2)(1-\gamma_k), \\ D &\equiv K_n L(\tfrac{\lambda}{2\pi})^2(1-\alpha^2)(1+\gamma_k \tfrac{\alpha^2-1}{\alpha^2}), \end{aligned} \tag{5.6}$$

where ℓ is the length of the coil, λ is the wavelength, and $\alpha = \cos^2\phi$, with ϕ being the pitch angle relative to the swimming axis (see Fig. 1.2). The quantity γ_k is the ratio of the tangential (K_t) to the normal (K_n) viscous resistance coefficients. The helix loses its ability to propel if $\gamma_k \to 1$, $\phi \to 0$ ($\alpha \to 1$), or $\phi \to \frac{\pi}{2}$ ($\lambda \to 0$) as expected. This approach does not include effects of hydrodynamic interactions between parts of filament outside this segment. In other words, it is assumed that the forms of K_t and K_n do not change, due to disturbances in the fluid created by other flagellar segments. A derivation of the expressions for A, B and D has been performed in Appendix A. Different formulations of K_t and K_n have been used in the literature which are summarized in Table 5.1. These differences arise from the usage of various approximations made, which have been discussed in the next subsection.

5.1.3.1 Issues with RFT

RFT has been the traditional choice for the evaluation of the dynamical variables associated with bacteria and other micro-organisms swimming at low Reynolds numbers. There have however,

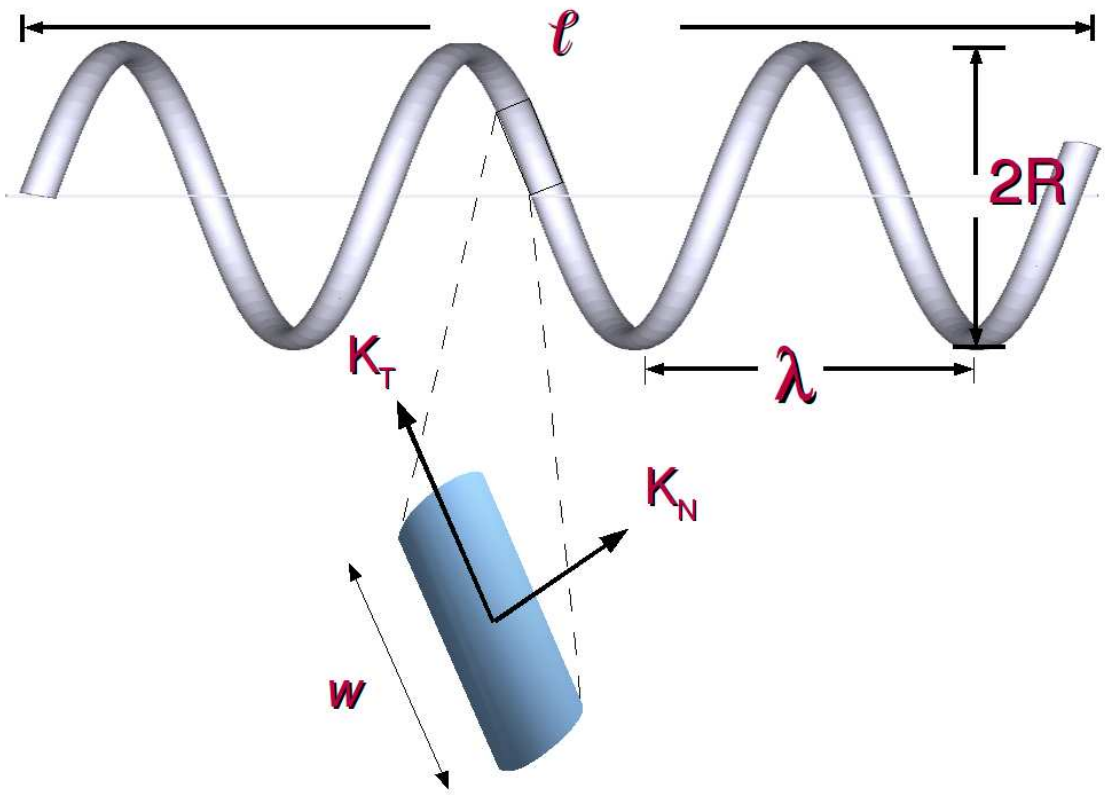

Figure 5.1: RFT formulation.

RFT assumes that a small segment of the flagellum, with length w, has drag coefficients K_t and K_n for the transverse and normal directions respectively. Summing up for all such segments making up the flagellum gives expressions for the propulsion matrix elements (See Appendix A).

been contentions about the theoretical validity of the assigned forms of K_t and K_n (See Table 5.1). RFT applied to swimming micro organisms, was formulated by Gray and Hancock in their classic paper [22], in which these coefficients were derived for the limit of an infinitely thin segment. A rigorous derivation of K_t and K_n from Stoke's equation for a slender cylindrical segment gives [35]

$$K_t = 2\pi\eta/(\ln(2w/r) - 1/2),$$

$$K_n = 4\pi\eta/(\ln(2w/r) + 1/2), \tag{5.7}$$

where w is the length of the segment. The implicit assumption was that $r < w < \lambda$, where r and λ the helix filament radius and wavelength respectively. Gray and Hancock however assumed that (a) the filament is infinitely thin, hence $K_n = 2K_t$ and (b) The width of the small segment is $w = \lambda$. Though these assumptions seemed to fit experimental observations made on sea urchin spermatozoa [22], Lighthill pointed out their shortcomings and suggested alternate forms [34]. He deduced that the $-1/2$ from the denominator of K_t should be dropped, along with using $w = 0.09\lambda$ [34, 35]. Despite these modifications Lighthill stressed on the fact that RFT can only be used in the case when the cell body is absent or is very small. His argument was, that long range interactions can be ignored only when the flagellum produces no additional thrust (i.e. the force which pushes the cell body). Lighthill argued that thrust generation involves co-operativity between flagellar segments, invalidating the assumption that they do not interact. He strongly suggested the use of the more rigorous Slender Body Theory (SBT) for an accurate treatment, which is discussed next.

5.1.4 Slender Body Theory

Slender Body Theory (SBT) is a class of calculations which can approximate the properties of slender objects with the aid of expansions in terms of the slenderness parameter (ratio of the width to the length). SBT was applied to bacterial swimming by Lighthill [34] and others [28]. The basis of Lighthill's approach was to model the flagellum by a distribution of point forces, called Stokeslets, distributed along the flagellar center line. To match no-slip boundary conditions at the flagellar surface, a distribution of dipole velocity potentials, called doublets, were also included. Appendix IV

summarizes the final expressions of Lighthill's SBT, with detailed information available in Refs. [34, 16].

As discussed in Chapter 3, bacterial swimming requires three independent quantities to be described. Lighthill choose dimensionless expressions for swimming speed $v = V/V_w$, torque $t = T/4\pi\eta R^2\omega$ and energy $e = E/\eta V^2$ as those variables. Here $V_w = \omega\lambda/2\pi$ is the phase velocity of the flagellar waves, $T = D_0\Omega$ is the torque on the cell body and $E = T\omega/L$, is the power dissipated per unit length by the flagellum. Lighthill used SBT to derive self consistent expressions for the velocity field created by the flagellum and the cell body. His calculation progressed in three sequential steps, which are as follows.

5.1.4.1 Step 1: Zero Thrust Limit In the zero thrust limit the cell body is absent, such that the flagellum swims by itself. In this limit the flagellum produces no excess thrust and hence the sum of all the Stokeslets along the swimming direction is zero. Calculations of RFT and SBT should provide identical results in this case [34]. Each flagellar segment just balances its own drag, allowing individual parts of the flagellum to be treated independently, which is the basic assumption of RFT. Whenever a load is present it is balanced by the generation of excess thrust, leading to the influence of long range hydrodynamic effects. This is demonstrated in Fig. 5.3 where the calculations of RFT and SBT are found to converge for a vanishingly small cell body. The zero thrust values of v, e and t are shown in Fig. 5.2 using the geometries presented in Table 5.3.

5.1.4.2 Step 2: Non-Zero Thrust Lighthill next estimated v, e and t for the case when a bacterial body is present. The cell body now has to be pushed forward resulting in a net thrust being generated by the flagellum. This reduces the swimming speed from the zero thrust value, with the rotation rate of the flagellum being negligibly effected. It is however assumed, that the flow fields generated by the cell body (flagellum) does not interact with the flagellum (cell body), which would be corrected in the next step. The drag of the ellipsoidal head is approximated by a sphere with effective radius a_E such that $6\pi\eta a_E = 4\pi\eta b/[log(2b/a) - 1/2]$. Figure 5.2 outlines changes in v, e and t as these steps are applied. It is evident from Fig. 5.2 that the reduced torque does not change appreciably. This is because the torque is estimated from forces (Stokeslets and doublets)

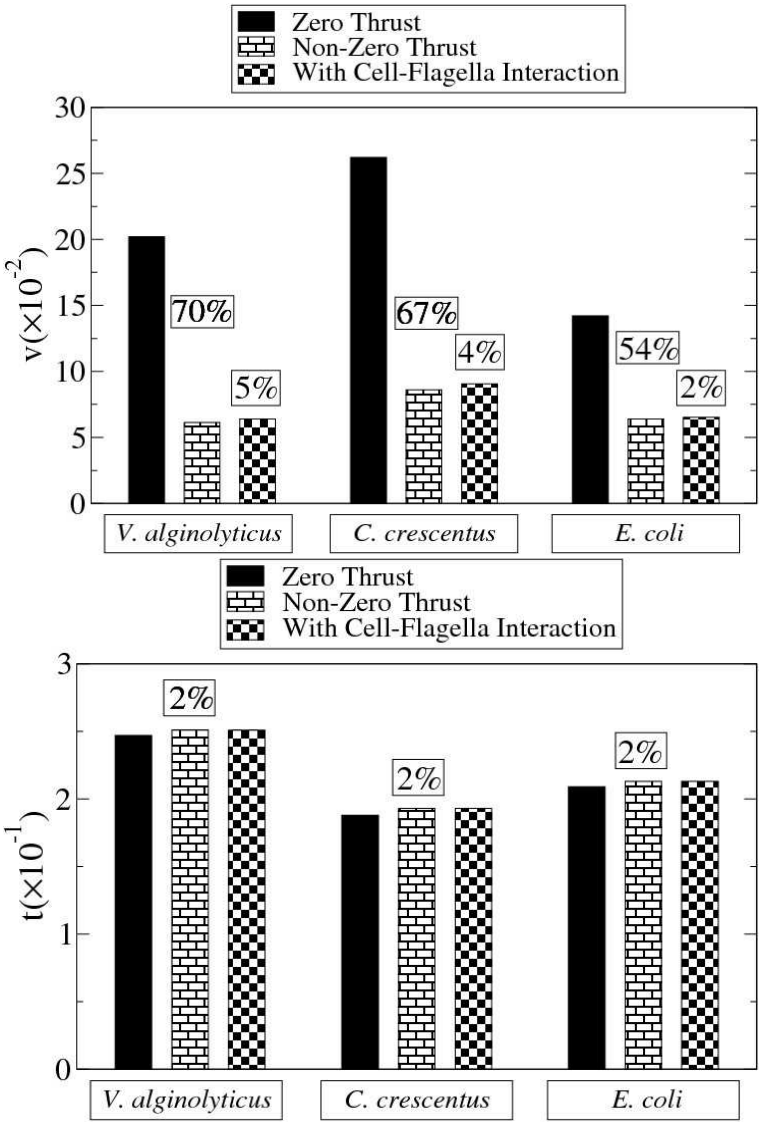

Figure 5.2: Steps in Lighthill's SBT.

Contributions of progressive steps for Lighthill's SBT calculations. Data is provided for the dimensionless speed (v) and torque (t). The zero thrust speed gets reduced by a large factor when the drag of the cell-body is accounted for. The inclusion of cell-body and flagellar flow interactions increases the swimming speed slightly, as the the flow field of the cell has the effect of decreasing the fluid drag on the flagellum.

which are transverse to the swimming direction, thus being unaffected by the presence of a load.

5.1.4.3 Step 3: Cell Body Flagellum Interaction In the next step the interaction of the flow fields of the cell body and the flagellum is considered. The physical picture can be visualized as a combination of the following effects. The flows created by the cell body and the flagellum interact to modify the hydrodynamic drags of one another. As a result, the distribution of Stokeslets along the flagellar length becomes non-uniform. Lighthill wrote down a set of self consistent equations to account for the above mentioned effects. In doing so he was able to estimate how v, e and t change due to the flow field interactions.

For the geometries of the bacterial strains under study, it can be seen that this effect is very small. As shown in Fig. 5.2 changes to both v and t are a few percent when flow field interactions between the cell body and the flagellum are considered. In order to simplify this calculation, it was assumed that the cell body was spherical. The radius of the sphere (a_E) was chosen accordingly to match the linear drag of the actual cell body (which is ellipsoidal). In Appendix C I have estimated the change in the flow field as observed by the flagellum, when an ellipsoid is replaced by a sphere of appropriate radius.

5.2 DYNAMICAL VARIABLES IN RFT

The quantities v, e and t can further be written in terms of the propulsion matrix elements (from Eqn. 3.1 and Section 5.1.4) as follows

$$v = 2\pi B/(A+A_0)\lambda, \tag{5.8}$$

$$t = (D - B^2(A+A_0)^{-1})/4\pi\eta R^2 L, \tag{5.9}$$

$$e = A_T(D(A+A_0)B^{-2} - 1)/\eta L. \tag{5.10}$$

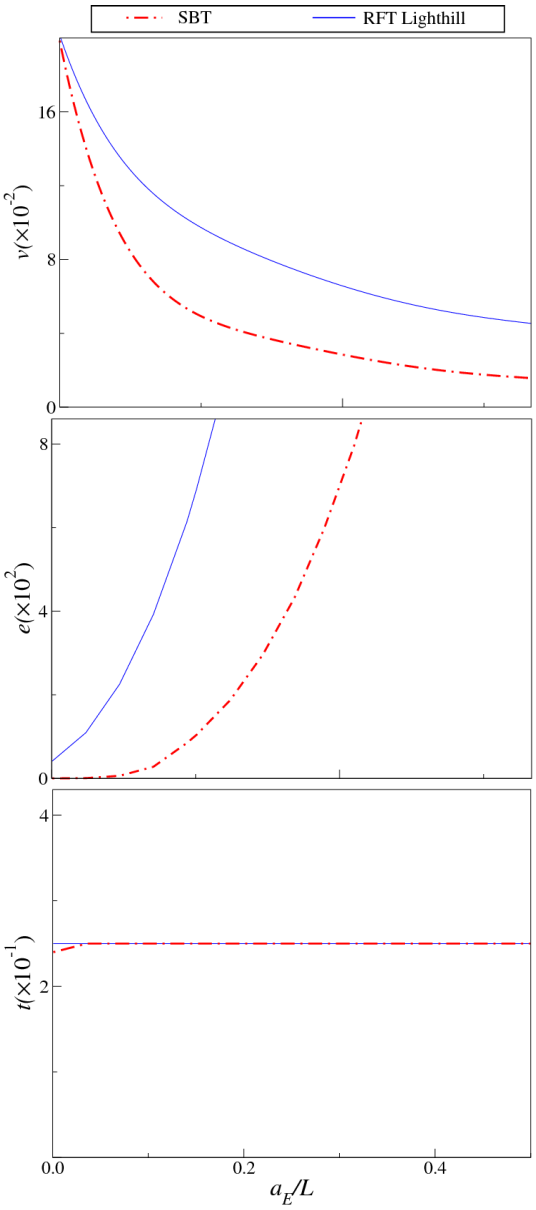

Figure 5.3: Convergence of SBT and RFT.

The calculations for v, e and t as obtained for SBT and RFT. The geometry of *V. alginolyticus* as shown in Table 5.3 is used for the estimations. It can be observed that as the effective radius (a_E) of the cell body decreases, results obtained by RFT and SBT converge. It should be noted, that the t does not change with the load, as transverse forces are not effected by the load imposed by the head.

These expressions are used to estimate v, e and t from RFT in order to compare with the predictions of SBT.

5.2.1 Axial RFT(ARFT).

Although SBT is a more rigorous theory, its formulation is complicated and its application can be daunting. RFT has been very popular over the years for its simplicity. Keeping this in mind, Lighthill proposed a modified RFT which I call the Axial Resistive Force Theory (ARFT). While pointing out that both RFT and SBT give the same estimates for the zero thrust limit, he strongly cautioned against the use of RFT to calculate the dynamics for bacteria with a large cell body. Thus in order to provide estimates for v, e and t for a finite thrust, Lighthill [34] suggested the use of a coefficient (in addition to K_t and K_n), which he called the axial resistance coefficient, K_x. K_x is used to estimate the change of the swimming speed from its zero thrust value V_0, to its finite thrust value V. One still has to use K_t and K_n to calculate V_0 and subsequently use K_x to obtain V. The calculation of torque does not change appreciably from T_0 to T due to reasons discussed previously. Lighthill suggested the following form for K_x,

$$K_x = \frac{2\pi\eta}{\ln(2\varsigma/r)},$$

where $\varsigma = \ell/6$, ℓ being the length of the flagellum. The change in swimming speed $\Delta V = (V - V_0)$ is given by

$$-\Delta V = g/K_x,$$

where $g = A_0 V/L$ is the thrust per unit length produced by the flagellum. Thus, K_x provides the additional thrust required to push the cell body forward when the swimming speed changes from V_0 to V. Using this formulation one can calculate v as

$$v = \frac{V}{V_w},$$

while, t is calculated the same way as the zero thrust case. Summarizing, ARFT can be written in the following form

$$V = \frac{V_0}{(1 + A_0/LK_x)},$$

where $V_0 = B\omega/A$. The torque on the cell body is given by,

$$T = [D - \frac{B^2}{(A+A_0)}]\omega.$$

5.3 EXPERIMENTAL INVESTIGATION OF LRHI.

Having discussed the theoretical approaches that have been put forward, I could now perform direct investigations into which model is best suited for the description of flagellar hydrodynamics. In doing so I wish to understand the importance of LRHI in the swimming of single bacterial cells. The optical trap is used in a way similar to what has been discussed before in Chapter 3. The procedure described earlier (Fig. 4.1) is difficult and time consuming. Bacteria typically swim in random directions while being away from a surface, making it difficult to pursue individual cells and trap them into Configuration C. As a result the collection of large data sets turns out to be an elaborate process. In order to facilitate faster data collection, I adopt a modified technique as depicted in Fig. 5.4. Cells are trapped near the lower surface instead of in the bulk. Due to this individuals can be chased and trapped easily in Configuration B, as they swim in a plane. They are then translated to the fluid bulk using a piezo actuator (see Chapter 7) at a speed close to the average swimming speed ($V_{average}$) for the population. This is done to closely mimic its natural free swimming state. Data acquisition is initiated as the cells move into the fluid bulk ($\sim 20\,\mu m$ from the surface). The power spectrum of the time trace of the cell position in the trap provides the values for ω and Ω. It is observed that the rotation rates do not change with the distance from the surface, indicating negligible influence of surface interactions. In order to measure the free swimming speed V, the cell is transferred to Configuration C (Fig. 5.4) with a quick burst of imposed flow ($U \approx 150\,\mu m/s$). The trapping laser and flow are next switched off simultaneously to let the cell swim away, providing V. This technique allows for the collection of a large number of data sets conveniently. As indicated before, the cell geometry is determined from video images (via bright field microscopy) and flagellar dimensions are obtained by fluorescent labeling. The average geometry of the cells is shown in Table 5.3.

In performing these measurements it is assumed that the rotation rates measured (ω and Ω) for the bacteria while in the trap is unchanged from its free swimming state. This assumption is based

on the observation that rotation rates are negligibly effected by moderate changes imposed flow (equivalently, a change in the swimming speed). This is because the contribution to the flagellar torque by the cross coefficient (B) is small. In other words, the rotation rates are determined by the rotational load experienced by the cell [17, 15] and is negligibly affected by flow rates which are comparable to the swimming speed of the cell.

5.3.1 Results

The procedure mentioned above is repeated for all three bacterial strains. The results are summarized in Table 5.2.

In Fig. 5.5, the reduced quantities (v, e, t) for the three bacterial strains are plotted by dotted horizontal lines with the errors of the mean indicated by the shaded bands. I found that the reduced swimming speed v of YM42 is almost a factor of two smaller than YB4038, despite the small difference in their mean swimming speeds. This suggests that for each rotation of the flagellum, YB4038 swims a longer distance than YM42, indicating *Caulobacter* is a more efficient swimmer. By all measure, the mini cells behave quantitatively similar to *C. crescentus* despite their very different cell geometry (see Table 5.3).

Next we turn our attention to theoretical predictions, which are presented as colored bars in Fig. 5.5. The uncertainties in the calculations, resulting from spreads in the measured geometric parameters, are indicated by the error bars. I found that, while all models predict t to within $\sim 30\%$ of each other and are in reasonable agreement with each strain tested, such consistency is absent for v and e. Specifically, RFT of Lighthill or Gray and Hancock predicted higher v than SBT, and in the case of *V. alginolyticus*, the discrepancy is about a factor of two. This should be compared with the $\sim 15\%$ difference between the measurement and the predictions of SBT. A more conspicuous difference is the reduced power e, resulting largely from its V^2 dependence. As shown, LRHI significantly increases e, and for *V. alginolyticus* the difference between RFT and SBT is a factor of four. The underlying physics that gives rise to this huge difference can be understood as the result of the local velocity field experienced by the flagellum. In RFT, the surrounding fluid is assumed to be static but in the SBT, this field is calculated self consistently, giving rise to an overall rotational movement. This reduces the relative velocity between the flagellum and the

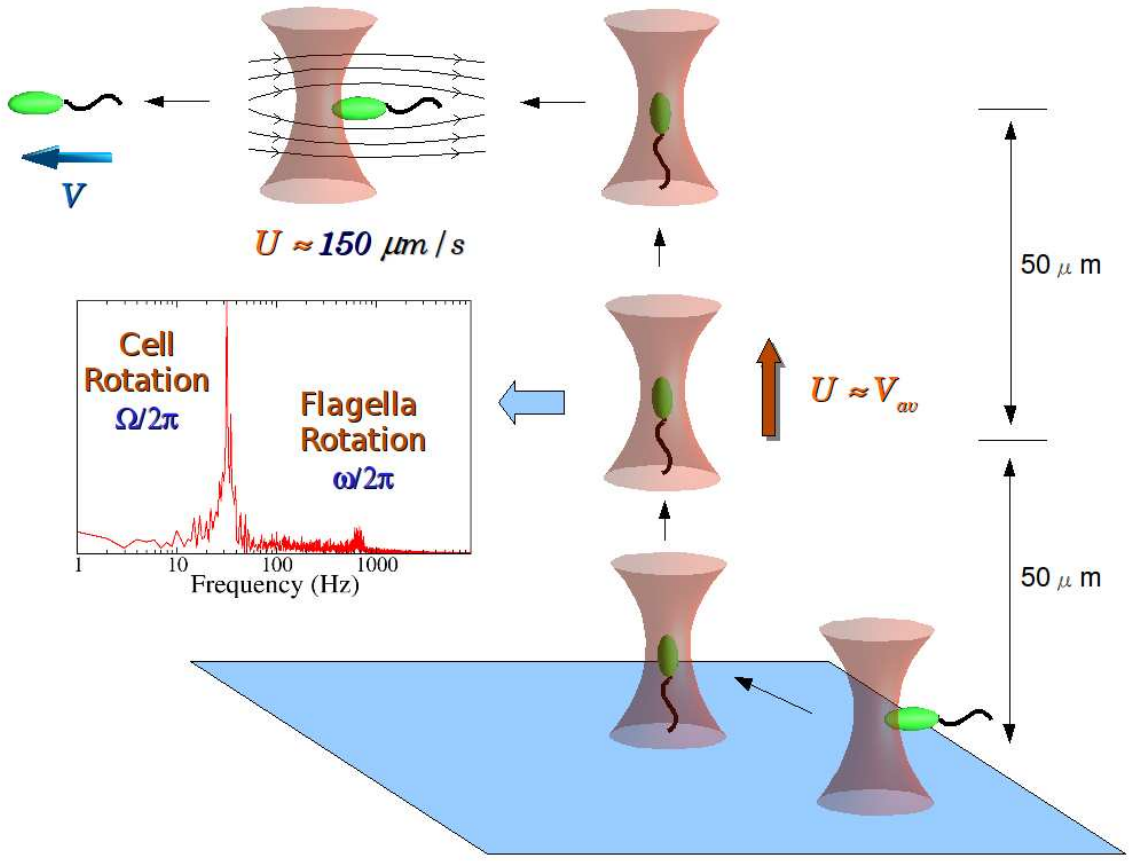

Figure 5.4: Experimental procedure for single flagellated cells.

Cells are initially trapped near a surface in Configuration A. A piezo actuator is used to translate the bacterium in to the fluid bulk via Configuration B, with a speed close to the average free swimming speed of the population (V_{av}). The rotation rates of the flagellum (ω) and the cell body (Ω) are obtained while the cell is being translated. A burst of imposed flow takes the cell into Configuration C, after which the flow and trapping beam are switched off to measure the swimming speed V of individual cells.

Table 5.2: Dynamical parameters for single flagellated cells.

Bacterial Strain		**No. of Cells**	**Dynamic Variables**					
Genus	**Name**	n_D	$V(\frac{\mu m}{s})$	$\frac{\omega}{2\pi}(Hz)$	$\frac{\Omega}{2\pi}(Hz)$	$Torque\,(pN \cdot nm)$	$Energy\,(pW)$	Efficiency(%)
V. alginolyticus	YM42	60	41(2)	550(12)	40(1)	800(30)	2.9(0.2)	0.6(0.02)
C. crescentus	YB4038	80	30(1)	311(10)	31(1)	555(21)	1.3(0.1)	0.9(0.05)
E. coli minicell	P567-48	75	18(0.4)	78(2)	31(1)	420(10)	0.3(0.04)	0.6(0.02)

The uncertainties quoted in parenthesis are standard errors of the mean. n_D is the number of cells used in the measurement of dynamical variables.

Table 5.3: Geometrical parameters for single flagellated cells.

Bacterial Strain		**No. of Cells**	**Flagellar Dimensions**				**Cell Size**				**Fluorescent**
Genus	**Name**	n_G	$\ell(\mu m)$	$\lambda(\mu m)$	$2R(nm)$	$r(nm)$	$a(\mu m)$	$b(\mu m)$	$a_E\,(\mu m)$	a_E/L	**Image**
V. alginolyticus	YM42	40	3.7(1)	1.2(0.02)	280(1)	16	0.35(0.01)	1.3(0.05)	0.57	0.11	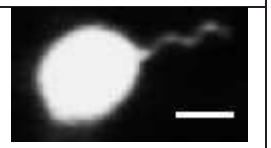
C. crescentus	YB4038	40	4.5(0.6)	0.96(0.01)	280(1)	7	0.42(0.01)	0.96(0.03)	0.50	0.08	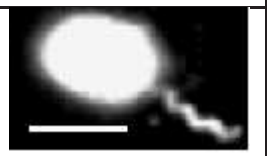
E. coli minicell	P567-48	40	6.2(0.2)	2.3(0.02)	380(5)	12	0.41(0.01)	0.41(0.01)	0.44	0.06	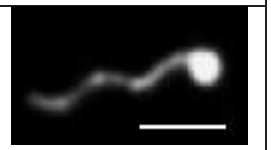

The uncertainties quoted in parenthesis are standard errors of the mean. n_D and n_G are respectively, the numbers of cells used in the dynamic and geometric measurements. The scale bars in the images correspond to $2\,\mu m$.

fluid. Consequently, for the same motor speed, the flagellum will experience a larger slip or a smaller v, and the swimming efficiency e^{-1} correspondingly decreases. As delineated in Fig. 5.5, for all bacteria studied, SBT works considerably better than the RFT, suggesting SBT has captured the essential physics of bacterial swimming. Moreover, this agreement is achieved without a single free parameter in the model.

An interesting feature of Fig. 5.5 is that the discrepancy between RFT and our measurements becomes progressively worse as the bacterial swimming speed increases. For instance, with the mini cells, although the measured v agrees better with SBT (within $\sim 7\%$), the difference with RFT is only $\sim 20\%$. However this difference is $\sim 100\%$ for *V. alginolyticus*, giving the impression that RFT may be a reasonable approximation of slow swimming cells but not for fast ones. This interpretation however is incorrect. According to SBT, the relevant quantity to gauge the importance of LRHI is the load defined as $g = A_0 V/L$ [34], i.e. the thrust/length that a flagellum must provide to propel the cell at velocity V. This is because the net contribution of g, i.e. g integrated along the contour of the flagellum, does not vanish. This is in sharp contrast with the zero-thrust limit where the Stokeslets integrated along the flagellum is zero, significantly reducing the hydrodynamic effect. Since $A_0 \propto a_E$ and V/V_W is constant, it follows that the dimensionless load is given by a_E/L. This point is illustrated in Fig. 5.3, showing RFT and SBT calculations of v, e, and t for a hypothetical bacterium with a variable load a_E/L. The calculation was performed using the flagellar geometry of *V. alginolyticus* and with a_E varying. One observes that for v and e, the difference between RFT (solid line) and SBT (dotted line) decreases with decreasing a_E/L, and the two theories converge as $a_E/L \to 0$, indicating that no LRHI is needed for a zero-thrust swimmer. On the other hand, both theories predict constant t, independent of a_E/L, and the difference between the two theories is negligible. It is thus expected that with everything being equal, bacteria swim slower and need more power in the presence of LRHI. For instance, for a bacterium with a large cell body, say $a_E/L = 0.15$, the reduced speed v without LRHI is about a factor of two higher whereas the reduced energy dissipation e is about a factor of four lower. The observed trend for the three bacteria is consistent with this physical picture. Similar qualitative features were also found by Johnson and Brokaw when they compared the predictions of RFT and SBT for swimming of spermatozoa, which has a load about $1/10$ of *V. alginolyticus* [29].

It has been demonstrated that SBT works considerably better than RFT for all single flagellated

strains tested, and for cells with a heavy load, the use of SBT becomes essential. RFT is commonly used by experimenters to calculate bacterial swimming speed and efficiency. Here I have shown that such practice is only qualitative, and can lead to erroneous results for bacteria with a large body/flagellar length ratio.

5.3.1.1 Controlled Variation of ω

The results obtained in the previous section demonstrated the importance of SBT for the calculation of the dynamics of swimming flagella. This was done for three different bacterial strains with varying geometries and dynamics. It would however be useful, to explore how the theories perform over an extended range of ω, Ω and V, keeping the geometry constant. However, in most biological systems it is difficult to attain accurate control over one particular variable. For instance, in *E. coli* it is difficult to change the motor speed over a big range as it is driven by H^+ ions. A change in H^+ concentration (pH) over viable ranges effects the swimming speed negligibly [27]. I was fortunate to possess a bacterial strain in which a large variation of ω, Ω and V are possible. *V. alginolyticus* is a marine bacterium and its flagellar motor is driven by Na^+ ions. This allows for a controlled variation in the flagellar rotation rate over an extended range ($\omega/2\pi$ changes from 80 to $1050\,Hz$) without effecting the pH. The protocol for achieving this is outlined in Chapter 7. The variation of ω provides a knob, which can be varied to change V and Ω, keeping the average geometry of the cells constant. Although individual cells have different geometries, the average for each bin (a group of ~ 40 cells) remains constant. Theoretical models hence can be checked for consistency over an extended range of dynamical variables. The experimental method is the same as the one described in the previous section. The obtained results are summarized in Table 7.1, with the geometry of the cells being the same as the ones shown for *V. alginolyticus* in Table 5.3.

A notable difference between the dimensions given in Tables 3.2 and 5.3, is the cell length ($b = 2.3\,\mu m$ changes to $1.3\,\mu m$) for *V. alginolyticus*. This is despite the strain type and growth conditions being the same. This is due to a selection of cell lengths inherited in the two distinct measurement procedures. While trapping cells in the fluid bulk via Configuration C, only cells with longer than average cell body sizes are stably trapped for given conditions (flow rate U and trap strength k) and hence increases the measured cell length. Trapping via Configuration B near a surface has no such

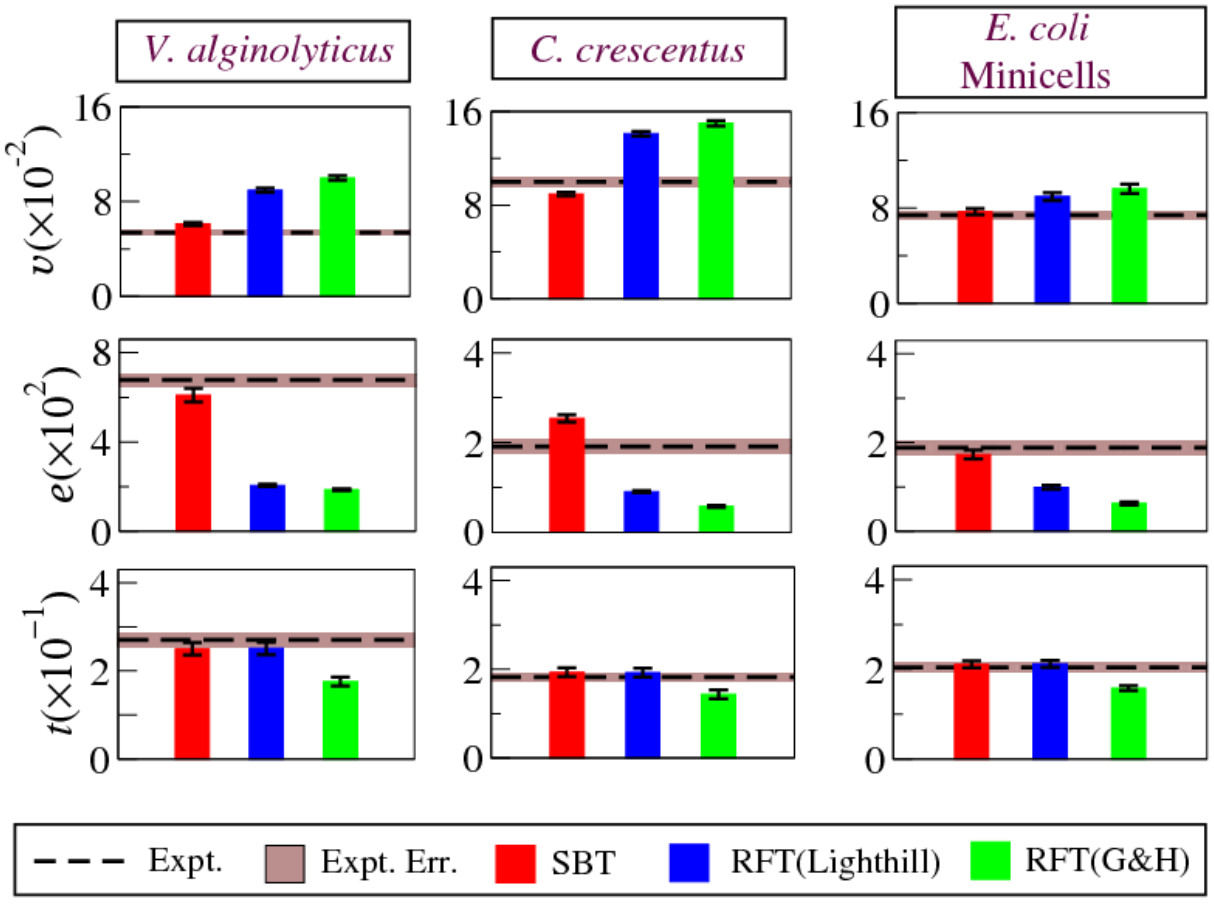

Figure 5.5: SBT, RFT vs. experimental observations for v, e and t.

Comparison of calculations by theoretical models and experimental measurements, for three separate bacterial strains. The dotted line shows experimental values for dimensionless speed v, torque e and energy t. The shaded band stands for experimental error. The geometrical and dynamical variables used are shown in Tables 5.3 and 5.2 respectively. The errors for theoretical predictions are due to uncertainties in measured geometry.

selection, thus providing cell lengths close to the true population average. However, all dynamics and geometry are measured in each case, making the data sets self contained.

Variation of the swimming speed (V) and cell body rotation rate (Ω) with the flagellar rotation rate (ω) is depicted in Fig. 5.6. Linear relations are expected between (V, ω) and (Ω, ω) as bacteria swim at a low Reynold's number ($\sim 10^{-4}$) [45]. This is indeed observed experimentally with $V \propto \omega$ and $\Omega \propto \omega$. Theoretically, the relationship between V, Ω and ω can be written as

$$V = \frac{v\lambda}{2\pi}\omega,$$

$$\Omega = \frac{4\pi\eta t R^2}{D_0}\omega.$$

Values of v and t can be obtained from RFT, SBT (Section 5.1.4) and ARFT, which are then plotted along with the experimental data in Fig. 5.6. It can be seen that both SBT and ARFT work reasonably well for both V and Ω. Deviations from linearity show up for high values of ω which are likely due to deformations in the flagellum. It has been observed previously that λ and R of the *V. alginolyticus* flagellum changes when the motor rotates at high speeds as compared to when it is at rest [52]. According to Takano et. al. [52] λ and R increased by 2% and 1% respectively when $\omega/2\pi$ changed from 0 to $1\,kHz$.

5.3.2 Axial RFT

Lighthill's axial RFT was described in 5.2.1. If ARFT is indeed accurate for the calculation of dynamical variables, it would be of great use to experimentalists because of its ease of use. I hence, have tested ARFT in Fig. 5.7 along with RFT, SBT against experimental observations. It is seen that ARFT performs better than RFT in predicting v, e, and t. Further in Fig. 5.6 I see that ARFT also works satisfactorily over a wide range of dynamical variables.

The results above have shown that ARFT is a suitable replacement for prevalent RFT models, as it retains ease of application and would be of enormous use for evaluation of dynamical variables from geometry. I have in Section 5.2.1 provided a summary of ARFT with readily usable expressions.

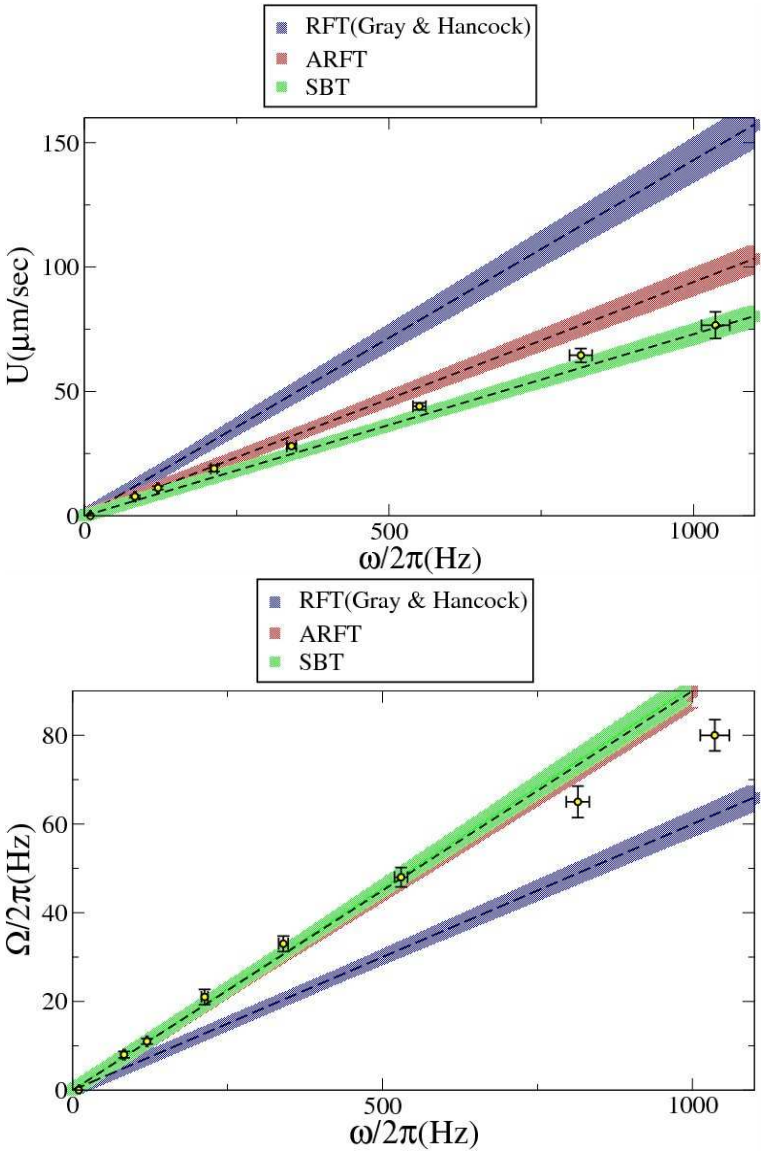

Figure 5.6: Variation of ω for *V. alginolyticus.*

The variation of swimming speed (V) and cell-body rotation rate (Ω) with the flagella rotation rate (ω) for *V. alginolyticus* which are depicted by small circles. Flagella rotation is controlled by changing the *NaCl* concentration in motility medium. In accordance with low Reynold's number hydrodynamics, linear relations are observed between these dynamical variables. Deviations from linearity for high rotation rates are possibly due to deformations in flagellum [51]. The straight lines are due to different theoretical models, as denoted above the plots, with shaded bands showing the uncertainty due to spreads in geometry.

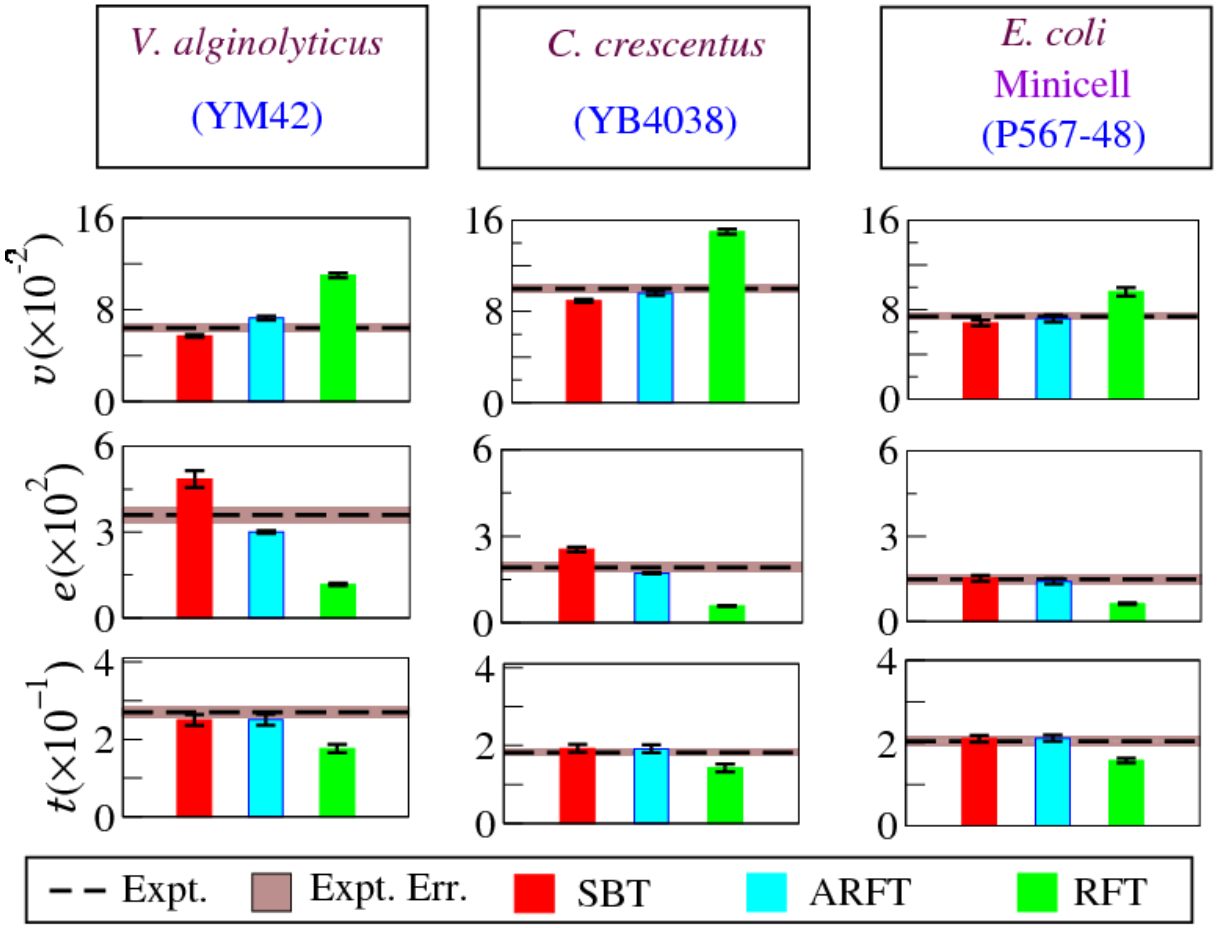

Figure 5.7: SBT, ARFT vs. Experimental Observations for v, e and t.

Figure 5.5 is plotted with the inclusion (exclusion) of ARFT (Gray and Hancock RFT) calculations. ARFT performs better than RFT in predicting experimental observations.

5.3.3 Conclusion

In conclusion, I have performed measurements of bacterial swimming using optical tweezers and compared the measurements with mathematical models of propulsion based on helical-wave propagation along a single polar flagellum. It has been demonstrated that SBT works considerably better than RFT for all strains tested, and for cells with a heavy load, the use of SBT becomes essential. RFT is commonly used by experimenters to calculate bacterial swimming speed and efficiency. Here I have shown that such practice is only qualitative, and can lead to erroneous results for bacteria with a large body/flagellar length ratio. Because of the simplicity in the implementation of RFT, previous theoretical studies [22, 29] have made attempts to reconcile the discrepancy between RFT and SBT by using $K_n/K_t = 2$ and w as an adjustable parameter (see Eqn. 5.7). For instance, the choice of $w = 1$ suggested by Gray and Hancock was purely empirical as this value appeared to fit the experimental data of spermatozoa [22]. Johnson and Brokaw [29] similarly found that an overall increase of K_t and K_n by 35-40% but without a significant change in their ratio could also make RFT to agree with the observations of spermatozoa swimming. If such a phenomenological approach is used for our data, I found that no value of w could produce good fits for v, e and t for any bacterium tested. This is perhaps not surprising as RFT should agree with experiments only at the zero-thrust limit, and prior agreements with experiments [22, 29] have been primarily due to the fact that spermatozoa swam very close to the that limit with $a_E/L \sim 0.02$. The smallest load in our experiment is for minicells, which have $a_E/L \sim 0.06$. I have further demonstrated that a modified RFT, termed the Axial Resistive Force Theory (ARFT) as proposed by Lighthill [34], can be applied effectively for a cell with arbitrary size. This modified theory would be of great convenience for the evaluation of bacterial dynamics in the future.

6.0 CHEMOTAXIS OF *VIBRIO ALGINOLYTICUS.*

In this section I discuss the chemotaxis of *Vibrio alginolyticus*, a marine bacterial strain, and demonstrate a previously unknown strategy adopted for the search of nutrients in open (possibly turbulent) water.

6.1 CHEMOTAXIS

Chemotaxis is the process by which bacteria search for environments rich in chemicals favorable for its growth and survival. This is achieved by a network of sensors on the bacterial cell body, which control the motion of its motors. These sensors (or chemical receptors) detect chemical signals and direct bacterial motility accordingly. Cells have to swim a certain length to determine if there is a chemical gradient and upon the detection of favorable chemicals, the current swimming direction persists. On the other hand, detection of a toxin would make cells reorient to a new direction. Due to their small size and the fact that they live in an environment heavily influenced by thermal motions, bacteria have to perform time averages to improve the signal to noise ratio. The minimum averaging time required is a function of the cell size, the diffusivity of chemicals concerned, and the chemical concentration among other factors. These criteria have been used to estimate limits for the attainable signal to noise ratio [12, 13].

6.1.1 Types of Chemotaxis

Most studies on chemotaxis have been performed on *E. coli* cells. As shown earlier (Fig. 1.1), this bacterium possesses multiple flagella, which form a bundle moving the cell forward (called

"runs"). This is the case when the flagellar motors rotate counter clockwise (when viewed from the cell exterior). On the other hand when rotating clockwise, flagella unbundle and point in different directions, making the cell body to "tumble". Alternating between these two states, a three dimensional random walk results. The decision for either clockwise or counter-clockwise rotation is made based on chemical gradient being sensed. A favorable gradient makes runs more probable while a harmful chemical signal would make cells tumbles more. The chemical network of *E. coli* has been studied in detail and the proteins which mediate signaling between the sensors and the motors are well known. Details on *E. coli*'s chemotaxis can be found in Ref. [2].

The run and tumble mode of chemotaxis is however not applicable for bacterial strains that possess a single flagellum, because when swimming at low Reynold's number a motor reversal merely makes cells backtrack. It was believed that these strains could randomize the swimming direction only by Brownian motion which reorients the cell body [3], a process which is much slower than the tumbly motion of *E. coli*. It has been further observed that swimming of single flagellated cells are asymmetric when near a surface [32]. Cells swim along straight lines while moving forward, but turn in tight circles while moving backward (Fig. 6.1). It needs to be pointed out that this asymmetry would enable these cells to effectively randomize directions when near a surface. This led to speculations that single flagellated strains may have evolved to perform chemotaxis near boundaries [32].

I wish to demonstrate in this chapter that the chemotactic mechanism employed by the single flagellated strain of *V. alginolyticus* is more advanced than what was believed; cells use their flagellum as a rudder to change directions.

6.1.2 Adaptation in Chemotaxis

The chemotactic network has been demonstrated to adapt to chemical concentrations on prolonged exposure [2]. In other words, if cells are exposed to a chemical for a long time ($\sim 5\,min$) they behave the same way as when no chemical is present. This feature allows bacteria to optimize the dynamic range of their sensors, enabling better detection at an elevated background concentration.

Due to this interesting feature, the behavior of cells when no chemical is present or when they have been exposed to a signal for an extended period, is termed the "steady state" of chemotactic

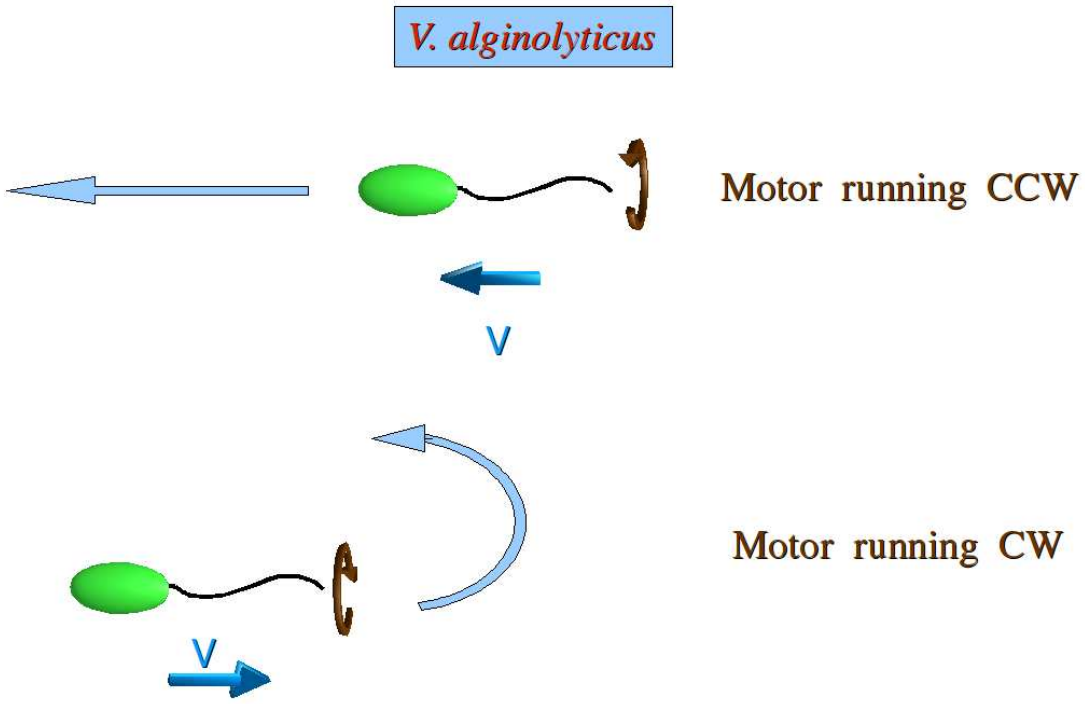

Figure 6.1: *V. alginolyticus* swimming trajectory near surface.

Vibrio alginolyticus cells swim asymmetrically near a surface. The trajectory is viewed from below the surface. The motor running CCW pushes the cell forward while a reversal makes the cell swim in tight circles. It has been speculated, that hydrodynamic interactions with the surface leads to such motion. This asymmetry is not observed in the fluid bulk.

response. In any other situation cellular response would be in transition towards this state.

6.2 THE PHYSICS OF CHEMOTAXIS

Bacteria and other microorganisms have the ability to sense chemicals over extensive thermal noise, which is a hallmark of the environment they live in. This noisy backdrop, provides severe physical limitations on the signal to noise ratio achievable by cells. Back-of-the-envelope calculations to estimate these limits were provided beautifully by Purcell [45] and discussed by Berg [9], some of which I outline below.

Thermal fluctuations have the effect of imparting random torques on the cell body making it rotate, by a process called rotational diffusion. The swimming cell has two degrees of freedom to deviate from the current swimming direction, for which the mean square angular deviation is given by

$$< \theta^2 >= 4D_r t,$$

where D_r is the rotational diffusion coefficient defined as

$$D_r = \frac{k_b T}{D_1},$$

with k_b being the Boltzmann constant, T is the temperature. D_1 is the rotational drag coefficient of the ellipsoidal cell body when it rotates around its short axis, as depicted in Fig. 6.2(b), where the expressions for D_1 also provided [9]. The root mean squared angle is given by

$$\theta = \sqrt{4D_r t} \approx 0.62\sqrt{t},$$

where cellular parameters from Table 5.3 have been used. This implies that in one second, rotational diffusion would reorient the cell by $\sim 17^0$ on average, limiting the precision by which cells can swim in straight lines. This puts an upper bound on the run length used for bacterial swimming, as a long run time would not be useful.

Chemicals being sensed by a cell are constantly spreading due to diffusion. If a cell swims a length that is smaller than the mean displacement due to diffusion in the same time, its chemical sensing would be similar to when the cell is not moving at all. In other words, if the cell does not

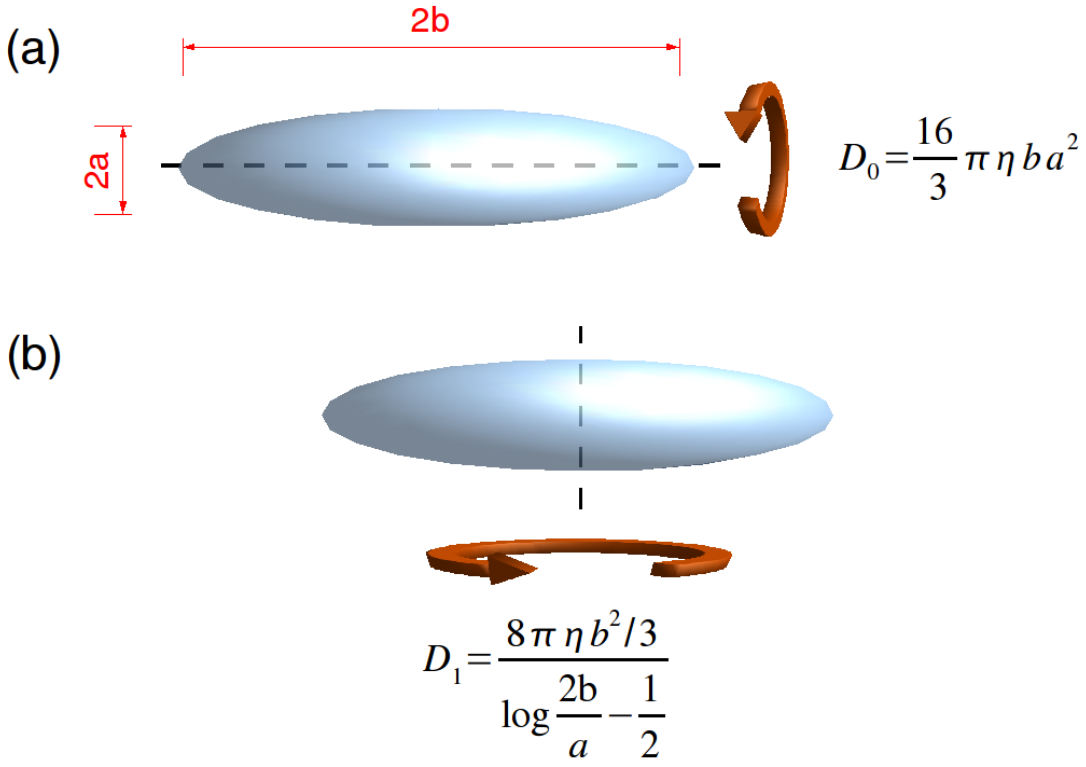

Figure 6.2: Rotational drag for an ellipsoid.

Rotational drag coefficients of an ellipsoid when (a) rotating around its long axis (D_0), and (b) when rotating about it short axis (D_1)

swim longer than this length, there is no use of swimming. Say, the length traversed by a chemical by diffusion (in one dimension along the bacterial swimming direction) is

$$l_1 = \sqrt{2D_\ell t},$$

while in the same time the distance travelled by the swimming cell is

$$l_2 = Vt,$$

where D_ℓ is the diffusion coefficient for the chemical, and V is the swimming speed of the bacterium. Thus, in order to outrun chemical diffusion $l_2 > l_1$ which implies

$$t > \frac{2D_\ell}{V^2}.$$

Taking typical values of $D_\ell = 8 \times 10^{-10}\, m^2/s$ and $V = 40\,\mu m/s$, gives $t > 1\,s$, or $l_2 > 40\,\mu m$, which is similar to typical run lengths observed for bacteria.

Berg and Purcell in their classical work evaluated limits to the precision of the sensory apparatus of microorganisms such as bacteria [12]. They provided an intuitive estimation of the precision that can be obtained by an ideal chemical sensor (which is counting molecules), and showed that the upper bound for fractional accuracy is given by

$$\frac{\delta c}{c} = \frac{1}{\sqrt{D_\ell a_E \bar{c} \tau}}, \tag{6.1}$$

where $\bar{c}$ (D_ℓ) is the mean concentration (diffusion coefficient) of the chemical being sensed, a_E is the radius of the bacterial cell, and τ is the integration time (total time for which the bacterium samples chemical signals). Bialek et. al. [13] improved the above estimate by introducing constraints imparted by the chemical kinetics of the signalling molecules which mediate chemotaxis, and showed that the accuracy for counting the number of molecules that are sensed by the receptor decreases to

$$(\frac{\delta c_{rms}}{\bar{c}})^2 = F(\{k_i\}, \bar{c}, m) + \frac{1}{\pi D_\ell \bar{c} \tau \ell_r}.$$

The second term is essentially Eqn. 6.1, while F depends on a set of kinetic parameters $\{k_i\}$, the number of receptors m, and $\bar{c}$. ℓ_r is the effective size of the receptors or receptor array. The additional noise is due to the internal chemical kinetics of the chemotactic network.

6.3 THE CHEMOTAXIS OF *V. ALGINOLYTICUS*

The chemotaxis of single flagellated bacterial strains has been intriguing, primarily by the question of how they randomize direction for an effective search for nutrients. It has been observed recently that cells of the single flagellated strain, *Pseudoaltermonas haloplanktis* are able to rapidly aggregate along ephemeral nutrient patches [50]. Cells of *V. alginolyticus* are also seen to accumulate around a point source of an attractant fairly quickly (data not shown). How the cells are able to perform an effective search, without the capability of randomizing swimming direction is an interesting question. All the above observations were made in the fluid bulk excluding the possibility of reorientation due to interactions with a surface.

In the absence of an active mechanism for direction randomization, it has been suggested that single flagellated marine bacteria utilize back and forth motion aided by shear flows, to localize into regions rich in nutrients. Simulations showed that the back-and-forth mechanism is more suited than the canonical run-and-tumble mode for turbulent environments, such as oceans. It was suggested that marine cells have to use both motility and shear flows in order to reach and stay in favorable regions [3].

6.4 VISUALIZATION OF CELL RE-ORIENTATION

V. alginolyticus cells swimming in the fluid bulk were studied by video recording via bright field microscopy. To our utter surprise it was observed that the bacteria were indeed able to change directions, sometimes by very large amounts (more than 90^0). Most prior studies have been performed near surfaces, preventing observation of these direction changes as then cells swim asymmetrically, as discussed in the above section and also in Ref. [32].

An intuitively obvious mechanism to explain this would be, that the cells are using their flagellum like a rudder for reorientation. It is hard to speculate any other way which would lead to a large change of direction in the fluid bulk. The quickest way to verify this speculation was a direct observation of reorientation, while the cells are fluorescently labeled, enabling flagellar visualization.

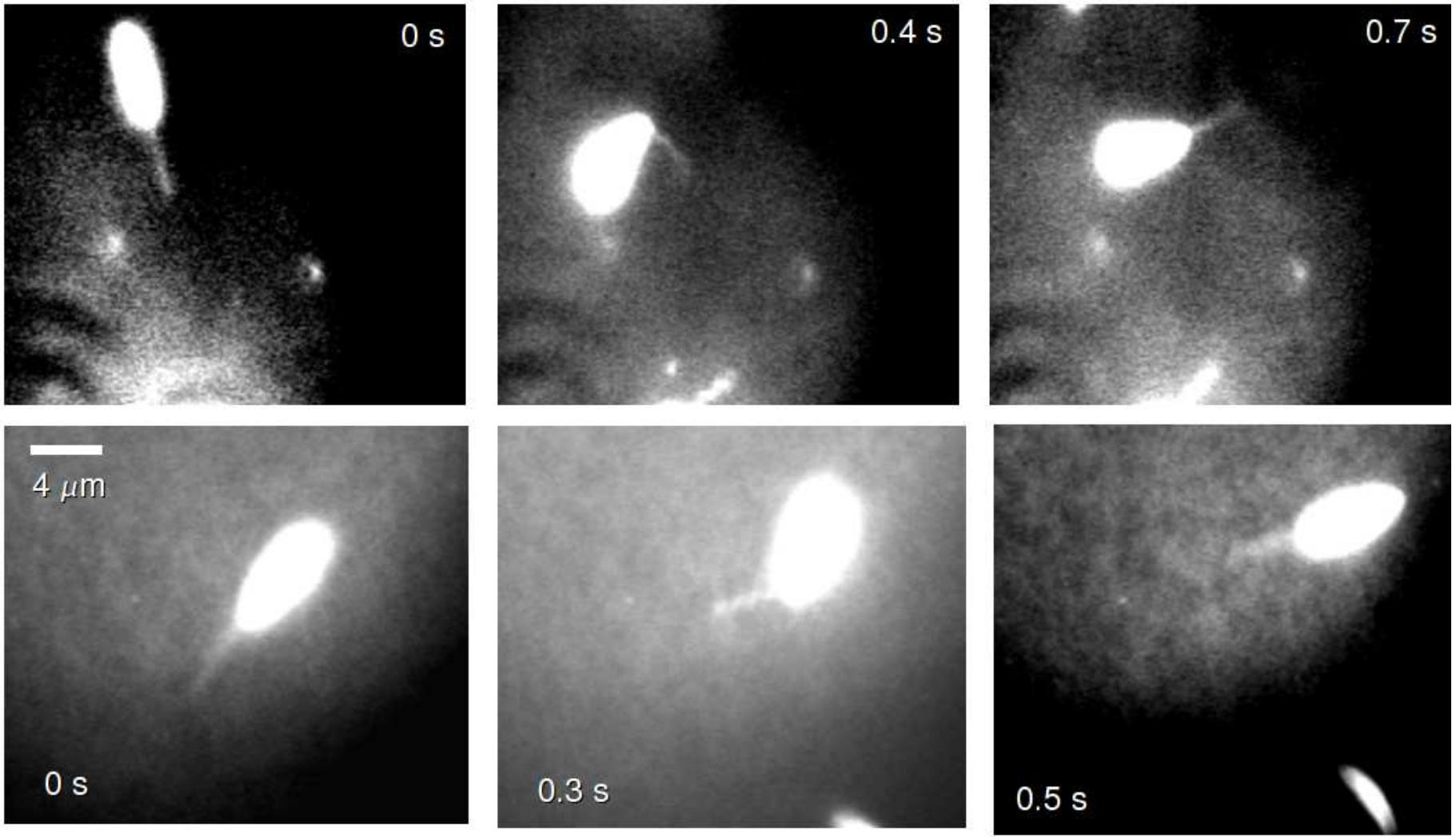

Figure 6.3: Visualization of flagellar bending.

Direct visualization of flagellar flicking. The first row shows a cell which flicks its flagellum and changes directions by around 80^0. The flick shown in the second row is for a smaller angle ($\sim 45^0$), showing clearly that the flagellum stops rotating during the process (2^{nd} frame). It can be seen that the flagellum is blurry, owing to its fast rotation ($\sim 500\,Hz$), before and after the frame. The insets show time progression of the images. Individual images have been adjusted for optimum contrast.

6.5 VISUALIZATION OF FLAGELLAR FLICKING

A direct visualization of "flagellar flicking" would leave no ambiguity about the mechanism involved. This was done by labeling cells with a fluorescent dye and watching them move randomly in the fluid bulk. The cells were exposed to a repellent (see Chapter 7 for details) to increase their rate of flicking, upon which fluorescent flagella were clearly observed to bend sharply making the cells change directions, which is depicted in Fig. 6.4. The following summarizes the observations made.

1. Flicking occurred primarily at the end of motor reversals. In other words, flagella flicked when the cells were at the end of their backward run, moving forward after it.
2. The sequence of events during a flick are outlined in Fig. 6.4. During the flick the flagellum bends slightly, thus producing thrust off the long axis of the cell body, which in turn makes the cell body change orientation.
3. After a brief generation of off-the-axis thrust the motor stops rotating. The flagellum then rotates about a cone to align along the long axis of the cell body, as depicted in Fig. 6.4(d). This straightens the flagellum making it aligned with the cell body. Section 6.9 evaluates the energetics of this process. After realignment the cell moves forward, with the motor resuming its CCW rotation. It is unclear if the protein responsible for the directional change in *V. alginolyticus* is related to the proteins of *Bacillus subtilis* which stops its motor rotation [14].
4. It has been demonstrated in Chapter 5 that Na^+ ion concentration can be changed to modify motor speed, with bacteria functioning normally over a wide range of Na^+ concentrations. This fact is used to probe whether flagellar flicking is mediated by Na^+ ions or if it is coupled with the rotation of the motor, i.e. the flagellum can flick only when the motor is rotating, even though it is not powered by it. The *NaCl* concentration in the motility medium (*HG* medium, detailed in Chapter 7) is decreased to zero to stop cells from swimming. These non motile cells are fluorescently labeled and are treated with a repellent to increase the rate of flickings. No flagellar bending is however observed, indicating that either flagellar flicking is powered by Na^+ ions or the process is somehow coupled with motor rotation, stopping the rotation of which causes flicks to stop.

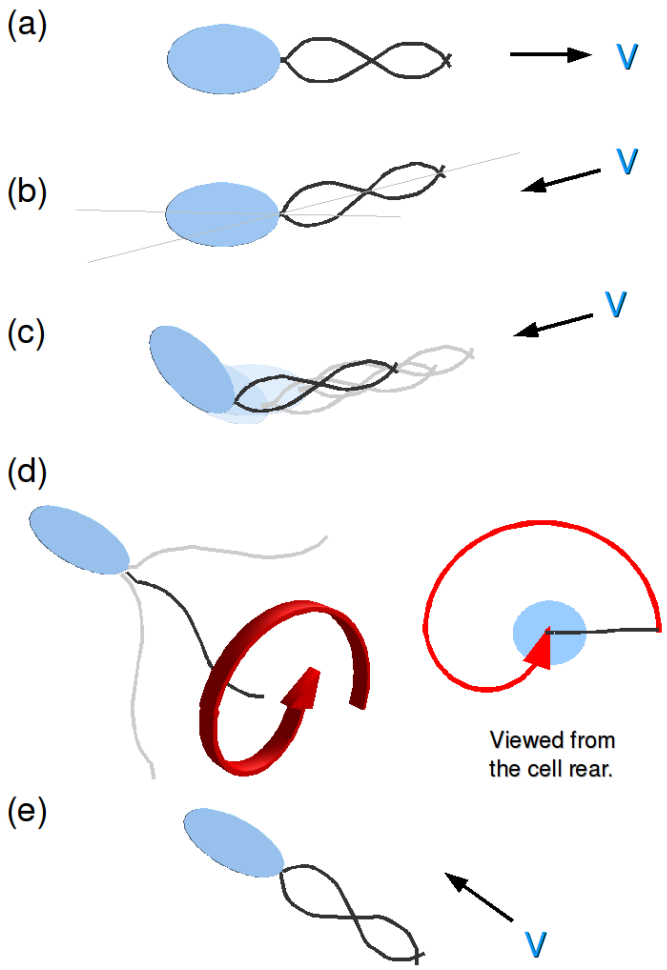

Figure 6.4: Sequence of events for a flagellar flick.

A flagellar flick occurs at the end of a reverse run, when the motor is running CW, and is composed of the following sequence of events. (a) The motors starts to rotate CCW pushing the cell forward. (b) The flagellum bends slightly so that the cell body is no longer coaxial with it. (c) Off-axis thrust force is generated for a short period, which reorients the cell body. In Section 6.9 it is estimated that the motor has to run for $\sim 0.03s$ for the observed average flicking angle. (d) The motor stops rotating and aligns the flagellum with the reoriented cell direction, by a wide sweep as depicted. (e) The motor resumes its CCW rotation to push the cell forward. The whole process takes around $\sim 0.3s$. Section 6.9 contains estimates of the energetics of this sequence.

6.6 VIDEO TRACKING

Bacterial cells are video recorded and their trajectories tracked to obtain information on their steady state behaviour. As it has been shown that flagellar flickings occur at the end of its reverse run, one can identify forward and reverse motions from bright field video microscopy, even though the flagellum is not visible. Data is collected for the forward and the reverse intervals, the flicking angle, and the flicking rate (inverse of the time between two flicks). The PDFs of these quantities are shown in Fig. 6.5. This is done for cells which are not exposed to any chemicals and show their steady state chemotactic response.

All these variables have broad distributions, which is common in many biological systems. The PDF for the forward run times has a very long tail, which may be characteristic of the search strategy of the cells. It has been speculated that infrequent long runs enables bacteria to perform an effective search for nutrients [55]. The average flicking angle is around 80^0, with a broad distribution ensuring direction randomization. In Section 6.9, I will evaluate the energetics of the flicking process to show the feasibility of the suggested mechanism to demonstrate the possibility of the flagellar motor being the source of power for the flagellar flick.

6.7 CHEMOTAXIS STUDIED USING OPTICAL TWEEZERS

Previous chapters have described how an optical trap can be used to measure the dynamics of swimming bacterial cells. An optical tweezers is able to hold bacteria without restricting rotation of the flagellum or cell body (the optical trap applies no torque on the cell body thus not effecting the rotational motion), while the state of rotation can be monitored by a position detector. This provides us with a convenient tool for studying the chemotaxis. Trapped cells can be forced to move away from or towards a nutrient source, with continuous monitoring of the motor response. This is not possible with free swimming cells as they move at will, making such a study difficult.

The basic procedure for this analysis has been summarized in Fig. 6.10. Cells are held via Configuration C (Fig. 2.3) and manipulated to observe their responses. To probe the steady state behavior, cells are trapped and motor rotations recorded for $4s$. As described in Chapter 3 the

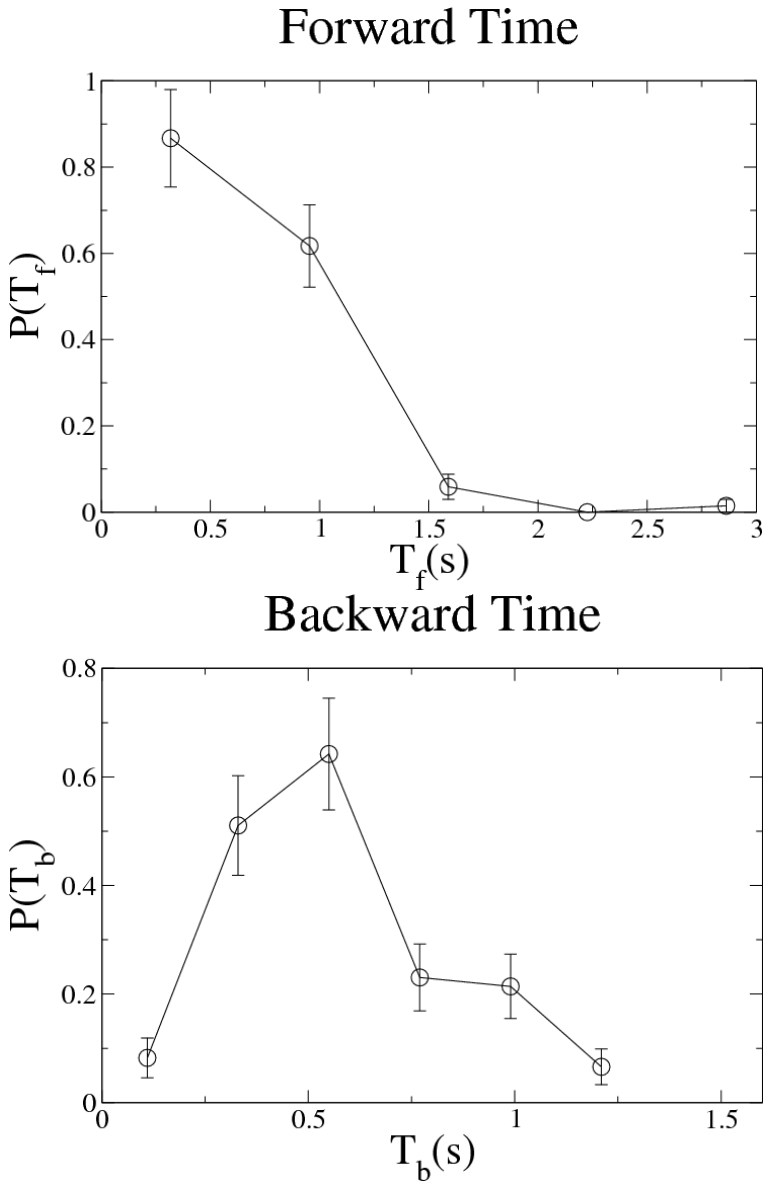

Figure 6.5: PDF of forward and reverse run times.

PDF of the forward and reverse run times of *V. alginolyticus* cells, as analyzed by bright field microscopy. The average times are $\bar{T_f} \sim (0.7 \pm 0.05)\,s$ and $\bar{T_b} \sim (0.6 \pm 0.02)\,s$ for 100 cells.

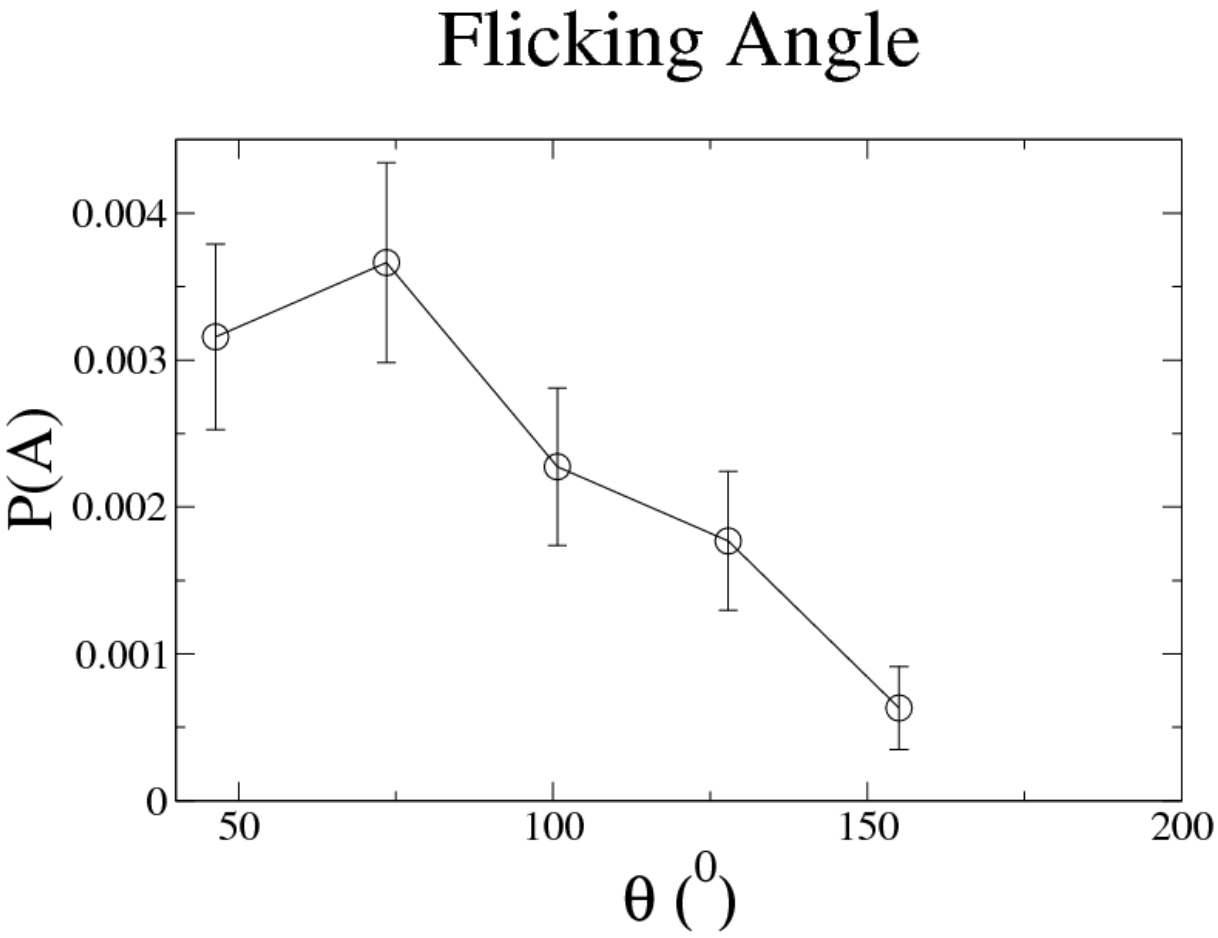

Figure 6.6: PDF of flicking angle.

PDF of flicking angles of *V. alginolyticus* cells in steady state. The average angle is $\bar{A} \sim (76 \pm 3.6)^{0}$ for 100 cells. For typical run times rotational diffusion has an average reorientation of $\sim 30^{0}$, letting us ignore smaller angles.

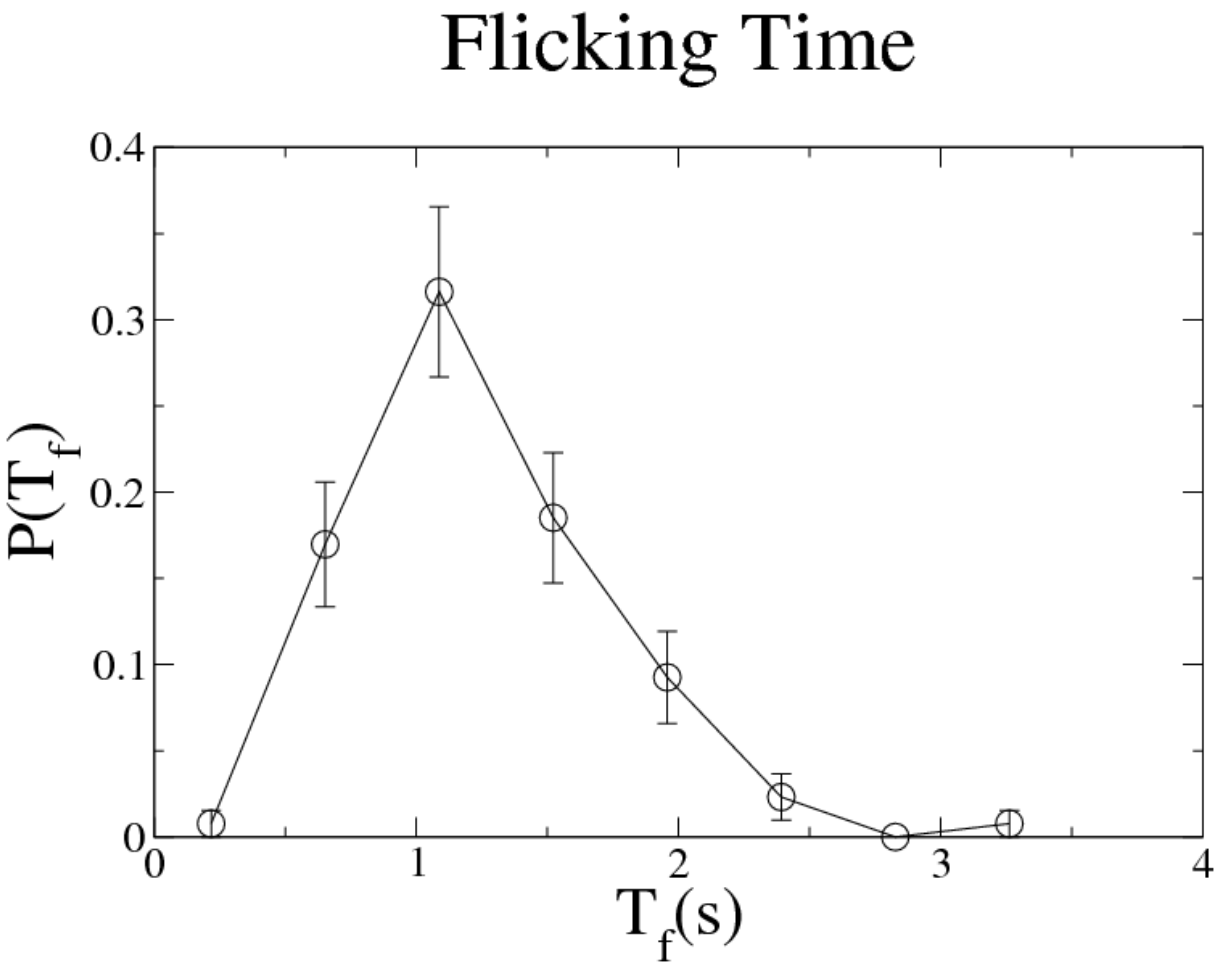

Figure 6.7: PDF of flicking time.

PDF of average time between two flicks for cells in the steady state. The average time is $\bar{T_f} \sim (1.3 \pm 0.05)\,s$ for 100 cells.

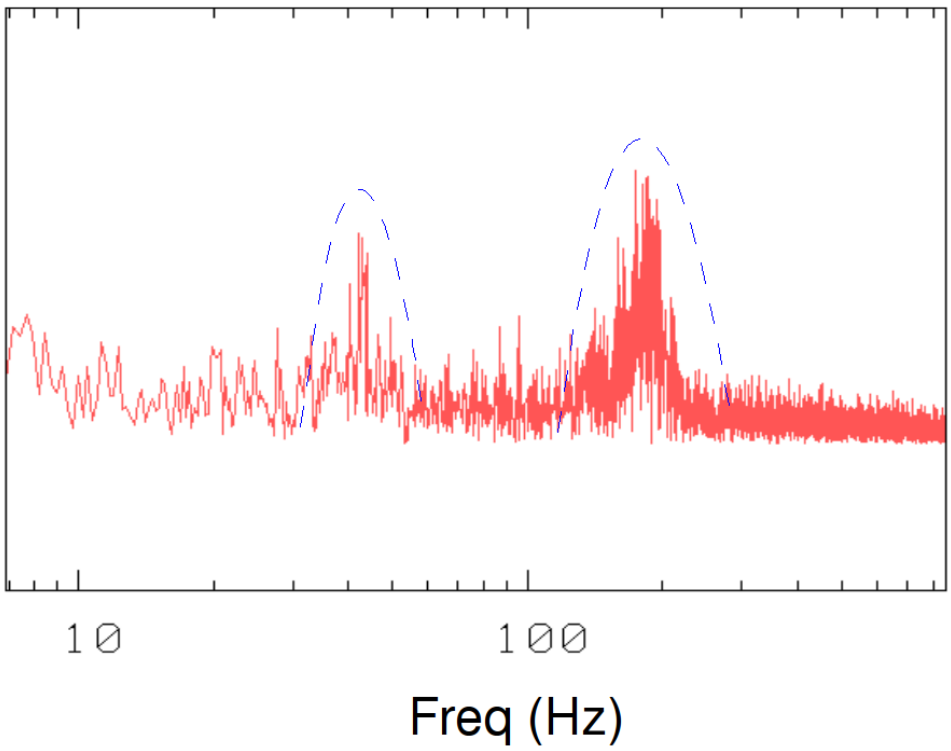

Figure 6.8: Band pass filtering.

Window functions are multiplied to the Fourier transforms, individually centered according to the measured cell body ($\Omega/2\pi$) and flagellar rotation ($\omega/2\pi$) rates to filter out respective trajectories. Everything outside the window is set to zero, while the smooth edges ensure that the inverse transform is free of unwanted artifacts. The result obtained are shown in Fig. 6.9.

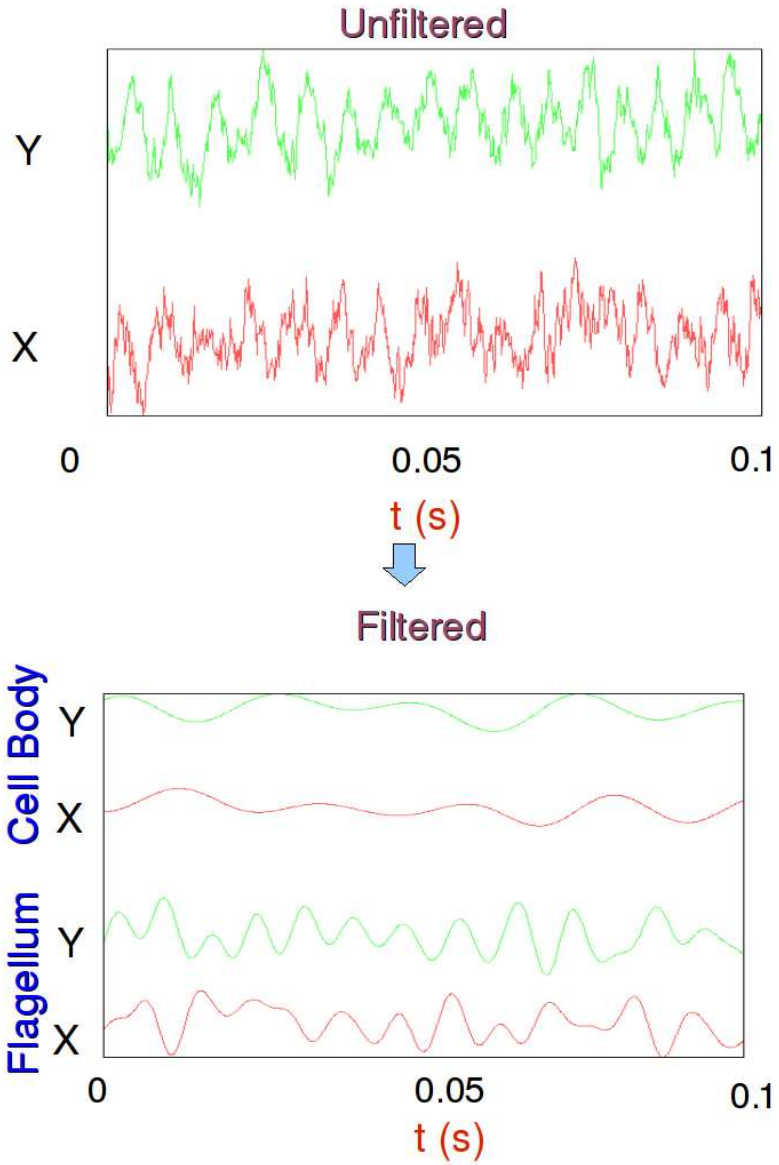

Figure 6.9: Filtered trajectories.

Data filtered in the frequency space as depicted in Fig. 6.8, is transformed back into real space to separate out trajectories of the cell body and the flagellum. The cell body rotates slower and in the opposite direction as compared to the flagellum.

power spectrum has peaks corresponding to the flagellar ($\omega/2\pi$) and cellular rotation ($\Omega/2\pi$) frequencies. Knowledge of these frequencies enables bandpass filtering of the time trace of the cell body fluctuations in the trap (Fig. 6.8), providing separate trajectories for the cell body and flagellum, as depicted in Fig. 6.9. These individual trajectories enables us to monitor the direction of rotation of the flagellar motor and study how they change in response to chemical gradients.

Unfortunately, it was not possible to observe flagellar flicks via the optical trap. The flicking energy is not high enough to leave a noticeable difference in the signal over motor rotation (see Section 6.9) and thermal noise. A sample of the steady state response is shown in Fig. 6.11. The PDFs for the run times collected for a number of cells is shown in Fig. 6.13. As cells can be trapped either with the flagellum up or down, it was not possible to distinguish forward and reverse rotations. Hence, the obtained PDF is an average of forward and reverse motions. Some bacteria were observed to switch rotation directions at most once or never in the $4s$ observation window, for which only a lower limit could be provided for the run times. The PDF shows a long tail which is in agreement with the observations of Figs. 6.5.

6.7.1 Chemotactic Response to Chemical Gradients

Using an approach very similar to that described in the previous section, I now look at the response of cells to a positive or negative gradient in order to explore the chemotactic strategy adopted by these cells. Cells were trapped via Configuration C and moved towards or away from a point source of nutrient (see Section 7) which sets up a gradient by diffusion, as depicted in Fig. 6.10. A sample response of the flagellar motor is depicted in Fig. 6.11. It is clearly seen that while the motor switches back and forth when taken down the gradient, it is completely smooth when moved towards the point source. The PDFs for the observed switching times T_{DG}, is shown in Fig. 6.14. When down the gradient T_{DG} has a broad distribution, which is symmetric and shows a characteristic switching time scale ($\sim 0.5s$). A positive gradient makes cells swim smoothly with a very few showing a single switch in the $4s$ observation window. Switching times are thus not defined for these cells for which switching rates can only be calculated by a lower limit $\sim 1/4s$. These rates are summarized in Fig. 6.12.

It is interesting to compare the PDFs for the switching times while in the steady state (Fig.

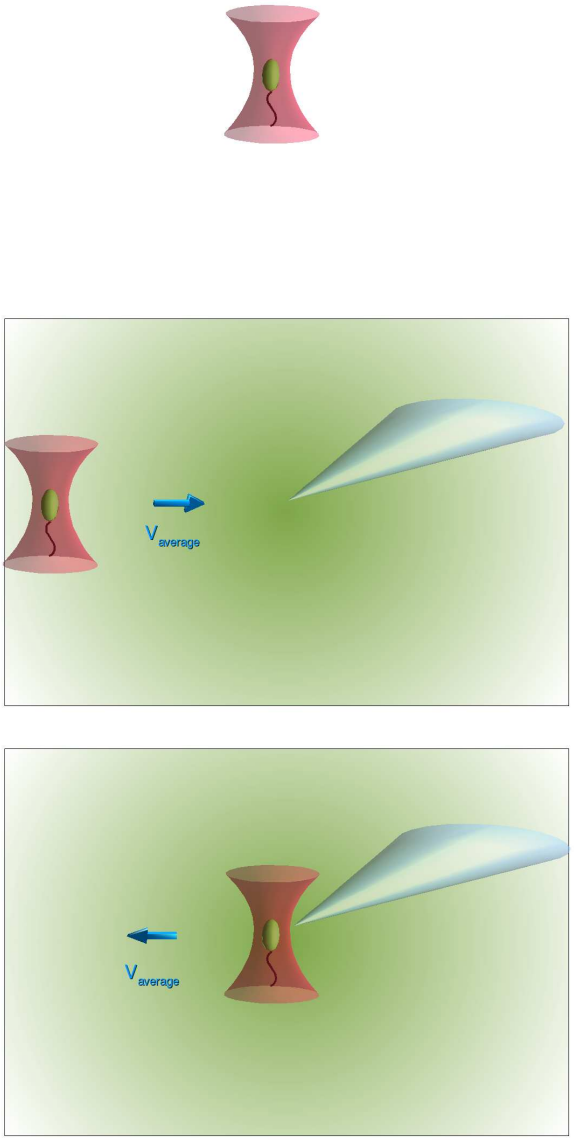

Figure 6.10: Probing chemotactic response with an optical tweezers.

The setup for the detection of cellular response by an optical tweezers. Cells are held in the absence of any chemical to probe their steady state response. A micropipette is used to set up a chemical gradient, and cells are then trapped and maneuvered towards or away from it, to simulate exposure to an increasing or decreasing gradient. The speed of translation is kept close to the average swimming speed of the population to closely mimic its free swimming state.

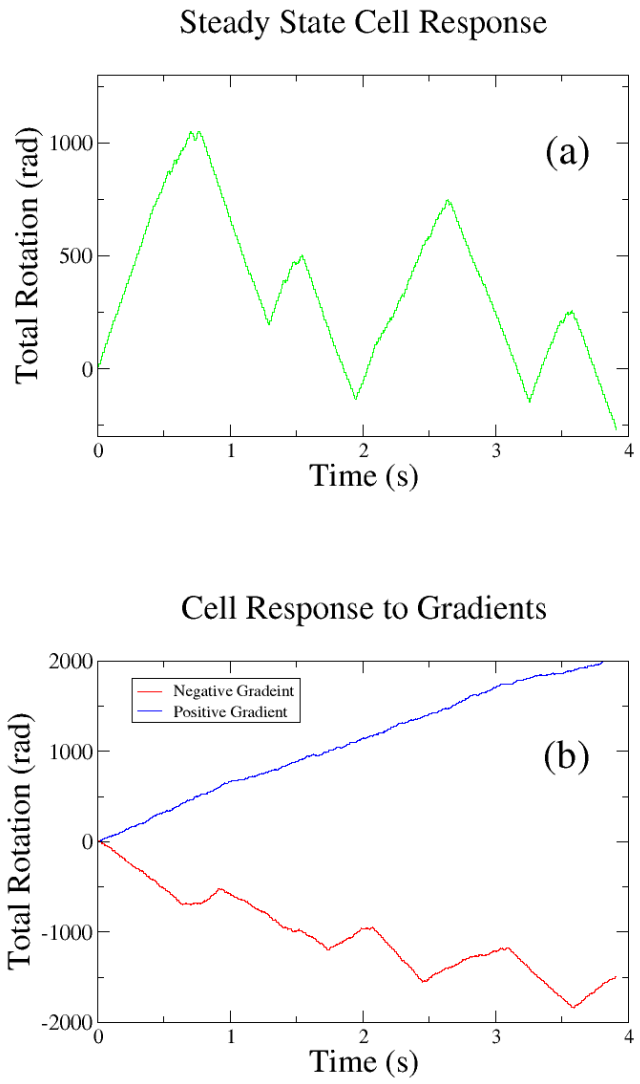

Figure 6.11: Cellular response data.

Time trace of the position of the bacterial cell body is bandpass filtered to obtain the rotational motion of the cell body and the flagellum (see Fig. 6.9). The plots show the cumulative angle traced by the rotation of the flagellum. (a) The steady-state response shows the motor changing rotation directions. (b) Cellular response to increasing and decreasing gradients shown are for the same bacterial cell. The flagellum does not change directions while moving up a gradient while frequent switches are observed while moving down one.

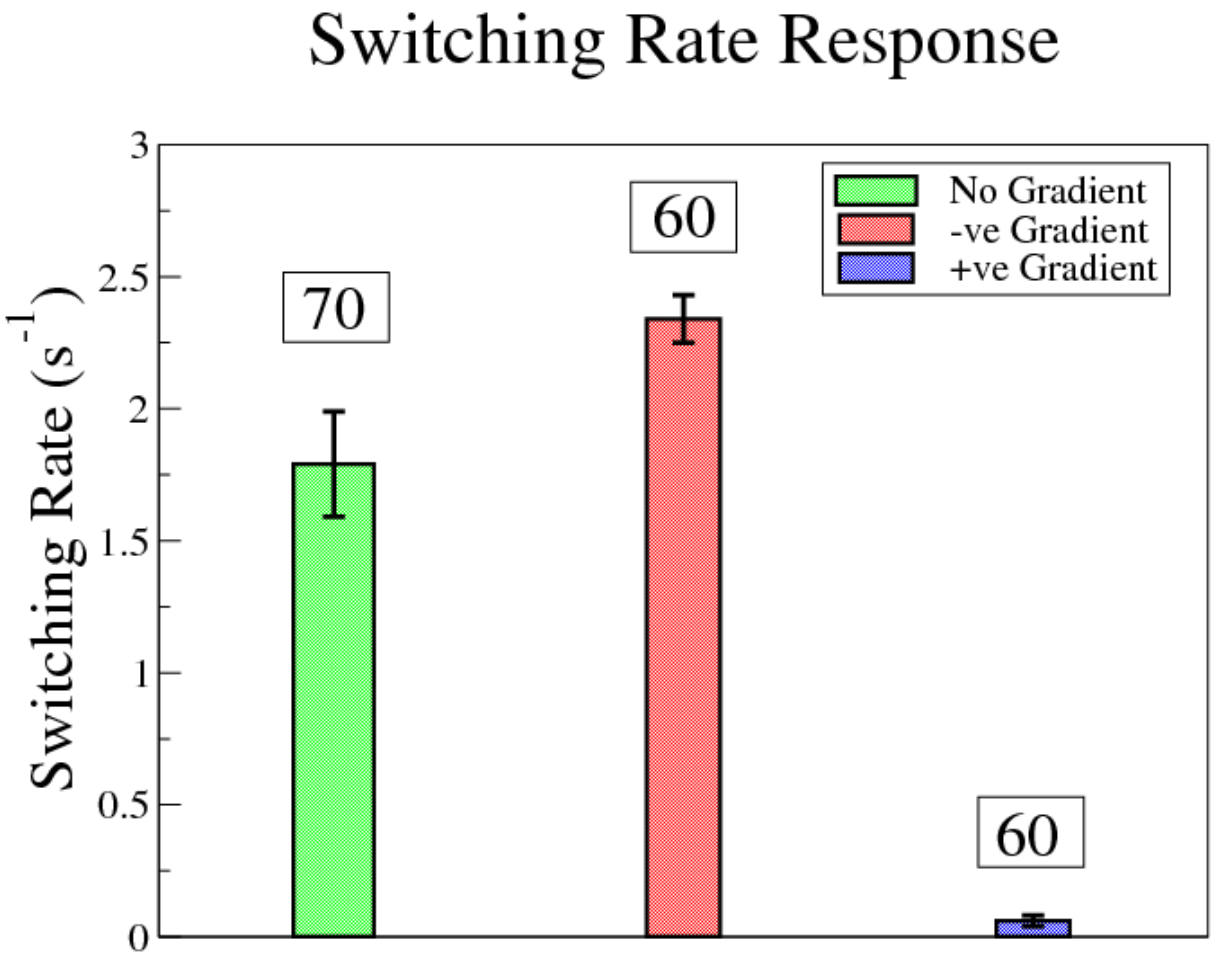

Figure 6.12: Switching rate response to gradients.

Comparison of flagellar switching rates along with the corresponding number of data in each case. The steady state has fewer switches with a bigger spread, while ones moving towards a higher concentration rarely switch. Cells being moved down a gradient have more frequent switches with a smaller spread, which indicates their tendency to reverse swimming direction.

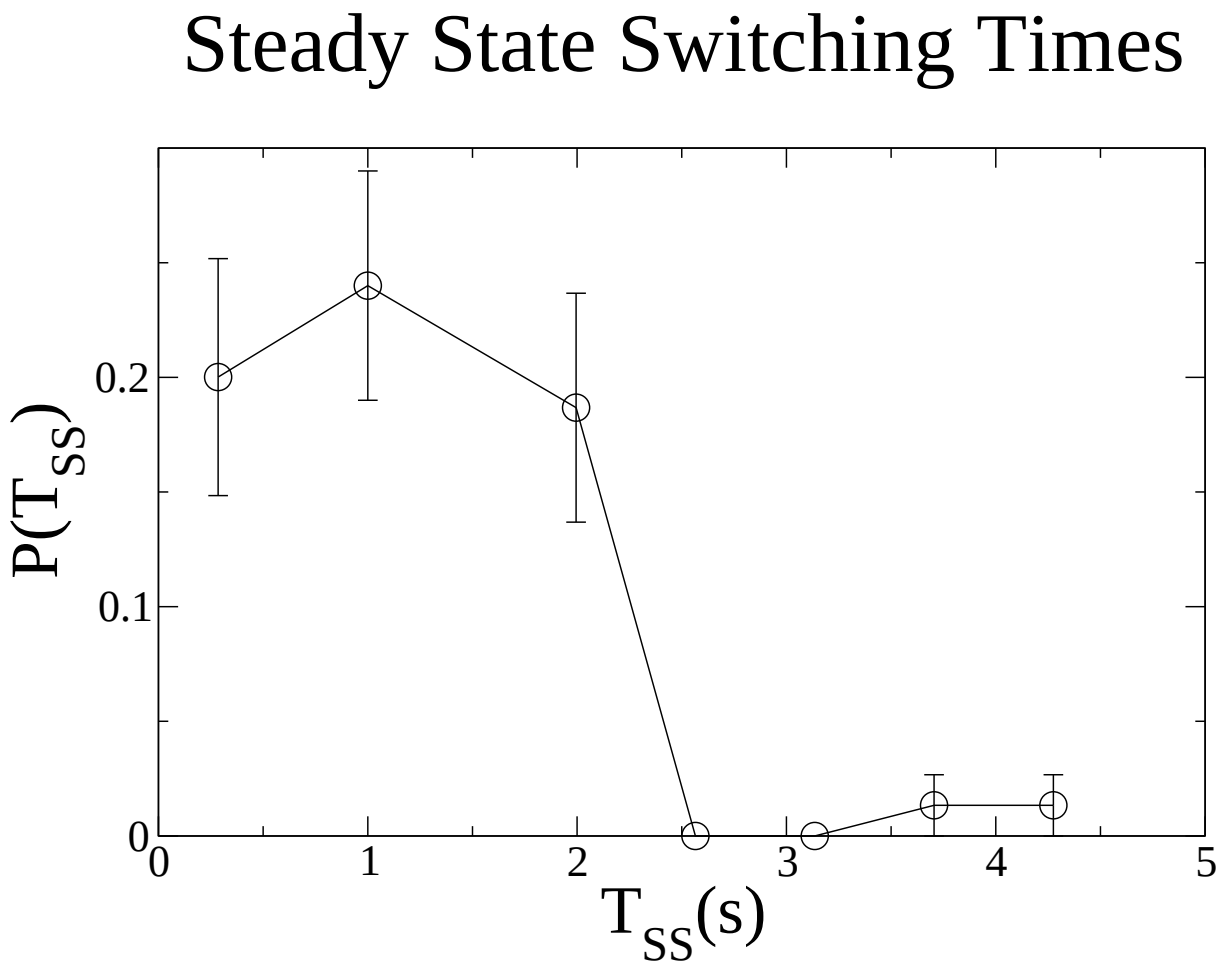

Figure 6.13: Steady state switching times in optical trap.

Steady state switching times as obtained from optical trap data. Cells can be trapped symmetrically with the flagellum pointing either up or down. The switching times obtained are thus the average of forward and reverse times. Some cells are observed to switch only once or never in the observation window of $4s$. Only lower bounds could be assigned for the switching times of these cells. A total of 70 cells were included in this plot.

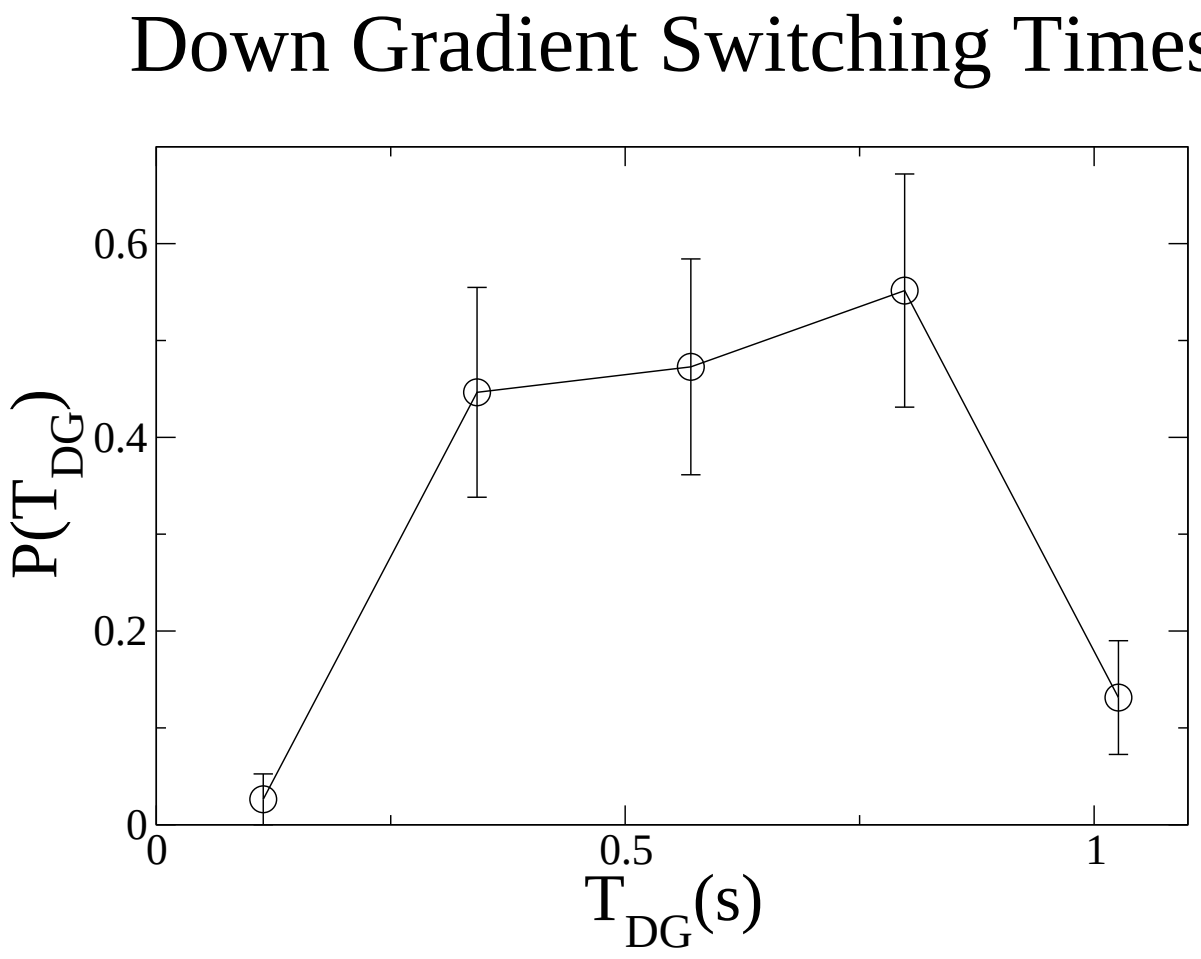

Figure 6.14: Down gradient switching times in optical trap.

Switching times for cells being moved down a gradient of attractant. Times are peaked around $0.5s$ with a roughly symmetrical distribution. No switching times are significantly above the $1s$ mark. 60 cells were used to generate the PDF

6.5) vs. while being taken down a gradient (Fig. 6.12). It can be seen that the characteristic long tail is distinctively absent for cells moving down a gradient. A possible explanation for this is the fact that when moving down a gradient, cells merely attempt to reverse their swimming direction. A characteristic sampling time ($\sim 0.6s$) is possibly inherent for these cells, upon the completion of which they can react by switching motor direction. In the steady state, on the other hand, cells are in the search for a chemical signal, hence have to occasionally run long paths to explore new regions, which is not required when detecting a gradient. For *E. coli* it has been shown before, that the methylation of the chemical receptors (sensors) control this low frequency response [31], which is a characteristic of an optimal search strategy [55].

6.8 PROPOSED CHEMOTACTIC STRATEGY FOR *VIBRIO ALGINOLYTICUS.*

Observations made in the previous sections allows us to propose a possible strategy for the chemotaxis of *V. alginolyticus*. Data on response of cells to chemical gradients along with their steady-state behavior helps us speculate the following mechanism being adopted by this strain. The cell's chemotaxis can be divided into two broad categories, (a) a search mode (or the steady state), when the cell does not sense any chemical gradient, and (b) a lock-on mode, where the cell senses a signal.

1. In the search mode, cells perform random walk in search of nutrients by changing swimming directions with the aid of flickings. The forward movements have infrequent long runs which helps in covering a large search area.
2. In the lock-on mode, which has been described in Table. 6.1, cells stay around the source of a gradient for an extended period by switching swimming direction (run-reverse) , and by reducing the rate of flicking from their steady state value. The run-reverse strategy has been observed for the marine strain of *Pseudomonas haloplanktis*, which are able to track motile algae (diffusing source of nutrients) by employing this mode [7]. For the current study, this strategy is strongly suggested from Fig. 6.12, where it can be seen that while going down gradients cells try to move backward by switching motor direction at a rate higher than the steady state value, while when taken up a gradient the motor very rarely switches. A combination of

these two conditions would enable cells to run and reverse around the maxima of the chemical gradient (alternating between up and down gradients). However, as the optical trap is unable to detect flagellar flicking, more work needs to be done to verify or falsify the speculation that flagellar flickings do indeed decrease when cells move along a gradient. As it has been shown that cells do not switch motor directions when taken up a gradient, it is obvious that they do not flick their flagellum when in this state. Thus, it remains to be investigated if flagellar flicking are suppressed when cells are taken down a gradient.

6.9 THE ENERGETICS OF FLAGELLAR FLICKING

As depicted in Fig. 6.4 and described in Section 6.8 the process of flagellar flicking has been proposed to be composed of a sequence of steps. In this section I will attempt to obtain the energetics of the flicking steps. All these estimates are rough, and careful calculations and measurements would be needed to improve their precision.

As the Navier-Stokes equation at low Reynolds number is time reversal symmetric, the movement that produces motion has to be asymmetric in time to provide a net displacement. In other words, as there is no inertia, any cyclic propulsion stroke would bring the body back to where it started from. Consequently, flagellar motility consists of a continuous wave which propagates backwards, propelling the cell body forward. The same logic applies to flagellar flicking, and a mere flick followed by a straightening of the flagellum would bring the cell back to its original orientation. In this case, rotation of the flagellum between the flick and straightening, breaks the symmetry, allowing the cell to reorient.

The first step in this process is when the flagellum and the cell body become non coaxial. This is as a result of a very slight bending of the flagellum, the energy for which is difficult to estimate from the present study. The thrust force, which is at an angle to the long axis of the cell body, it rotates by an angle of $\sim 80^o$ on average. Assuming that the thrust force being generated is the same as free swimming, one can estimate the time required to reorient the cell by the observed amount. Roughly, this process is equivalent to the application of a torque which rotates the cell body about an axis passing through its free end, and perpendicular to the plane of swimming, as shown Fig.

Table 6.1: Summary of Lock-on Mode

Chemical Signal	**Up gradient**	**Down gradient**
Response	Continue current direction	Reverse current direction

Summary of cell response when a chemical gradient is detected. This behaviour is for an attractant, for a repellent the opposite effect may be speculated along the lines of what has been seen for *E. coli* [2].

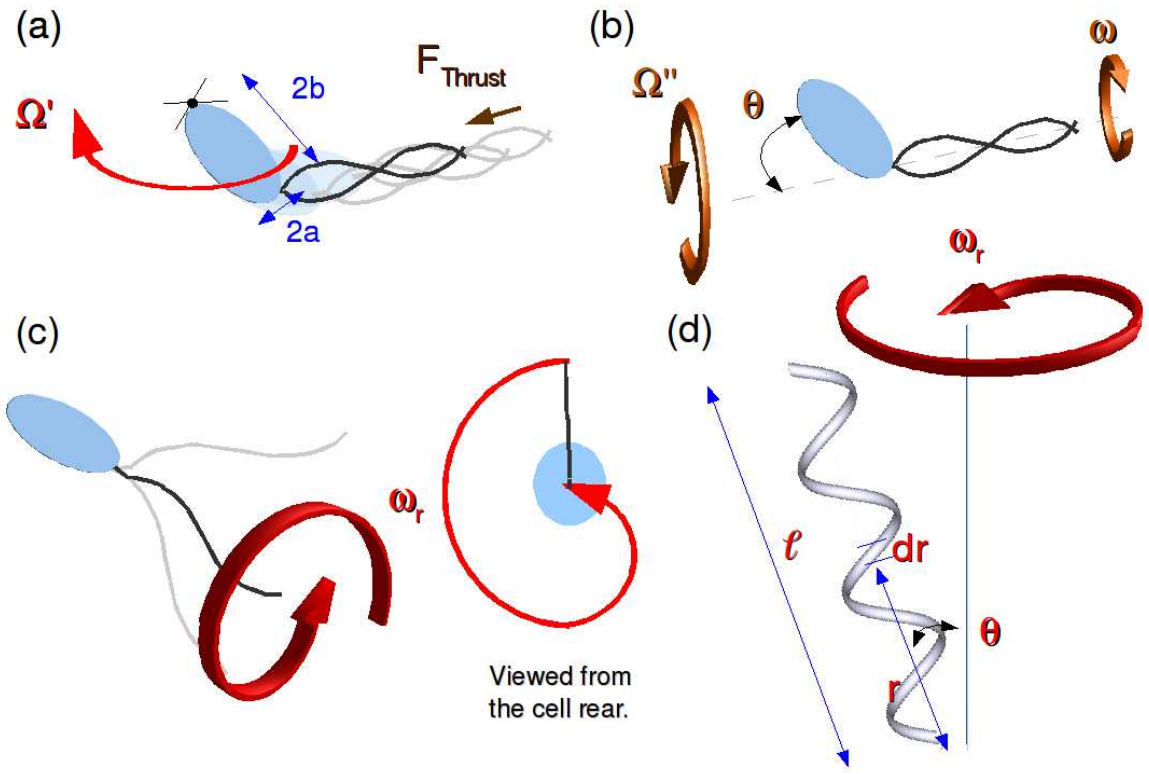

Figure 6.15: Energetics of the flagellar flick.

(a) Generation of thrust off the long axis of the cell body makes it rotate about its tip with a rotation rate of Ω'. (b) The reoriented cell body has to rotate around the axis of the flagellum, to conserve angular momentum being produced by the rotating flagellum. (c) The flagellum stops rotating after reorienting the cell, and realigns with the new cellular axis by rotating at a speed ω' with a decreasing radius around the long axis of the cell. A view from behind the cell shows the path traced by the flagellum. (d) Depiction of the formulation to calculate the torque on the flagellum as it reorients with the cell body making an angle θ with its long axis.

6.15 (a). Rigorously, the torque should be calculated by the component of the force perpendicular to the rotation arm, however let us assume it to be constant for a rough estimate. The drag of the cell body about this axis is given by $D_1^{'} = 8\pi\eta(2b)^3/3\log(\frac{2b}{a} - \frac{1}{2}) = 1.9 \times 10^{-19} N \cdot s \cdot m$, where $a(b)$ are the semi-minor (major) axes. Thus, assuming the free swimming value of the thrust force the torque about the axis of rotation is $T \approx A_0 \bar{V} \times 2b \approx 0.6\, pN \cdot 2.4\, \mu m = 1.44\, pN \cdot \mu m$ ($A_0 = 6\pi\eta b/(\log\frac{2b}{a} - \frac{1}{2})$, with a and b being taken from Table 5.3 while $\bar{V}$ has been obtained from Table 5.2 for cells of *V. alginolyticus*), which would impart an angular speed of $\Omega^{'} = T/D_1^{'} = 75\, rad/s$. Time required to turn by $\sim 80^0$ is $\tau_{bending} = (80 \cdot \frac{\pi}{180})/\Omega' \approx 0.018 s$. This value roughly agrees with observations made with a high speed camera (100 $frames/s$) via bright-field microscopy ($\sim 0.03 s$). I was intrigued to observe that the cell body does not rotate, along the axis of the flagellum, as shown in Fig. 6.15 (b), in response to the torque (N) being produced by the rotating flagellum, in order to conserve angular momentum. The rotational drag of the cell body about an axis, which is at an angle θ, with respect to the flagellar direction can be written as $D_1^{''} = D_1^{'} \sin^2\theta$. Using this relation, one can estimate the expected rotation rate $\Omega^{''} \approx N/(D_0^{'} \sin^2\theta) = 6.5\, rad/sec$, by applying torque balance for the cell body and flagellum. Note that this is the upper bound of the estimation, as the drag would be function of the angle (which changes from 0 to 80^0 on an average). The value for N has been obtained from Table 5.2. This slow rotation rate implies, that in the given flicking period ($\sim 0.018 s$) the cell body would rotate $6.5 \times 0.018 rad = 6.5^0$, which is very small and may not be detected, especially as it is out of the focal plane (as the observed flagella flick is along the focal plane, the cell rotation would be out of it).

In the ensuing step the flagellum stops rotating and the stationary flagellum relaxes back to align with the new direction of the long axis of the cell body. The angle of rotation of the flagellum, as denoted in Fig. 6.15 (c), is along a cone with a rotation rate of ω_R. The value of this rotation speed is measured from fluorescent video and is roughly $\omega_R/2\pi \approx 30 Hz$. In order to estimate the energy or power required for this movement, I have to calculate the rotational drag of the flagellum around the rotation axis as defined in Fig. 6.15 (d). A small flagellar segment of length dX is considered at a distance X from the center of rotation. The length of the segment is the component of the helix which perpendicular to the rotation direction, and thus contributes to the torque. From RFT one can estimate the drag coefficient per unit length for a small segment when it is moving normal to its the helical axis, which is given by $K_n = 4\pi\eta/(\ln(0.18\lambda/\alpha r) + 1/2)$ (See Fig. 1.2 for

the definition of the parameters). Thus the net torque on the whole flagellum (of length ℓ along the helical axis) is given by

$$N_R = \int_0^{\ell} (K_n dX \cdot \omega_R X \sin\theta) \cdot X \sin\theta = K_n \frac{\ell^3}{3} \cdot \sin^2\theta \cdot \omega_R$$

where $K_n dX \cdot \omega_R X \cdot \sin^2\theta$ is the viscous drag force on the segment. Thus the average torque will be a function of the angle made by the flagellum while it relaxes decreasing θ from $\bar{\theta} = 80^0$ to zero, on average. Thus the average torque is $\bar{N_R} = K_n \frac{\ell^3}{3} \cdot < \sin^2\bar{\theta} > \cdot \omega_R = K_n \frac{\ell^3}{3} \cdot 0.44 \cdot \omega_R$. Plugging in numbers from Table 5.2 and using the measured value of ω_R one obtains a torque of $T_R \approx 5000\, pn \cdot nm$. This value is indeed comparable to the torque produced by the flagellar motor of *V. alginolyticus* under high load conditions [49]. As mentioned earlier, I have observed that depletion of Na^+ ions from the motility media has the effect of stopping both motor rotation and flagellar flicking, indicating the possibility of the two processes being strongly coupled.

6.10 SUMMARY

It has been demonstrated in this chapter that cells of *Vibrio alginolyticus* employ a strategy of chemotaxis which is very different from the canonical run-and -tumble mode adopted by *E. coli.* Bacteria belonging to this strain (*V. alginolyticus*) are able to randomize swimming direction by flicking or bending the flagellum at its base. This, in addition to forward and reverse swimming, enables cells to quickly respond to a chemical stimulus and localize into regions rich in attractants. Table 6.2 summarizes and compares the proposed chemotactic strategy of *V. alginolyticus* and the mode adopted by *E. coli*.

The startling observation of flagellar flicking has brought forth several questions regarding the chemotactic strategy employed by *V. alginolyticus* and related strains. The widely different strategies used for chemotaxis by *E. coli* and *V. alginolyticus* raises interesting questions about how evolution has shaped a particular choice. *E. coli* swims in highly viscous environments (eg. in the animal intestine) where multiple flagellar motors are required for generation of greater thrust (when compared to a single motor). It is further possible that these cells are exposed to large

Table 6.2: Summary of chemotactic strategies of *V. alginolyticus* and *E. coli*

	Steady State	**Up a Gradient**	**Down a Gradient**
E. coli	Cells "run" with occasional "tumbles" to randomize direction	Bias for "runs" increases	Bias for "tumbles" increases
V. alginolyticus	Cells move "forward" and "reverse" with occasional "flicks" to randomize direction	Continues current state without switching or flicking	Reverses current state without flicking
Difference	*V. alginolyticus* integrates chemical signals both in forward and reverse swimming states		
	E. coli uses motor reversal to randomize direction, while *V. alginolyticus* "flicks" their flagella.		

Comparison of the proposed chemotactic strategy for of *V. alginolyticus* with that of *E. coli*, with prominent differences being pointed out.

nutrient patches which persist for some time. *Vibrio* cells on the other hand may be adopted to swim in lower viscosity and to respond to concentrated patches of chemicals which are mixed rapidly by ocean currents [3]. Knowledge of the chemotactic strategy would now make it possible to computationally simulate native environments for each cell type and observe which mechanism is more effective. As mentioned before, the chemotactic network of *E. coli* cells are known in detail [2, 8]. It would be interesting to try to explore how this network has to be modified in order to explain the additional functions being performed by *V. alginolyticus*. It was pointed out earlier that *Vibrio* cells possess two sets of flagella. The single polar flagella is used in low viscosity, while when in highly viscous environments, these cells express multiple flagella, called lateral flagella [21], very similar to those of *E. coli*. The lateral motors are driven by H^+ ions instead of Na^+ used by the polar flagellum [6]. It will be interesting to ask if *E. coli* cells have evolved from a marine species whereby they have lost their polar flagellum due to prolonged presence in regions of high viscosity and low Na^+ concentrations. Detection of flagellar flick in the optical trap would be significant for the unambiguous determination of the chemotactic strategy of *V. alginolyticus* which is the focus of research ongoing during the writing of this thesis. Probing whether cellular response is sensitive to the magnitude of a gradient is also left as future work.

7.0 MATERIALS AND METHODS

7.1 OPTICAL TRAP

An optical trap is formed by a laser beam (1064nm, Photop U.S.A., Sunnyvale, CA) tightly focused by a 100$\times$ oil immersion objective (Numerical Aperture 1.3). Flows in the sample chamber were produced by linear actuators (850A, Newport, Irvine, CA) used in the X-Z directions and a piezo actuator (P-841.60, Physik Instrumente, Irvine, CA) used in the Y direction (Fig. 2.3). The trapping beam is refocused onto a position sensitive detector (PSD) (DL100-7PCBA, Pacific Silicon Sensor, Westlake Village, CA). The output from the PSD is acquired using a data acquisition board (NI PCI-6259, National Instruments, Austin, TX). The linear actuators are controlled directly via analog outputs from the computer, while the piezo actuator is maneuvered via a controller (E-500.00, Physik Instrumente, Irvine, CA). The acquired data are analyzed using custom programs written with the C programming language. Video images are acquired with a CCD camera (CCD 72, DAGE-MTI, Michigan City, IN), digitized with a MPEG encoder card (WinTV-PVR-250, Hauppauge Computer Works, Hauppauge, NJ) and were analyzed by an image analysis software (ImageJ, NIH, Bethesda, MD).

The PSD outputs four signals VX_1, VX_2, VZ_1 and VZ_2 . The difference of the values gives the position of the laser spot along that particular direction. Thus $VZ_1 - VZ_2$ would be the position along the Z axis of the diode. The sum, on the other hand, measures the total power incident. In order to make the positions independent of intensity, the outputs are normalized by the sum. i.e. $VZ = \frac{VZ_1 - VZ_2}{VZ_1 + VZ_2}$ and $VX = \frac{VX_1 - VX_2}{VX_1 + VX_2}$, which are recorded. The diode housing includes an amplifier along with a normalization circuit which outputs the appropriate signal. An optical bandpass filter was placed at the front of the detector to selectively pass through the laser signal and block ambient light. A linear actuator was coupled to a syringe for the creation of flows in the sample chamber.

The DAQ card used had 4 analog output channels which were used to control the three axes of motion (Z, X and Y) and the laser power. The flow chamber was maneuvered with the actuators to trap a swimming bacteria and a sequence of appropriate measurements were initiated to perform a particular experiment. All instruments were controlled via single keystrokes of a computer keyboard.

Data analysis was performed via the C programming language. Image analysis was done with the GNU Image Manipulation Program (GIMP) (*http://www.gimp.org*) and ImageJ (*http://rsbweb.nih.gov/ij*). Data were presented with GNUPlot (*http://www.gnuplot.info*) and XMGrace (*http://plasma-gate.weizmann.ac.il/G*. Numerical analysis was done using custom computer codes and libraries from Numerical Recipes (*http://www.nr.com*). The FFTW (*http://www.fftw.org*) library was used to perform fast Fourier transforms of the recorded data.

7.2 CALIBRATION OF PSD CONVERSION FACTOR.

The PSD outputs normalized voltages which correspond to the position of the laser beam. The conversion factor C, is the parameter which would then convert these voltages into actual position in the optical trap. C would depend on the shape of the object only, as the PSD output has been normalized to be independent of laser intensity. Hence, the conversion factor has to be calibrated for bacterial shapes. Cells are attached to cover slips which are coated with *poly-D-lysine* (P2636, Sigma-Aldrich, St. Louis, MO) according to standard protocols. The bacterium is next translated with a pre-calibrated speed, by translating the sample stage, such that the tip of the cell passes through the center of the trap .The movement of the cell through the center gives a linear change in the output of the PSD, which is recorded. The process is depicted in Fig. 7.1. The ratio of the change in the position of the bacterial tip to the output of the PSD, gives the required conversion factor. i.e. $C = \frac{\Delta z}{\Delta VZ}$. It is to be noted that an appropriate bacterial cell should be used to obtain the corresponding conversion factor, as C would depend on the index of refraction along with the cell shape, which can be different for individual strains. Also, the conversion factor is independent of the length of the bacterium, as the laser beam is only influenced by the curved end of the cell. It is well known that the curvature of the cell tip does not appreciably change for cells belonging to the

same strain, although their cell length may vary according to their growth stage. For convenience, cells which lack flagella are used for this calibration (*E. coli* strain YK4516, *V. alginolyticus* strain YM14).

7.3 CALIBRATION OF TRAP CONSTANT.

The force exerted on an object in an optical trap is given by the product of the displacement from the center of the trap and the trap constant (k). k is dependent on the geometry of the object being trapped in addition to being a function of the the laser strength. Higher the intensity stronger is the trapping force. Hence, k has to be calibrated for every bacterial shape (for each strain, for reasons discussed in the end of the previous section), and for the laser strength. Further, high numerical aperture objectives are designed to work at the surface of glass slides, as index matching oils are used to minimize loss of resolution due differences in refractive indices. Moving deeper into the fluid bulk would decrease trap strength due to looser focusing of the laser beam. Thus, calibration has to be performed for the given distance from the glass surface ($\sim 100\,\mu m$ from the lower surface).

As the drag of the flagellum is not well known, and that of the cell body is, k is calibrated with bacterial strains which lacked flagella (YK4516 for *E. coli* and YM14 for *V. alginolyticus*). Trapping a cell via Configuration C (Fig. 2.3) and applying a ramped flow one obtains the trap constant. Flow is applied along the Z axis and displacements along the same direction are recorded. Thus, for a change of flow velocity of δU, if the displacement from the center of the trap is given by $\Delta(z-z_0)$, where z_0 is the center of the trap, the trap constant will be given by $k = \frac{A_0 \Delta U}{k\Delta(z-z_0)}$ (A_0 is the drag coefficient of the cell body).

7.4 FLUORESCENCE MICROSCOPY FOR FLAGELLAR IMAGING

Flagellar filaments are extremely thin providing very little contrast for imaging via conventional bright-field microscopy. A convenient technique is to label them with fluorescent dyes for visu-

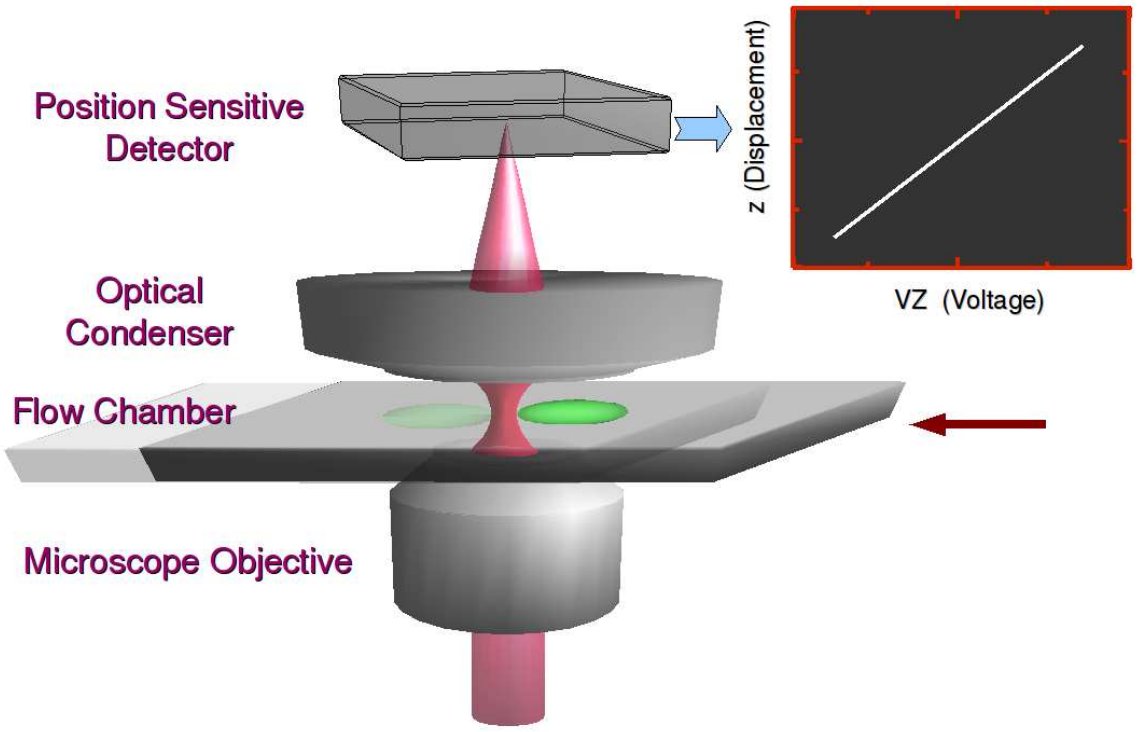

Figure 7.1: Conversion factor.

Diagrammatic depiction of the conversion factor calibration. A bacterial cell is stuck on the glass surface and translated with a known speed, such that its tip passes through the center of the optical trap. The slope of the tip position vs. voltage output from the PSD is the required conversion factor.

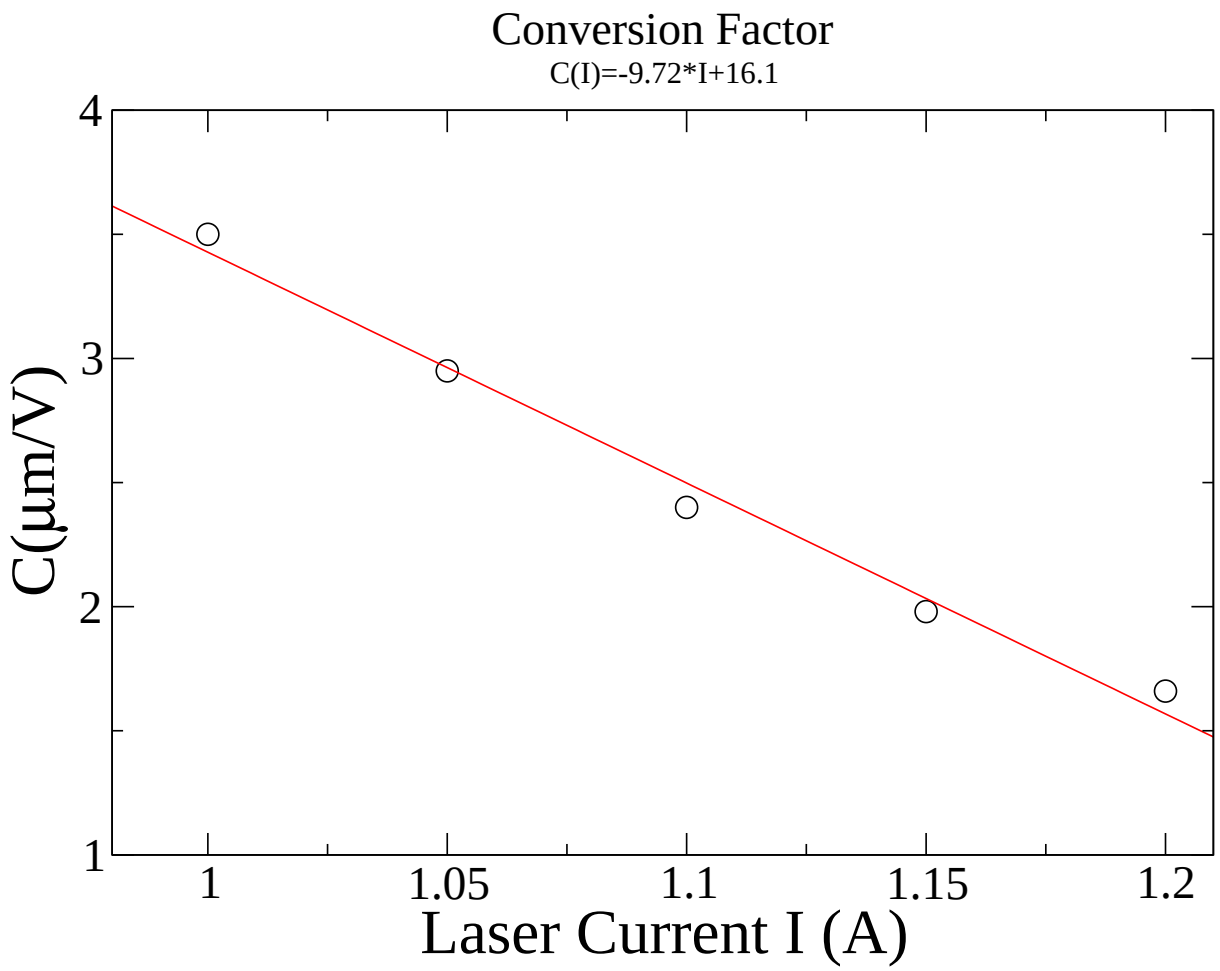

Figure 7.2: Conversion factor calibration for *E. coli* cells.

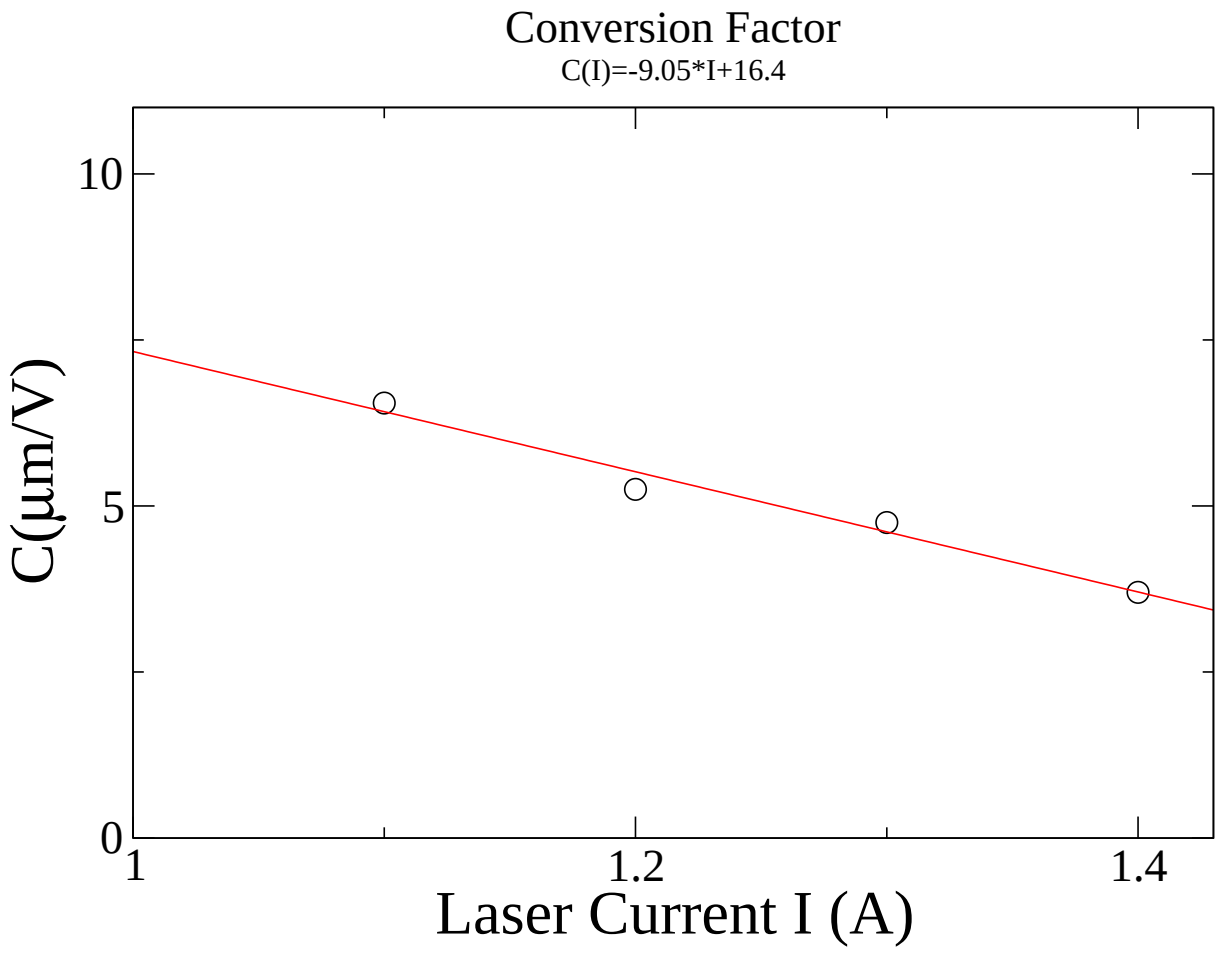

Figure 7.3: Conversion factor calibration for *V. alginolyticus*.

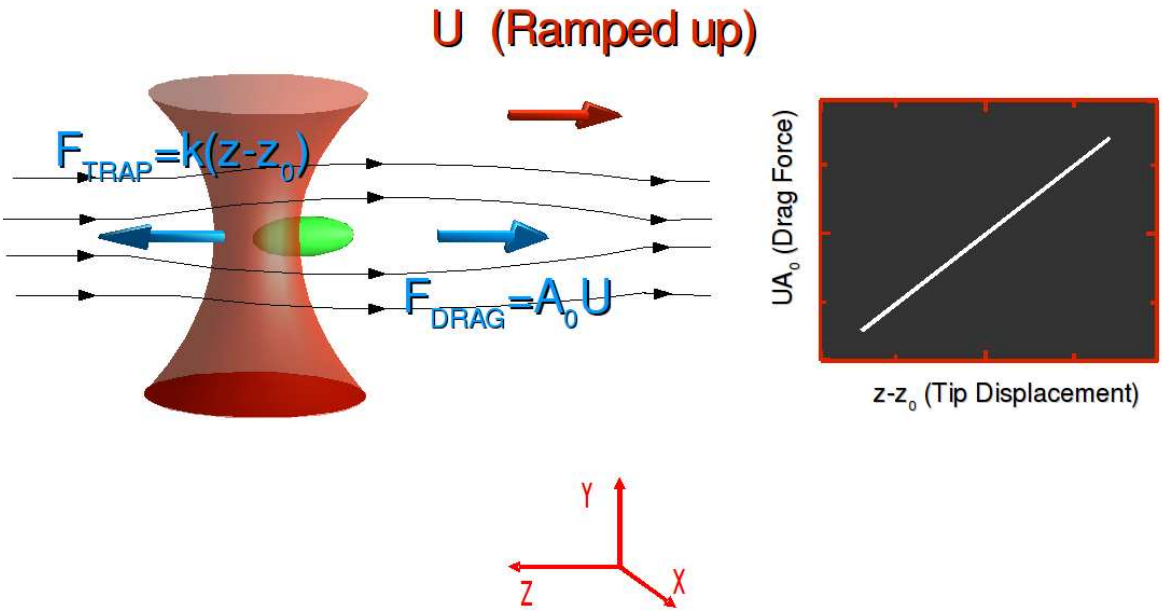

Figure 7.4: Trap constant calibration.

Description of the calibration process for the trap constant (*k*). A bacterial cell lacking flagella is trapped perpendicular to the optical axis while in the fluid bulk, with the aid of an imposed flow. The flow speed is ramped up and the corresponding change in the displacement of the tip from the trap center is recorded. The slope of the plot of flow speed vs. displacement of the cell tip gives the trap constant *k*. It is to be noted that the trap constant is dependent on the strain of the bacterium used, the laser beam strength and the distance at which the calibration is performed.

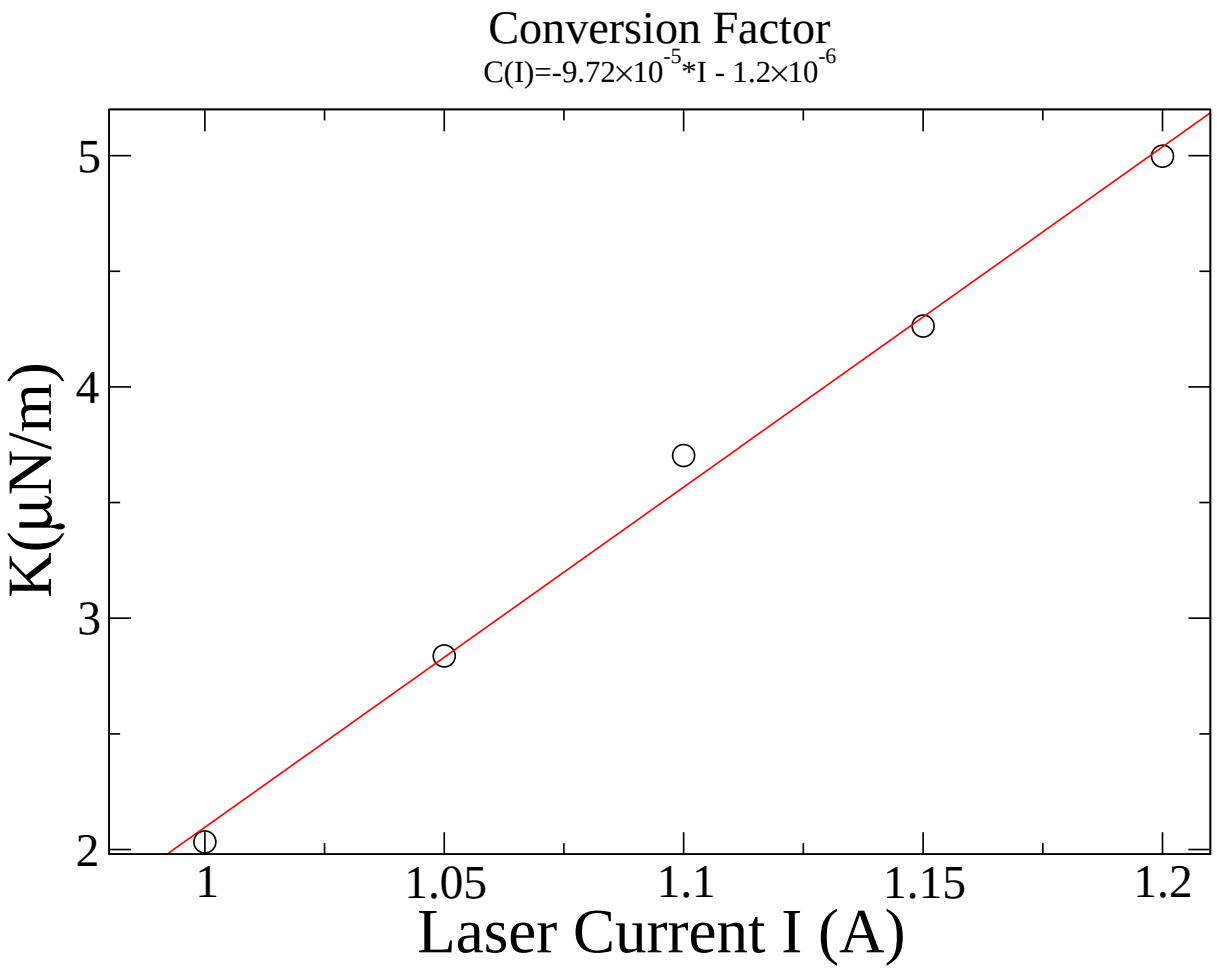

Figure 7.5: Trap constant calibration for *E. coli.*

For cells near the surface ($z \sim 5\,\mu m$).

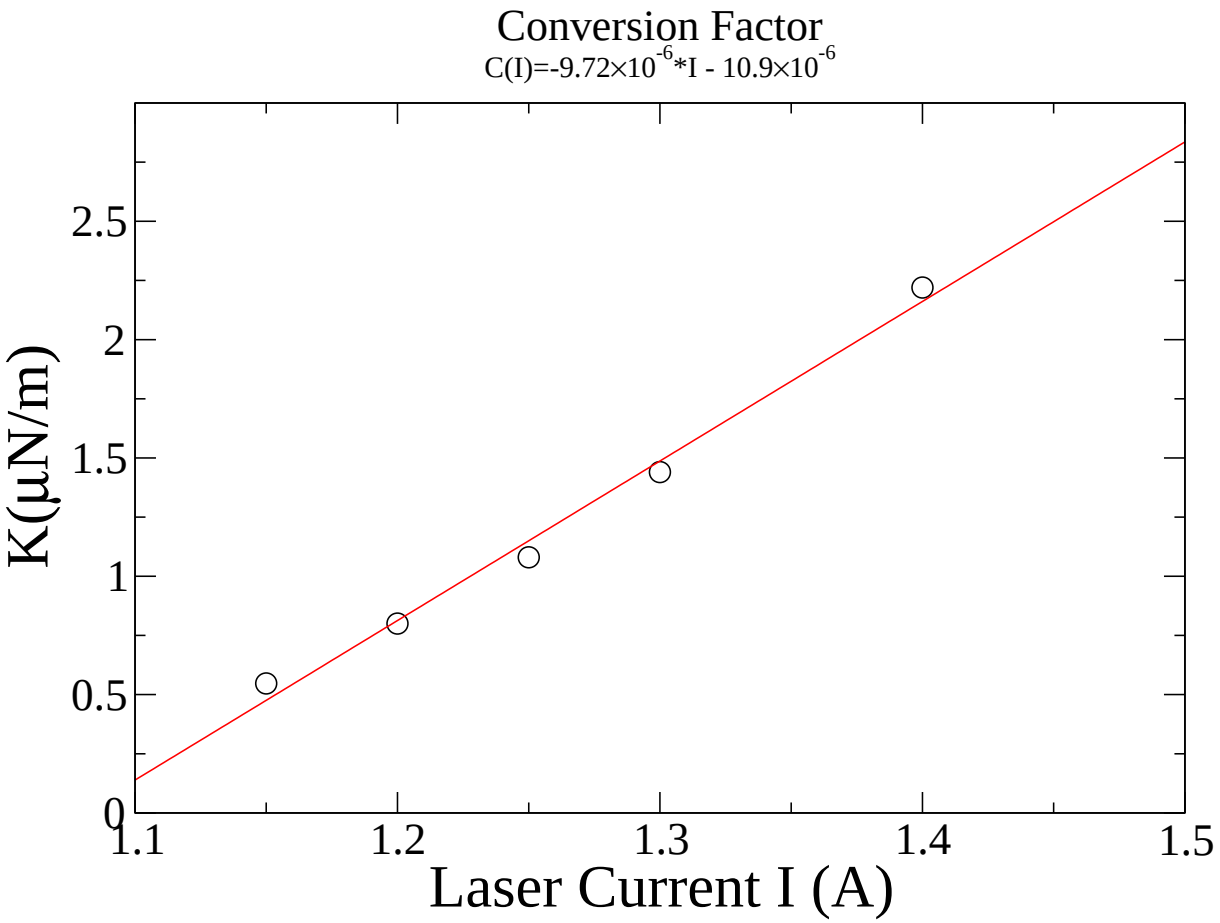

Figure 7.6: Trap constant calibration for *V. alginolyticus*.

For cells in the fluid bulk ($z \sim 100\,\mu m$).

alization [54, 23]. Electron microscopy has also been used in the past for this purpose [38]. The specific protocols for the different bacterial strains are given below. I visualize the filaments when they are at rest, as it is difficult to image rotating filaments. It is however reasonable to do this, as flagellar filaments are rigid and do not deform when rotating [54, 52]. The observed images along with the dimensions for the strains studied are summarized in Table 5.3.

Cells were imaged with a Nikon epifluorescence microscope (TE3000) with appropriate filters and illuminated by a Xenon arc lamp. Cells were immobilized by oxygen depletion to enable imaging. The protocols used for the different strains used are described below.

Cy3 mono functional succinimidyl ester (PA23001, GE Healthcare, Piscataway, NJ): Cells of *E. coli* and *C. crescentus* were labeled using this dye. The basic protocol is outlined in [20]. $0.5\,ml$ of bacteria containing motility media are mixed with one package of Cy3 and $25\,ml$ of 1.0 M $NaHCO_3$. The suspension was incubated for $90\,min$ by shaking at $100\,rpm$ while being kept in the dark. Excess dye was removed by washing with motility media. The cells were viewed using a Cy3 filter set (Chroma, Rockingham, VT).

NanoOrange (N-6666, Invitrogen, Carlsbad, CA): *V. alginolyticus* cells possess a membrane on the flagellum and thus were labeled using this dye. NanoOrange attaches non specifically to protein and hence labels the flagellum [23]. $30\,\mu L$ of NanoOrange Component A was added to $1\,mL$ of motility media containing cells. Bacteria were observed after incubation at room temperature for $30\,min$. This dye is fluorescent only when bound to protein, and thus excess dye does not require being washed off. Flagella were clearly visible when viewed with a blue filter set. Swimming was inhibited by Oxygen depletion.

7.5 BACTERIAL GROWTH PROTOCOLS

The growth and motility media used for the individual bacterial strains used in this study are described below. All percentages are in weight/volume unless otherwise mentioned.

E. coli (HCB30, smooth swimming mutant; YK4516, mutant lacking flagella): Cells were grown overnight in Tryptone broth (0.4% peptone, 0.1% $NaCl$, 0.4 ml of $1\,M\ NaOH$) [20] at 33^oC with vigorous shaking (200 RPM). Overnight culture was diluted 1:100 into fresh growth media

and grown to early log phase (4.5 hrs). Cells were washed twice in motility medium (10 $mM\,KPO_4$, 0.1 mM EDTA, 0.1 mM glucose, 2×10^{-4}%(v/v) Tween 20) by centrifugation (2000 $\times\, g$ for 5 min) and gently re suspended. Final solution was diluted 1:3 into motility media for the experiments.

P678-54, minicell producing mutant of *E. coli* [1]: Cells were grown overnight in Nutrient broth (0.8% Difco Nutrient Broth, 0.6% $NaCl$, 0.1% Yeast extract) at 33^oC with vigorous shaking (200 RPM). Overnight culture was diluted 1:100 into fresh growth media and grown to mid log phase (4.5 hrs). Log phase media was centrifuged for 2 min at 2000 $\times\, g$, and the supernatant (top half) was taken to isolate minicells. This was diluted 1:3 into fresh growth medium for the experiments. It is to be noted that as I did not posses a minicell producing mutant of *E.coli* which was also a smooth swimmer, I performed experiments in growth medium (Nutrient broth). Bacteria transferred from nutrient depleted into fresh media behave primarily as smooth swimmers, enabling measurements.

YB4038, mutant of *C. crescentus* lacking pili: Cells were grown overnight in PYE medium (0.2% peptone, 0.1% Yeast extract, 0.6 $mM\ MgSO_4$, 0.5 $mM\ CaCl_2$) at 30^oC with vigorous shaking (200RPM) [33]. Overnight culture was diluted 1:100 into fresh media and grown to early log phase (5 hrs). Cells were washed twice in distilled water by centrifugation (5000 $\times\, g$ for 5 min) and gently re-suspended. Final solution was diluted 1:3 into distilled water for the experiments. Although *C. crescentus* cells were wild type, their motile cells (swarmer cells) were observed to be primarily smooth swimming when transferred into distilled water. This is possibly due to the fact that the fresh media is richer in oxygen, which induces smooth motion.

Vibrio alginolyticus (YM4 wild type; YM42, smooth swimming mutant; YM14 mutant lacking flagellum,): Basic protocol adopted from [49]. Cells were grown overnight in VC media (0.5% peptone,0.5% yeast extract, 0.4% K_2HPO_4, 3%$NaCl$, 0.2% glucose) at 30^oC with vigorous shaking (200 RPM). Overnight culture was diluted 1:100 into VPG media (1% peptone,0.4% K_2HPO_4, 3% $NaCl$, 0.5% glycerol) and grown to early log phase (3 hrs). Cells were washed twice by centrifugation (2000 $\times\, g$ for 5 min) and gently re suspended in TMN medium (50 mM Tris-$HCl(pH\,7.5)$, 5 $mM\ MgCl_2$, 5 mM Glucose, 300 $mM\ NaCl + KCl$). The cells were incubated at 30^0C for 45 min to ensure maximum motility. Final solution was diluted 1:10 for the experiments.

7.5.1 Controlled Variation of ω for cells of *V. alginolyticus.*

The flagellar rotation rate was controlled by the concentration of *NaCl* in TMN media. For measurement of the propulsion matrix elements in Chapter **??**, a salt concentration of $30\,mM$ was used. Table 7.1 provides the *NaCl* and *KCl* concentrations used and the corresponding dynamics observed. The increase of ω saturates at a salt concentration of $300\,mM$, beyond which flagellar rotation is increased by incrementing the temperature.

7.5.2 Chemotaxis of *V. alginolyticus*

Wild type strain (YM4) of *V. alginolyticus* were grown according to protocols specified above and are suspended in TMN media, for the observation of chemotactic response. A $10\,mM$ solutions of L-serine (LAA-21, Sigma-Aldrich, St. Louis, MO) and phenol were used as an attractant and a repellent respectively [25]. VPG motility medium was used for the experiments which had a *NaCl* concentration of $30\,mM$. If *NaCl* concentration is set to zero in VPG medium, cells are still observed to swim. However, HG medium ($50\,mM\ HEPES-KOH$ (pH 7.0), $5\,mM$ glucose and $5\,mM\ MgCl_2$), when used with no *NaCl*, stopped motor rotations completely [43].

Table 7.1: Controlled variation of ω for *V. alginolyticus.*

Cell no.	**Salt concentration in motility media**		**Temp.**	**Dynamical variables**		
n_G	$NaCl\,(mM)$	$KCl\,(mM)$	$T\,(^0C)$	$\omega/2\pi\,(Hz)$	$\Omega/2\pi\,(Hz)$	$V\,(\mu m/s)$
60	0	300	25	96(3)	11(1)	13(0.5)
20	10	290	25	260(10)	24(2)	24(2)
20	20	280	25	310(30)	35(3)	28(2)
100	30	270	25	560(12)	49(2)	41(2)
50	300	0	25	815(20)	60(3)	63(5)
40	300	0	38	1050(28)	65(4)	76(5)

Control of bacterial swimming by changing the *NaCl* concentration in motility media for *V. alginolyticus*. Dynamics measured for varying salt concentrations are shown. The increase of rotation rate saturates at a *NaCl* concentration of $300\,mM$, which is in agreement with the results seen in Ref. [49]. Further increase in ω is obtained by incrementing the temperature to $38\,^0C$.

APPENDIX A

DERIVATION OF PROPULSION MATRIX ELEMENTS FROM RFT

I wish to derive the propulsion matrix elements from the basic principles of RFT. The idea is to relate the velocities and the torques in terms of the geometrical parameters of the flagellum. As mentioned earlier, RFT divides the flagellum into small segments of length w (Fig. 5.1). The drag coefficients per length of this segment, when translated either tangential (K_t) or normal (K_n) to its axis can be evaluated. This is done by solving Stokes equation for the given geometry of the segment, with the result [35]

$$K_t = 2\pi\eta/(\ln(2w/r) - 1/2),$$

$$K_n = 4\pi\eta/(\ln(2w/r) + 1/2),$$

where r is the radius of the filament and η is the fluid viscosity. It has been indicated in Section 5.1.3, how different authors have assumed distinct forms of K_t and K_n. The derivations of the propulsion matrix elements are however independent of the choice of specific formulations.

Let us begin by looking at the helical wave traveling along the flagellum (Fig. A-1). The flagellum rotates at a speed of ω, hence the phase velocity of the wave travelling on the flagellum V_w can be written as $V_w = \lambda\omega/2\pi$, where λ is the pitch of the helix. Thus, as a whole, the flagellum is moving in the negative X direction with swimming speed V, while the wave is travelling in the positive X direction with the phase velocity V_W. However, the phase velocity can be written in terms of the a velocity along the contour of the flagellum c, is related to V_W as $c = V_W/\alpha$, where α is the cosine of the helix angle ($\alpha = \cos\phi$). The speed of each segment in the laboratory frame is

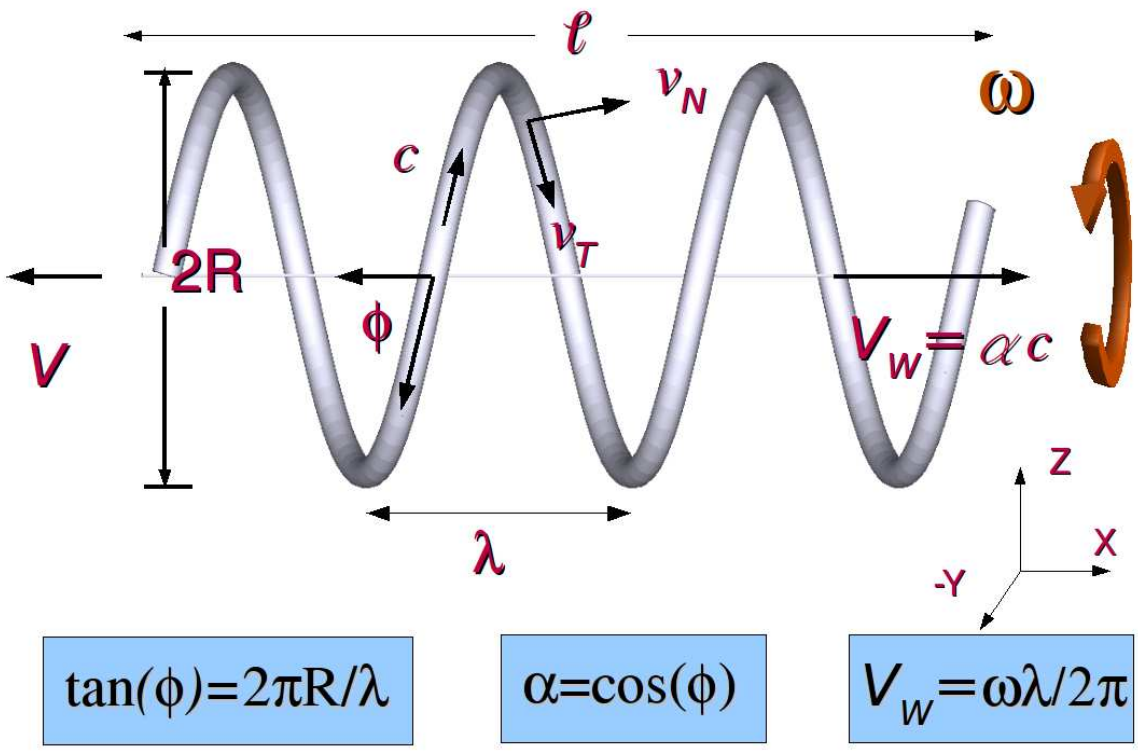

Figure A-1: RFT derivation.

Parametrization for the derivation of propulsion matrix elements from RFT. Net velocity of each segment is due to the combination of the forward swimming speed of the whole flagellum (V) and the wave speed of the helix (V_W) which moves in the opposite direction. Variables can be defined in its terms of the helix angle (ϕ), as shown. ϕ is constant over the length of the helix.

therefore, a sum of c along the flagellum contour and $(V_w - V)$ along the axis. Resolving the speed of each flagellar segment along the normal and tangential directions of its axis one gets

$$v_t = (V_w - V)\cos$$

$$v_n = (V_w - V)\sqrt{1-\cos^2\phi}$$

Thus the net force due to the normal and tangential motions of the flagellar segment (due to the fluid on the flagellum) projected onto the swimming direction is

$$dF_{thrust} = \{K_t[(V_w - V)\cos\phi - c]\cos\phi + K_n(V_w - V)[1-\cos^2\phi]\}ds.$$

Total force when summed over the whole flagellar length is then

$$F_{thrust} = \int_0^L (K_t[(V_w - V)\cos\phi - c]\cos\phi + K_n(V_w - V)[1-\cos^2\phi])ds$$

$$= K_t(V_w - V)(\int_0^L \cos^2\phi\, ds - \int_0^L \cos\phi\, c\, ds) + K_n(V_w - V)[\int_0^L ds - \int_0^L \cos^2\phi\, ds].$$

Let us assume $\int_0^L \cos\phi\, ds = \ell$ and $\cos^2\phi = \beta$. The former is the length of the flagellum along the helical axis. The net thrust of the flagellum then becomes,

$$F_{thrust} = K_t L\,[(V_w - V)\beta - V_w) + K_n L(V_w - V)(1-\beta)$$

$$F_{thrust} = LV_w[K_t(\beta - 1) + (1-\beta)K_n] - LV[\beta K_t + (1-\beta)K_n], \qquad (A.1)$$

where $\gamma_k = K_t/K_n$. Similarly the torque on the flagellum about the helical axis is given by the component of dF_{thrust} normal to the helical axis multiplied by the lever arm, which is the helix radius, obtaining

$$dN = \{RK_t[(V_w - V)\cos\phi - c]\sin\phi + RK_n(V_w - V)\sin\phi\cos\phi\}ds$$

Hence, the total torque is given by

$$N = \int_0^L [RK_t[(V_w - V)\cos\phi - c]\sin\phi + RK_n(V_w - V)\sin\phi\cos\phi]ds$$

$$= RK_t(V_w - V)(\int_0^L \cos\phi \sin\phi - \int_0^L c\sin\phi)ds + RK_n(V_w - V)\int_0^L \sin\phi\cos\phi ds$$

$$= RK_t((V_w - V)L\cos\phi\sin\phi - \frac{V_w L}{\cos\phi}\sin\phi) + RK_n(V_w - V)L\sin\phi\cos\phi$$

$$N = V_w RL(K_t\cos\phi\sin\phi - K_t\tan\phi + K_n\sin\phi\cos\phi) - RLV(K_t\cos\phi + K_n\sin\phi\cos\phi) \quad (A.2)$$

Now, looking back at Eqn. 3.3 I had,

$$-F_{thrust} = AV - B\omega$$

$$F_{thrust} = -AV + B\frac{2\pi V_w}{\lambda}$$

Comparing with Eqn. A.1 we get,

$$A = L[\beta K_t + (1-\beta)K_n] = K_n L[\beta\gamma_k + (1-\beta)] = K_n L(1-\beta)[\gamma_k\frac{\beta}{1-\beta} + 1] = K_n L(1-\alpha^2)[\gamma_k\frac{\alpha}{1-\alpha} + 1], \quad (A.3)$$

and

$$B\frac{2\pi}{\lambda} = L[K_t(\beta - 1) + (1-\beta)K_n],$$

$$\Rightarrow B = \frac{\lambda}{2\pi}K_n L[\gamma_k(\beta-1) + (1-\beta)] = K_n L(\frac{\lambda}{2\pi})(1-\beta)(1-\gamma_k) = K_n L(\frac{\lambda}{2\pi})(1-\alpha^2)(1-\gamma_k). \quad (A.4)$$

Again, Eqn. 3.4 gave us

$$N = -BV + D\omega$$

$$N = -BV + D\frac{2\pi V_w}{\lambda}$$

Comparing with Eqn. A.2 we get,

$$D\frac{2\pi}{\lambda} = RL(K_t\cos\phi\sin\phi - K_t\tan\phi + K_n\sin\phi\cos\phi)$$

$$\Rightarrow \quad D = (\frac{\lambda}{2\pi})[\frac{\lambda}{2\pi}tan(\phi)]K_n L(\gamma_k\cos\phi\sin\phi - \gamma_k\tan\phi + \sin\phi\cos\phi)$$

$$= K_n L(\frac{\lambda}{2\pi})^2[\gamma_k(\sin^2\phi - \tan^2\phi) + \sin^2\phi]$$

$$\Rightarrow D = K_n L(\frac{\lambda}{2\pi})^2(1-\cos^2\phi)[\gamma_k(1-\cos^{-2}\phi)+1] \quad \text{(A.5)}$$

$$= K_n L(\frac{\lambda}{2\pi})^2(1-\alpha^2)[\gamma_k(\frac{\alpha^2-1}{\alpha^2})+1]. \quad \text{(A.6)}$$

Here the relation $\tan\phi = \frac{2\pi R}{\lambda}$ has been used. By comparison of the other coefficient one obtains $B = RL(K_t\cos\phi + K_n\sin\phi\cos\phi)$, retaining Eqn. A.4.

I thus have derived above (Eqns. A.3, A.4 and A.5) expressions for A, B and D, as shown in Eqns. 5.6 from the basic definitions of RFT . Different variants of RFT can be applied by choosing appropriate forms of K_t and K_n, as shown in Table 5.1.

APPENDIX B

SUMMARY OF LIGHTHILL'S SBT

According to Lighthill's 1976 paper on "Flagellar Hydrodynamics" [34], the dimensionless velocity v, the torque t , and the efficiency e are given by (Eqs. 57, 58, 59, 95 and 103 of [34]):

$$v = \frac{(1-\alpha^2)Z}{Y} \times \frac{1}{(1+\frac{\psi a_E}{L})}, \tag{B.1}$$

$$t = \frac{1}{Y} \times \frac{(1+\frac{\Psi a_E}{L})}{(1+\frac{\psi a_E}{L})}, \tag{B.2}$$

$$e = \frac{4\pi Y}{\alpha^2(1-\alpha^2)Z^2} \times (1+\frac{\Psi a_E}{L})(1+\frac{\psi a_E}{L}), \tag{B.3}$$

where $\alpha = \cos\phi$ is the directional cosine of the helix, a_E is the effective radius of the cell body, and L is the total length of the flagellum. The other quantities, Y, Z, ψ and Ψ are functions of α and are given by:

$$Z = [-1 - \ln\varepsilon + A_1(\alpha)]$$

$$Y = -(1-\alpha^2) - (2-\alpha^2)\ln\varepsilon + \alpha^2 A_1(\alpha) + 2(1-\alpha^2)A_2(\alpha)$$

$$\psi = \Psi - \frac{\frac{3}{2}\alpha^2(1-\alpha^2)Z^2}{Y} \qquad \text{(B.4)}$$

$$\Psi = \frac{3}{2}[2-\alpha^2-\frac{3}{\alpha}+\frac{2}{\alpha}\ln(kL)-(1+\alpha^2)\ln\varepsilon-2A_3(\alpha)-(1-\alpha^2)A_1(\alpha)]/[1+\frac{\ln(\ell/a_E)-1.5}{2(\ln(\ell/\zeta)-2)}] \qquad \text{(B.5)}$$

In the above equation, $\zeta = \ell\exp(-\frac{\alpha\Psi}{3}-1)$ with $\ell = L\cos\phi$ and r the radius of the flagellar filament, and $A_1(\alpha)$, $A_2(\alpha)$, and $A_3(\alpha)$ are given by the following definitive integrals:

$$A_1(\alpha) = \int_\varepsilon^\infty \frac{\theta\sin\theta d\theta}{[\alpha^2\theta^2+2(1-\alpha^2)(1-\cos\theta)]^{\frac{3}{2}}} + \ln\varepsilon,$$

$$A_2(\alpha) = \int_\varepsilon^\infty \frac{\sin^2\theta d\theta}{[\alpha^2\theta^2+2(1-\alpha^2)(1-\cos\theta)]^{\frac{3}{2}}} + \ln\varepsilon,$$

$$\begin{aligned} A_3(\alpha) &= -\frac{1}{2}[\int_{-\theta_1}^{-\varepsilon} \frac{d\theta}{[\alpha^2\theta^2+2(1-\alpha^2)(1-\cos\theta)]^{\frac{1}{2}}} + \\ &\quad \int_\varepsilon^{\theta_2} \frac{d\theta}{[\alpha^2\theta^2+2(1-\alpha^2)(1-\cos\theta)]^{\frac{1}{2}}} + 2ln\varepsilon - \frac{\ln(\theta_1\theta_2)}{\alpha}], \end{aligned}$$

where $\varepsilon = 5.2\alpha r/\lambda$, and $\theta_1 = \frac{2\pi}{\lambda}\alpha L_1$ and $\theta_2 = \frac{2\pi}{\lambda}\alpha L_2$ represent the ends of the flagellum. For a long flagellum the term $\ln(\theta_1\theta_2)$ in the above equation can be replaced by averaging L_1 over the length of the flagellum. It can be shown that $<\ln(\theta_1\theta_2)>= 2\ln(kL)-2$.

APPENDIX C

DIFFERENCE OF FLOW FIELDS BETWEEN ELLIPSOID AND SPHERE

Here I wish to evaluate the difference in flow fields experienced by the flagellum when the ellipsoidal cell body is approximated as a sphere. The radius of the sphere is chosen so that it has the same linear drag.

It has been shown by Chwang and Wu that a uniform flow around a ellipsoid can be modeled by a uniform distribution of Stokeslets and doublets between the foci [19]. It is known that a Stokeslet (a delta function body force on the fluid, i.e. $\vec{F(\vec{r})} = \vec{F}\delta(\vec{r})$) $\vec{F} = (F,0,0)$ produces a velocity field of

$$\vec{u}(r) = \frac{F}{8\pi\eta}(\frac{x^2+r^2}{r^3}, \frac{xy}{r^3}, \frac{xz}{r^3}).$$

However if the observation point is along the x axis then $\vec{u}$ becomes,

$$\vec{u}(x) = \frac{F}{8\pi\eta}(\frac{x^2+x^2}{x^3}, 0, 0) = \frac{F}{4\pi\eta}(\frac{1}{x}, 0, 0).$$

Let us assume the ellipsoidal cell body has b and a as its semi -major and -minor axes respectively (Fig. C-1). The origin is located at the joint of the cell body and the flagellum. The foci are thus located at $-b(1-\vartheta)$ and $-b(1+\vartheta)$, where ϑ is the eccentricity of the ellipsoid. Let us assume an uniform Stokeslets distribution of $-F'$ per unit length between the foci. Hence the induced velocity field at an arbitrary observation point along the x axis would be

$$\vec{u_1}(x_0) = -\frac{F'}{4\pi\eta}(\int_{-b(1-\vartheta)}^{-b(1+\vartheta)} \frac{1}{(x_0-x)}dx, 0, 0) = -\frac{F}{4\pi\eta}(ln(\frac{x_0+b(1+\vartheta)}{x_0+b(1-\vartheta)}), 0, 0)$$

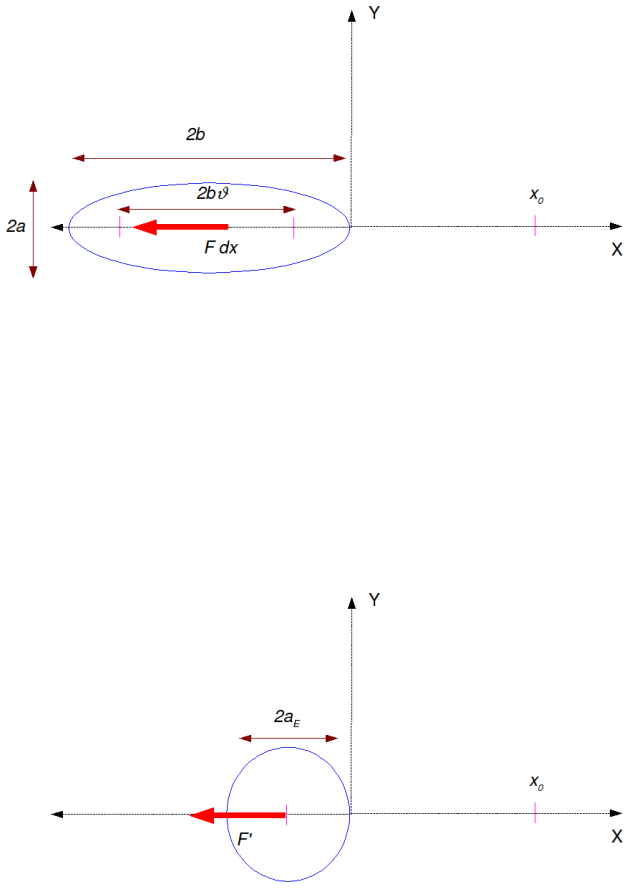

Figure C-1: Flow fields for ellipsoidal and spherical cell bodies.

The distribution of Stokeslets and doublets for an ellipsoidal and spherical cell body. For the former an uniform distribution of Stokeslets are used, while a single Stokeslet is placed at the center of the sphere.

The net drag on the ellipsoid is the total magnitude of the Stokeslets, which is $F' \times 2b\vartheta$, the length between the foci being $2\vartheta b$.

The ellipsoidal head is then replaced by a sphere which has the same linear drag. The effective radius of the sphere would then be $a_E = 2b/3[ln(2b/a) - 1/2]$. This is because the drag of the ellipsoidal head is given by $A_0 = 4\pi\eta b/[ln(2b/a) - 1/2]$, and a sphere which has the same linear drag can be found by equating $6\pi\eta a_E$ to A_0. Thus this sphere has its center at $x = -a_E$ and has a Stokeslets of strength $-F''$. But as the linear drag of the ellipsoid and sphere are the same, we have $F'' = 2F'b\vartheta = A_0 V$, where V is the cells average swimming speed. I can then write down the velocity field seen at an observation point along the x axis when the sphere replaces the ellipsoidal cell body.

$$\vec{u_2}(x_0) = -\frac{F''}{4\pi\eta}\left(\frac{1}{(x_0 + a_E)}, 0, 0\right)$$

Let us take a look at the geometrical parameters of the cell body for the strains under study. *E. coli* minicells are spherical in shape and hence do not have to be replaced. It can be observed, that the highest aspect ratio is for the cells of *V. alginolyticus*, which would have the greatest error by this replacement. Hence, I will examine the difference in the flow fields, for of *V. alginolyticus*, which would represent the maximum error sustained amongst the strains under study, by the replacement of the ellipsoid by a sphere. Figure C-2 shows the variation of $\vec{u_1}(x_0)$ and $\vec{u_2}(x_0)$ as x_0 varies over length scales comparable to the flagellar length.

Lighthill in his derivation was able to separately treat the different sources of LRHI in swimming bacteria. They are contributions due to flagella-flagella interactions and cell body-flagella interactions. As stated before, the dimensionless torque t is not effected appreciably by LRHI. The contribution of the cell body-flagella interactions to v is smaller ($\sim$ 10% for *V. alginolyticus* and smaller still for the other strains) than the contribution due to flagellum/flagellum interactions (See Fig. 5.2).

It can be seen from Fig. C-2, that the difference between the flow fields when a ellipsoid is replaced by a sphere, is quite small ($\sim$ 10%), with the sphere predicting a larger flow field at the flagellum, due to its proximity to the Stokeslet at the sphere center.

Lighthill did not attempt to explicitly match boundary conditions at the surface of the sphere. In order to do this one has to include a doublet with an appropriate strength in addition to the

Table C-1: Dimensions of the cell body and equivalent spheres.

Bacterial Strain	**Cell Size**		**Aspect Ratio**	**Eccentricity**	**Stokeslet Dist.**
	$a\,(\mu m)$	$b\,(\mu m)$	ξ_E	ϑ	$F = A_0 U/2b\vartheta\,(N/m)$
V. alginolyticus	0.35(0.01)	1.5(0.05)	4.3	0.97	1.7×10^{-7}
C. crescentus	0.42(0.01)	0.96(0.03)	2.3	0.89	2.1×10^{-7}
E. coli minicell	0.41(0.01)	0.41(0.01)	1	0	N.A.

Cell body sizes for the various strains used, along with the value of the Stokeslet per unit length to be used, to rigorously model the ellipsoid.

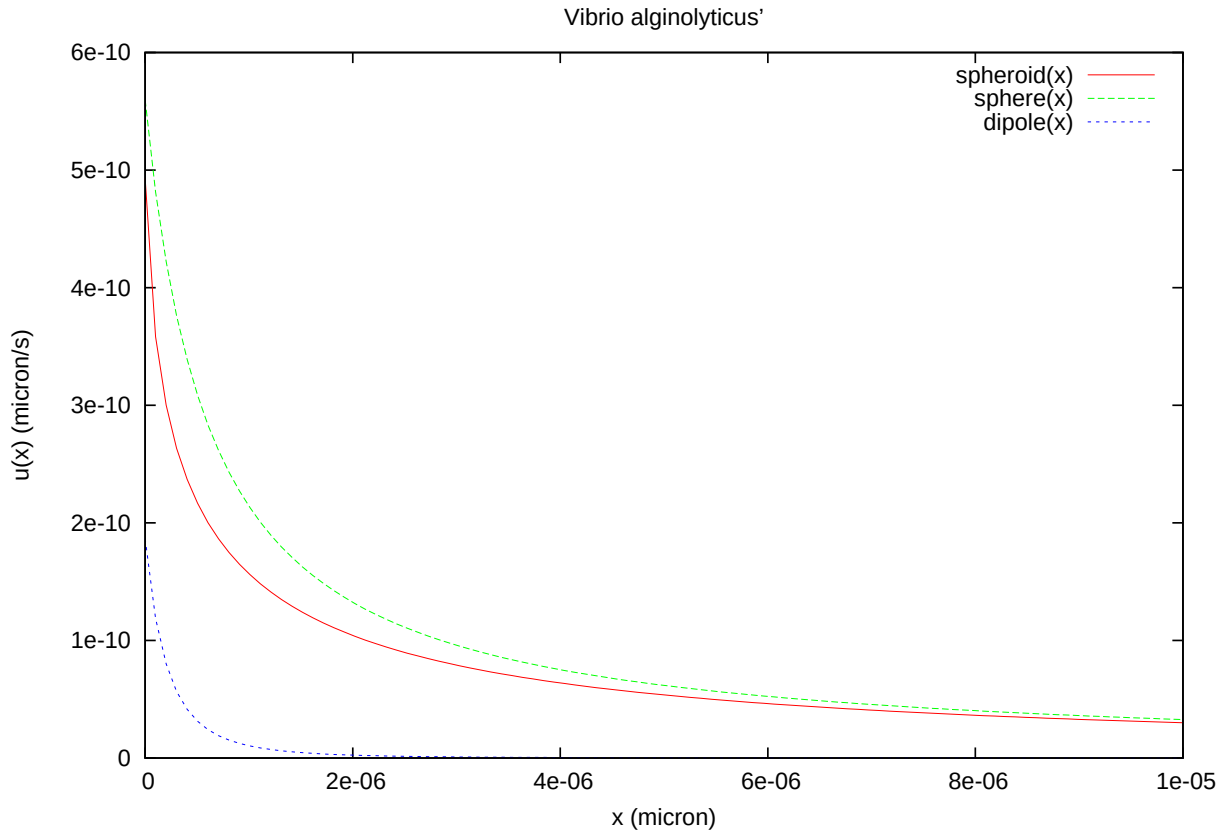

Figure C-2: Flow fields at the flagellum due to the cell body.

Variation in the flow field induced by the ellipsoidal head, as compared to the same by a sphere with equal linear drag. Also shown is the contribution due to a doublet placed at the sphere center to match boundary conditions at the sphere surface.

Stokeslet already included [35]. The strength of the doublet, to be placed at the center of the sphere for a sphere of radius a_E, to match no slip boundary conditions at the sphere surface is [35],

$$\vec{u}(r) = \frac{Fa_E^2}{24\pi\eta}\left(\frac{1}{r^3} - \frac{3x^2}{r^5}, \frac{-3xy}{r^5}, \frac{-3xz}{r^5}\right).$$

For observation along the x axis this becomes,

$$\vec{u}(x) = \frac{Fa_E^2}{12\pi\eta}\left(-\frac{1}{x^3}, 0, 0\right)$$

Thus, the addition of a dipole will change the velocity field at the observation point x_0 insignificantly ($< 0.1\%$) when compared to $u_1(r_0)$ or $u_2(r_0)$. The dipole contribution to the velocity field is also shown in Fig. C-2.

APPENDIX D

ELECTRICAL ANALOG FOR FLAGELLAR PROPULSION.

The flagellar motor is the source of power which drives the bacteria forward. The power output is converted into actual forward motion of the cell body. This is very similar to electrical circuits where voltage sources drive currents through different loads. In this section, I will discuss an electrical analog of bacterial propulsion, to better understand the various sources of energy dissipation. Equation 3.6, describes the torque balance equation for the cell body and the flagellum. It can be combined with Eqn. 3.5, by replacing U by $B\omega/(A+A_0)$ to obtain

$$D_0\Omega = D\omega - \frac{B^2\omega}{(A+A_0)} \qquad (D.1)$$

This expression clearly displays all the sources of dissipation in the system. The total power output by the motor is dissipated in parts by the rotational drag of the head ($D_0\Omega^2$), the rotational drag of the flagellum ($D\omega^2$), and the drag of the cell as a whole ($B^2\omega^2/(A+A_0) = (A+A_0)U^2$). One can clearly see the analogy of the rotation rates to electrical currents and drags to electrical resistances. Thus, Eqn. D.1 can be described by an equivalent circuit as shown in Fig D-1.

We will deal with magnitudes in the electrical analog, and disregard the signs of the rotation speeds. The motor is the source which drives the current through the loads. The total current Ω_M is divided in the parallel resistances. The upper arm is for the flagellum. As the flagella is a spiral, it has two components corresponding to the angular and linear parts. The angular part is just its rotational drag, while the linear part is the dissipation due to the translation of the whole cell. The lower arm stands for the cell body with only one load depicting the rotational drag. It is interesting to note, that as the two arms are parallel, the torque balance relation states that the potential across

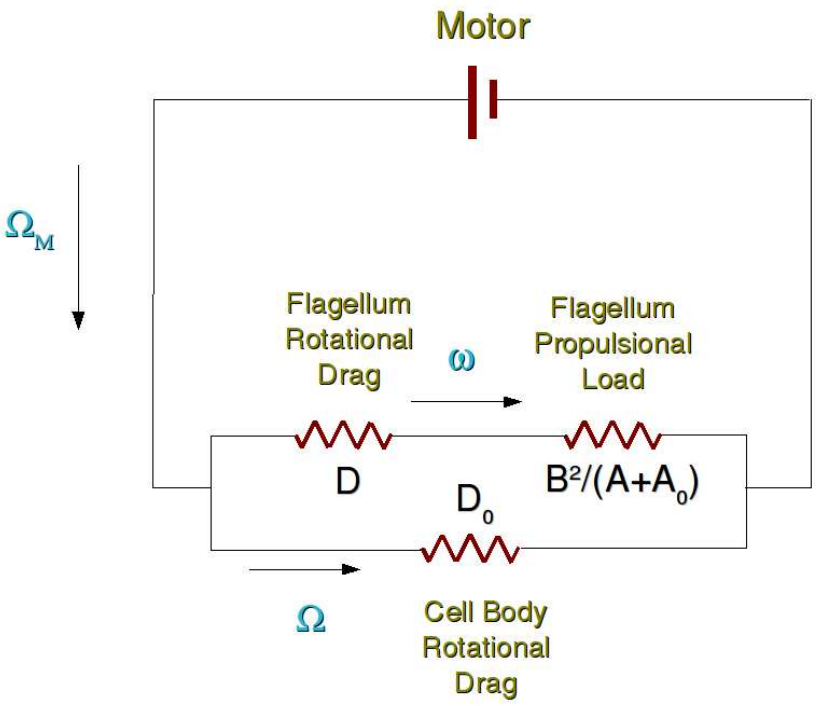

Figure D-1: Electrical analog of flagellar propulsion.

The motor is analogous to a voltage source, driving a current (Ω_M) through loads. The flagellum and the cell body act as a parallel connection of resistances. The two contributions for the flagellar arm are rotational and propulsion loads, while the cell body only experiences rotational drag.

the arms is the same ($D_0\Omega = D\omega + BU$). Also worth pointing out is, that experimentally it was found, that the load due to the propulsion (forward motion of the cell body and flagellum) is much smaller than due to rotational drag. Table B-1 shows the distribution of power dissipation of the strains for which the propulsion matrix elements were measured directly (Table 3.1).

The contribution to the dissipation is largest for the flagellum rotational drag, followed by the rotation of the cell body. The lowest energy is used in translating the cell forward, which is the reason for the low propulsion efficiency, i.e. a small fraction of the energy output is actually converted to the forward motion of the cell. The dissipation are plotted out as pie charts in Fig. D-2.

Bacterial Strain		**Dynamic Variables**				**Matrix Elements**					**Power Dissipation**		
Genus	**Name**	n_D	V	$\frac{\omega}{2\pi}$	$\frac{\Omega}{2\pi}$	A	A_0	B	D	D_0	$D\omega^2$	$D_0\Omega^2$	$(A+A_0)V^2$
			$(\frac{\mu m}{s})$	(Hz)	(Hz)	$(\times 10^{-8}, N\cdot s/m)$		$(\times 10^{-16}, N\cdot s)$	$(\times 10^{-22}, N\cdot s\cdot m)$		$\times 10^{-17} W$		
E. coli	HCB30	200	22(0.4)	120(2)	15(1)	1.5(0.05)	1.4(0.01)	7.9(0.2)	7.0(0.2)	42(0.1)	39.7	3.7	1.4
V. alginolyticus	YM42	140	34(1)	571(12)	26(1)	0.73(0.06)	1.3(0.01)	2.3(0.2)	2.0(0.1)	47(0.1)	257	12.5	2.4

Table B-2: Dissipation sources for *E. coli* and *V. alginolyticus*.

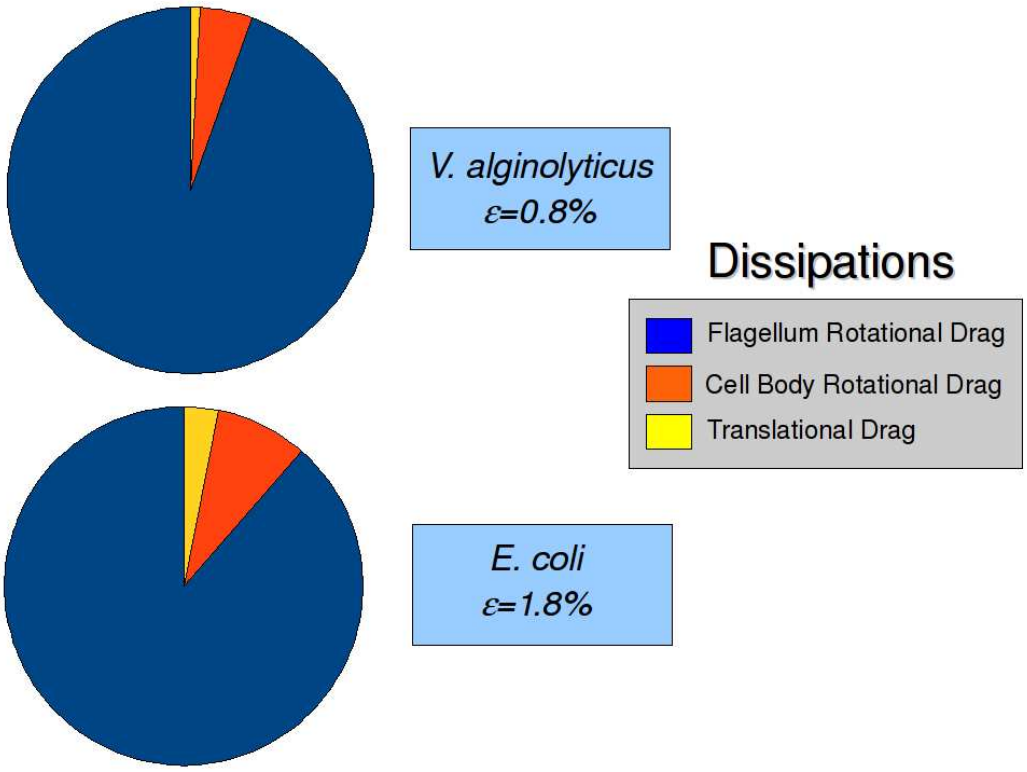

Figure D-2: Power dissipation in motility of *E. coli* and *V. alginolyticus.*

Largest chunk of energy output is dissipated in rotating the cell body. A small fraction can be utilized for translation, which leads to a tiny propulsion efficiency.

Bibliography

[1] H. I. Adler, W. D. Fisher, A. Cohen, and A. A. Hardighee. Minature *Escherchia coli* cells deficient in dna. *Proc. Natl. Acad. Sci.*, 57:321–326, 1967.

[2] J. Adler. Chemotaxis in bacteria. *Annu. Rev. Biochem.*, 44:341–356, 1975.

[3] R. H. Luchsinger and. Bergersen and J. G. Mitchel. Bacterial swimming strategies and turbulence. *Biophys. J.*, 77:2377–2386, 1999.

[4] A. Ashkin. Forces of a single-beam gradient laser trap on a dielectric sphere in the ray optics regime. *Biophys. J.*, 61:569–582, 1992.

[5] A. Ashkin, J. M. Dziedzic, J. E. Bjorkholm, and S. Chu. Observation of a single-beam gradient force optical trap for dielectric particles. *Optics Lett.*, 11:288–290, 1986.

[6] T. Atsumi, L. McCartert, and Y. Imae. Polar and lateral flagellar motors of marine vibrio are driven by different ion-motive forces.

[7] G. M. Barbara and J. M. Mitchell. Bacterial tracking of motile algae.

[8] H. C. Berg. Chemotaxis in bacteria. *Annu. Rev. Biophys. Bioeng.*, 4:119–136, 1975.

[9] H. C. Berg. *Random Walks in Biology*. Princeton University Press, 1 edition, 1993.

[10] H. C. Berg. The rotary motor of bacterial flagella. *Annu. Rev. Biochem.*, 72:19–54, 2003.

[11] H. C. Berg, M. D. Manson, and M. P. Conley. Dynamics and Energetics of Flagellar Rotation in Bacteria. *Symp. Soc. Exp. Biol.*, 35:1–31, 1982.

[12] H. C. Berg and E. M. Purcell. The physics of chemoreception. *Biophys. J.*, 20:193–219, 1977.

[13] W. Bialek and S. Setayeshgar. Physical limits to biochemical signaling. *Proc. Natl. Acad. Sci.*, 102:10040–10045, 2005.

[14] K. M. Blair, L. Turner, J. T. Winkelman, H. C. Berg, and D. B. Kearns. A molecular clutch disables flagella in the bacillus subtilis biofilm. *Science*, 320:1636–1638, 2008.

[15] S. Chattopadhyay, R. Moldovan, C. Yeung, and X. L. Wu. Swimming efficiency of bacterium *Escherichia coli*. *Proc. Natl. Acad. Sci.*, 103(37):13712–13717, 2006.

[16] S. Chattopadhyay and X. L. Wu. *In preparation*.

[17] X. Chen and H. C. Berg. Torque-speed relationship of the flagellar rotary motor of *Escherichia Coli*. *Biophys. J.*, 78:1036–1041, 2 2000.

[18] S. Childress. *Mechanics of swimming and flying*. Cambridge Studies in Mathematical Biology. Cambridge University Press., 1 edition, 1981.

[19] Allen T. Chwang and T. Yao-Tsu Wu. Hydromechanics of low-reynolds-number flow. part 2. singularity method for stokes flows. *J of Fluid Mech.*, 67(4):787–815, 1975.

[20] N. C. Darnton, L. Turner, S. Rojevsky, and H. C. Berg. On torque and tumbling in swimming *Escherichia coli*. *J. Bacteriol.*, 189(5):1756–1764, 2007.

[21] W. de Boer, C. Golten, and W. Scheffers. Effects of some chemical factors on flagellation and swarming of *Vibrio alginolyticus*. *Antonie van Leeuwenhoek*, (1), 1975.

[22] J. Gray and G. J. Hancock. The self-propulsion of microscopic organisms through liquids. *J. of Exp. Bio.*, 32:802–814, 1955.

[23] H. P. Grossart, G. F. Steward, J. Martinez, and F. Azam. A simple, rapid method for demonstrating bacterial flagella. *Appl. Environ. Microbiol.*, 66(8):3632–3636, 2000.

[24] J. Happel and H. Brenner. *Low Reynolds Number Hydrodynamics*. Springer, 1 edition, 1981.

[25] M. Homma, H. Oota, S. Kojima, I. Kawagishi, and Y. Imae. Chemotactic responses to an attractant and a repellent by the polar and lateral flagellar systems of *Vibrio alginolyticus*. *Microbiol.*, 142:2777–2783, 1996.

[26] H. Hotani. Mico-video study of moving bacterial flagellar filaments. *J. Mol. Biol.*, 156:791–806, 4 1982.

[27] T. Minamino Y. Imae, F. Oosawa, Y. Kobayashi, and K. Oosawa. Effect of intracellular ph on rotational speed of bacterial flagellar motors. *J. Bacteriol.*, 85:1190–1194, 2003.

[28] R. E. Johnson. *Slender-body theory for Stokes flow and flagellar hydrodynamics*. PhD thesis, California Institute of Technology, 1977.

[29] R. E. Johnson and C. J. Brokaw. Flagellar hydrodynamics. a comparison between resistive-force theory and slender-body theory. *Biophys. J.*, 25(1):113–127, January 1979.

[30] M. J. Kim, J. C. Bird, J. Park, T. R. Powers, and K. S. Breuer. Particle Imaging Velocimetry Experiments on a Macro-scale Model for Bacterial Flagellar Bundling. *Experiments in Fluids*, 37:782–788, 12 2004.

[31] E. Korobkova, T. Emonet, J. M. G. Villar, T. S. Shimizu, and P. Cluzel. From molecular noise to behavioural variability in single bacterium. *Nature*, 428:574–578, 2004.

[32] S. Kudo, N. Imai, M. Nishitoba, S. Sugiyama, and Y. Magariyama. Asymmetric swimming pattern of vibrio alginolyticus cells with single polar flagella. *FEMS Microbiol. Lett.*, 242:221–225, 2005.

[33] G. Li and J. X. Tang. Low flagellar motor torque and high swimming efficiency of *Caulobacter crescentus* swarmer cells. *Biophys. J.*, 91:2726–2734, 2006.

[34] J. Lighthill. Flagellar hydrodynamics. *SIAM Rev.*, 18(2):161–230, 4 1976.

[35] J. Lighthill. *Mathematical Biofluiddynamics*. SIAM, 3 edition, 1989.

[36] G. Lowe, M. Meister, and H. C. Berg. Rapid rotation of flagellar bundles in swimming bacteria. *Nature*, 325:637–640, 2 1987.

[37] R. M. Macnab and M. K. Ornston. Normal-to-curly flagellar transitions and their role in bacterial tumbling. stabilization of an alternative quaternary structure by mechanical force. *J. Mol. Biol.*, 112:1–30, 5 1977.

[38] Y. Magariyama, S. Sugiyama, M. Kazamasa, I. Kawagishi, Y. Imae, and S. Kudo. Simultaneous measurement of bacterial flagellar rotation rate and swimming speed. *Biophys. J.*, 69:2154–2162, 11 1995.

[39] Y. Magariyama, S. Sugiyama, K. Muramoto, Y. Maekawa, I. Kawagishi, Y. Imae, and S. Kudo. Very fast flagellar rotation. *Nature*, 371:752–752, 2002.

[40] R. M. Mcnab. Genetics and biogenesis of bacterial flagella. *Annu. Rev. Genet.*, 26:131–158, 1992.

[41] R. M. Mcnab and S. I. Aizawa. Bacterial motility and the bacterial flagellar motor. *Ann. Rev. Biophys. Bioeng.*, 13:51–83, 1984.

[42] M. Meister, G. Lowe, and H. C. Berg. Proton flux through the bacterial flagellar motor. *Cell*, 49:643–650, 6 1987.

[43] K. Muramoto, I. Kawagishi, S. Kudo, Y. Magariyama, Y. Imae, and M. Homma. High-speed rotation and speed stability of the sodium-driven flagellar motor in vibrio alginolyticus.

[44] K. C. Neuman and S. M. Block. Optical trapping. *Rev. Sci. Instrum.*, 75:2787–2809, 9 2004.

[45] E. M. Purcell. The efficiency of propulsion by a rotating flagellum. *Proc. Natl. Acad. Sci.*, 9:11307–11311, 10 1997.

[46] M. Ramia, D. L. Tullock, and N. Phan-Thien. The role of hydrodynamic interaction in the locomotion of microorganisms. *Biophys. J.*, 65:755–778, 1993.

[47] A. D. Rowe, M. C. Leake, H. Morgan, and R. M. Berry. Rapid rotation of micron and submicron dielectric particles measured using optical tweezers. *J. Mod. Opt.*, 50(10):1539–1554, 2003.

[48] A. D. T. Samuel and H. C. Berg. Torque-generating units of the bacterial flagellar motor step independently. *Biophys. J.*, 71:918–923, 8 1996.

[49] Y. Sowa, H. Hotta, M. Homma, and A. Ishijima. Torque-speed relationship of the Na^+-driven flagellar motor of *Vibrio alginolyticus*. *J. Mol. Biol.*, 327:1043–1051, 2003.

[50] R. Stocker, J. R. Seymour, A. Samadani, D. E. Hunt, and M. F. Polz. Rapid chemotactic response enables marine bacteria to exploit ephemeral microscale nutrient patches. *Proc. Natl. Acad. Sci.*, 105:4209–4214, 2008.

[51] Y. Takano, K. Yoshida, S. Kudo, M. Nishitoba, and Y. Magariyama. Analysis of small deformation of helical flagellum of swimming *Vibrio alginolyticus*. *JSME Int. J., Ser. C*, 46:1241–1247, 2003.

[52] Y. Takano, K. Yoshida, S. Kudo, M. Nishitoba, and Y. Magariyama. Analysis of small deformation of helical flagellum of swimming vibrio alginolyticus. *JSME International Journal Series C*, 46(4):1241–1247, 2003.

[53] G. I. Taylor. Ther action of waving cylindrical tails in propelling microscopic organisms. *Proc. Roy. Soc. Lond. A*, 211:225–239, 6 1952.

[54] L. Turner, W. M. Ryu, and H. C. Berg. Real-time imaging of fluorescent flagellar filaments. *J. of Bacteriol.*, 182(10):2793–2801, 5 2000.

[55] G.M. Viswanathan, S. V. Buldyrev, S. Havlin, M.G.E. da Luz, E.P. Raposo, and H.E. Stanley. Optimizing the success of random searches. *Nature*, 401(6756):911–914, 2003.

[56] G. J. Wuite, R. J. Davenport, A. Rappaport, and C. Bustamante. An integrated laser trap/flow control video microscope for the study of single biomolecules. *Biophys. J.*, 79:1155–1167, 8 2000.

[57] J. Xing, F. Bai, R. Berry, and G. Oster. TorqueâĂŞspeed relationship of the bacterial flagellar motor.